THESIS FOR THE DEGREE OF DOCTOR OF PHILOSOPHY IN MATERIALS SCIENCE

Hydrogen Embrittlement of Austenitic Stainless Steels

Influence of hydrogen charging, microstructure and low-temperature carburizing

XIAO QIN

Department of Industrial and Materials Science

CHALMERS UNIVERSITY OF TECHNOLOGY

Gothenburg, Sweden 2026

Hydrogen Embrittlement of Austenitic Stainless Steels

Influence of hydrogen charging, microstructure and low-temperature carburizing

XIAO QIN

ISBN 978-91-8103-364-9

Doktorsavhandlingar vid Chalmers tekniska högskola

Ny serie nr 5821

ISSN 0346-718X

https://doi.org/10.63959/chalmers.dt/5821

Department of Industrial and Materials Science

Chalmers University of Technology

SE-412 96 Gothenburg

Sweden

Telephone + 46 (0)31-772 1000

Cover: In-situ SEM-EBSD reveals the effect of hydrogen on deformation microstructure

Printed by Chalmers digitaltryck

Gothenburg, Sweden 2026

To myself

You chose the long road on purpose.

Not because it was easy, but because the questions mattered and you believed careful thinking could move the world, even if only by a fraction.

Hydrogen Embrittlement of Austenitic Stainless Steels

Influence of hydrogen charging, microstructure and low-temperature carburizing

XIAO QIN
Department of Industrial and Materials Science
Chalmers University of Technology

Abstract

Austenitic stainless steels (ASS) are widely applied in hydrogen-related infrastructures because of their excellent corrosion resistance, low hydrogen diffusivity and good ductility. However, ASS still faces the risk of failure when exposed to hydrogen environments for extended periods. More specifically, hydrogen reduces ductility and fracture toughness, leading to sudden fracture of steel, a condition known as hydrogen embrittlement (HE), thus posing a critical challenge to the hydrogen economy. Microstructure and surface treatment are key factors affecting HE because they influence hydrogen diffusion and uptake, thus affecting deformation and mechanical properties. This thesis study systematically investigates the effects hydrogen charging, microstructure and low-temperature carburizing (LTC) on the HE of ASS. HE behavior was evaluated by introducing hydrogen into steel using cathodic charging combined with slow strain rate tensile tests. Scanning electron microscopy (SEM), X-ray diffraction (XRD), transmission electron microscopy (TEM), and electron backscatter diffraction (EBSD) techniques were used for analyzing the microstructure and fracture morphology, along with hydrogen content, to reveal the failure mechanism. The main results of this study indicate that:

1) Hydrogen uptake, microstructure, and surface morphology are influenced by current density and electrolyte. During the hydrogen charging process in H_2SO_4 electrolyte, high current density can lead to surface cracking, martensitic phase transformation, and increased hydrogen content due to high hydrogen fugacity and surface stress. Increasing surface roughness can reduce hydrogen uptake and suppress surface cracking. Hydrogen charging in NaCl and NaOH electrolytes reveal intact surfaces and low hydrogen content.

2) LTC treatment introduces an approximately 22 μm thick expanded austenite layer on the surface of ASS, exhibiting lattice expansion, high hardness and high carbon concentration. The expanded austenite effectively suppresses hydrogen and strain-induced martensitic phase transformation. The effect of LTC on hydrogen-induced cracking and HE depends on the surface carbon concentration. Low carbon concentration in expanded austenite reduced surface cracking, HE and hydrogen uptake, while high carbon concentration leads to severe surface cracking, decomposition of expanded austenite, and increased hydrogen uptake and HE.

3) Hydrogen, similar to interstitial carbon, strengthens ASS thin film but introduces brittleness. Hydrogen embrittlement and carbon embrittlement share similarities, both being caused by stress cracking induced by high concentration gradients. The coexistence of both leads to softening, attributed to a decrease in lattice parameters and precipitation. Hydrogen triggered precipitation, deformation twins, accelerated local deformation with enhanced orientation-related slip.

Keywords: Austenitic stainless steel, low-temperature carburizing, expanded austenite, microstructure, cathodic hydrogen charging, hydrogen embrittlement

Preface

This doctoral thesis is based on the research work performed at the Department of Industrial and Materials Science at Chalmers University of Technology between December 2021 and January 2026. The work has been carried out under the supervision of Professor Yu Cao (supervisor), Professor Huiqun Liu (co-supervisor) and Professor Lars Nyborg (examiner). This work was financially supported by the Swedish Innovation Agency (2021-01908), the Swedish Energy Agency (2021-036176), TechForH2, the Production Area of Advance and Chalmers University of Technology.

List of Appended Papers

Paper I: Insights into cathodic hydrogen charging- surface morphology evolution

X. Qin, Y. Shi, S. B. A. Malladi, L. Nyborg, H. Liu, Y. Cao

Submitted for publication in International Journal of Hydrogen Energy

Paper II: Microstructure evolution induced by cathodic charging in low-temperature carburized 304 austenitic stainless steel

X. Qin, L. Nyborg, H. Liu, A. Bauer, Y. Cao

International Journal of Hydrogen Energy, 173 (2025), 151357.

Paper III: Deformation behavior and hydrogen embrittlement of low-temperature carburized 304 and 316L austenitic stainless steels

X. Qin, Y. Shi, L. Nyborg, H. Liu, Y. Cao

Submitted for journal publication

Paper IV: Low-temperature carburizing improves hydrogen embrittlement resistance of cold worked 304 austenitic stainless steel.

X. Qin, L. Nyborg, H. Liu, A. Bauer, Y. Cao

Journal of Materials Research and Technology, 36 (2025), 8816-8825.

Paper V: Hydrogen, similar to interstitial carbon, significantly strengthen 316 austenitic stainless steel

X. Qin, Y. Shi, L. Nyborg, H. Liu, Y. Cao

Manuscript

Paper VI: In-situ SEM-EBSD investigation of hydrogen effects on deformation and hydrogen embrittlement of NCF 3015 alloy

X. Qin, Y Shi, S. B. A. Malladi, L. Nyborg, H. Liu, Y. Cao

Manuscript

Contribution to the appended papers

Paper I: The authors conducted hydrogen charging experiments and characterized the microstructure, designed the manuscript framework, and wrote and revised the paper.

Paper II: The authors designed the experimental scheme, characterized the microstructure, and wrote and revised the paper.

Paper III: The authors conducted hydrogen-charging and tensile test and characterized the microstructure and wrote and revised the paper.

Paper IV: The authors designed the hydrogen-chargingg experiment and conducted mechanical property tests, characterized the microstructure, and wrote and revised the paper.

Paper V: The authors designed hydrogen charging parameters, prepared tensile samples and completed tensile tests, characterized the microstructure, and wrote and revised the paper.

Paper VI: The authors prepared in-situ tensile samples and performed in-situ ESBD-SEM experiments, characterized the microstructure, and wrote and revised the paper.

Papers published but not included in this thesis

Paper I: Recrystallization and texture evolution of warm-pilgered FeCrAl alloy tube during annealing at 850 °C.

X. Qin, Z. Liu, H. Liu, R. Zhang, Q. Pan, Y. Wang, J. Pei

Journal of Nuclear Materials, 562 (2022), 153575.

Paper II: Recrystallization and texture evolution of cold pilgered FeCrAl cladding tube during annealing at 700 °C~ 1000 °C.

X. Qin, R. Zhang, P. Du, J. Pei, Q. Pan, Y. Cao, H. Liu

Journal of Nuclear Materials, 577 (2023), 154303.

Paper III: Microstructure and texture evolutions in FeCrAl cladding tube during pilger processing.

X. Qin, R. Zhang, P. Du, J. Pei, Q. Pan, Y. Cao, H. Liu

Journal of Materials Research and Technology, 25 (2023), 5506-5519.

Paper IV: Microstructural stability and mechanical properties of advanced FeCrAl alloy cladding after thermal exposure at 800° C~ 1200° C

X. Qin, R. Zhang, P. Du, J. Pei, Q. Pan, H. Liu, Y. Cao

Journal of Nuclear Materials, 607 (2025), 155653.

Paper V: Insights from Microstructure and Recrystallization Comparisons of Wrought FeCrAl and Oxide Dispersion‑Strengthened Nanostructured Ferritic Alloy Tubes

X. Qin, G. Lin, R. Zhang, P. Du, Y. Cao, H. Liu

Advanced Engineering Materials 27 (2025), 2402484.

List of abbreviations and acronyms

ASS	Austenitic stainless steel
BCC	Body-centered cubic
BSE	Backscattered electrons
CW	Cold working
EBSD	Electron backscattered diffraction
EPMA	Electron probe micro-analyzer
FCC	Face-centered cubic
GB	Grain boundary
HE	Hydrogen embrittlement
HEDE	Hydrogen-enhanced decohesion
HELP	Hydrogen-enhanced localized plasticity
HIC	Hydrogen-induced cracking
IPF	Inverse pole figure
KAM	Kernel average misorientation
LTC	Low-temperature carburizing
OM	Optical microscope
SA	Solution annealing
SEM	Scanning electron microscopy
SFE	Stacking fault energy
SSRT	Slow strain rate tensile
TRIP	Transformation induced plasticity
TWIP	Twinning induced plasticity
TDS	Thermal desorption spectroscopy
TEM	Transmission electron microscopy
XRD	X-ray diffraction
XPS	X-ray photoelectron spectroscopy

γ	Austenite phase
γ_{c}	Carbon expanded austenite
γ_{H}	Hydrogen expanded austenite
α'	Alpha martensite phase
α	Ferrite phase
ε	Epsilon martensite phase
$R_{p0.2}$	0.2% offset yield strength
R_m	Maximum tensile stress
T	Temperature
t	Time
D	Difusivity
δ	Total elongation
φ	Reduction of area
i	Current density
f_{H_2}	Hydogen fugacity
η	Overpotential
L	Sample thickness
ε	Engineering strain
σ	Engineering stress
a	Lattice parameters

Table of Contents

1 Introduction

1.1 Background and motivation

Hydrogen is widely regarded as a key energy carrier for achieving carbon neutrality and sustainable development [1]. However, the safe and reliable utilization of hydrogen is critically hindered by hydrogen embrittlement (HE) [2-4], a phenomenon that drastically reduces the ductility, fracture toughness, and fatigue life of metallic materials.

Steels, especially austenitic stainless steels (ASS), are extensively used in hydrogen-related infrastructures [5] such as storage tanks, pressure vessels, valves, and fuel cell components owing to their excellent corrosion resistance, high toughness, and low hydrogen diffusivity. ASS possesses a face-centered cubic (FCC) crystal structure that generally offers good resistance to HE compared with ferritic and martensitic steels [6,7]. However, their relatively low strength and unsatisfied wear resistance restrict their application under demanding service conditions. Although work hardening (cold deformation) can enhance strength, the accompanying strain-induced martensitic transformation in metastable grades greatly increases the susceptibility to HE [8,9]. Nevertheless, even stable austenitic grades can suffer from strength degradation, cracking and ductility loss when exposed to hydrogen-rich environments or under cathodic charging conditions [10,11]. Improving the strength and mitigating HE of ASS is therefore essential for advancing the hydrogen economy.

Recent studies [12,13] address the low-temperature carburizing (LTC), which has been developed to enhance surface hardness and wear resistance while retaining the corrosion resistance of ASS. The LTC treatment produces an expanded austenite (S-phase) layer with carbon supersaturation at temperatures below carbide formation thresholds. Expanded austenite exhibits high residual compressive stress and hardness, thereby improving mechanical strength and fatigue performance [14]. Studies have shown that LTC can also improve resistance to HE. This effect has been attributed to the compressive stresses generated in the expanded austenite layer and the suppression of martensitic transformation [15,16], both of which hinder hydrogen penetration. However, other studies [17] found that excessive carbon content or high internal stress of expanded austenite can instead promote carbon-induced cracking. The mechanisms underlying these contradictory observations remain unclear, particularly regarding how carbon and hydrogen interact to influence the deformation and fracture behavior of ASS.

It is generally accepted that microstructural characteristics are crucial factors influencing HE. Vacancies, dislocations, grain boundaries, and precipitates can act as both hydrogen traps and lead to rapid hydrogen diffusion channels, influencing hydrogen distribution and concentration [18]. These microstructural characteristics interact with hydrogen, evolving particularly during mechanical loading. The factors such as dislocation motion, slip banding, twinning, and phase transformation, have received limited attention. Here, combining hydrogen-charged tensile bar with advanced characterization techniques, such as in-situ SEM–EBSD analysis during tensile testing, offers a powerful means to visualize deformation mechanisms and crack initiation in real time.

Cathodic hydrogen charging is a widely used method for introducing hydrogen into steel to study HE, owing to its low cost, simple operation and safety. This method is typically carried out in an aqueous solution and essentially introduces hydrogen into the sample via the hydrogen evolution reaction. Parameters such as electrolyte and current density affect hydrogen uptake by altering the hydrogen fugacity [19,20]. General studies have found that HE in acidic electrolytes is more severe than in alkaline and neutral electrolytes [21], mainly due to i) higher content of absorbed hydrogen, ii) higher hydrogen fugacity and iii) possible material changes induced, such as microstructure modification and surface damage [21-23]. Although the method is widely used in HE investigations, few studies have focused on the effects of hydrogen charging process on microstructure and hydrogen uptake. Therefore, a systematic understanding of how charging parameters influence microstructural evolution and hydrogen uptake is essential for the rational optimization of charging conditions. Such understanding enables the minimization of charging-induced artifacts and side effects, thereby reducing their interference with experimental observations and ensuring the reliability and reproducibility of HE test results. Another key factor is the extremely low hydrogen diffusivity in ASS, which means that the hydrogen concentration and its through-thickness gradient to be strongly dependent on the sample thickness and the hydrogen charging time. Although these parameters are crucial for accurately assessing hydrogen distribution and gaining a deeper understanding of HE mechanism, they are rarely considered systematically and comprehensively. Therefore, this study systematically investigates the effects of hydrogen charging parameters on microstructure and hydrogen uptake, aiming to optimize these parameters and reduce the interference of side effects on HE research.

The focus of this thesis is on the roles of LTC, hydrogen charging conditions and microstructural characteristics in determining HE behavior. By correlating hydrogen uptake, mechanical response and microstructure evolution, this study aims to establish a comprehensive understanding of the mechanisms underlying hydrogen-induced strengthening, softening, and fracture in ASS.

The motivation of this study, scientifically speaking, is to elucidate the effects of cathodic hydrogen charging on microstructure and hydrogen uptake, to understand the advantages and limitations of this method. Second, it aims to investigate the fundamental mechanisms of the interaction between hydrogen and carbon on the microstructure and their impact on the deformation behavior and mechanical properties of ASS. This includes understanding on how expanded austenite influences hydrogen diffusion, absorption and crack initiation. In engineering terms, the study provides practical guidance for designing hydrogen-resistant stainless steels by optimizing surface treatments and microstructure. The results are expected to support the development of durable materials for hydrogen energy economy.

1.2 Research objectives and approach

This doctoral thesis aims at comprehensively understanding of HE in ASS. Considering that surface treatment and microstructure affect hydrogen uptake and diffusion, and consequently HE, this study investigated samples with varying surface roughness, samples subjected to low-temperature carburizing, and samples with different alloy compositions and initial microstructures. Hydrogen was introduced into steels using the cathodic charging method. The effects of charging parameters on microstructure and hydrogen uptake were studied, providing optimized hydrogen charging conditions. Simultaneously, the effects of hydrogen charging on the microstructure and hydrogen uptake of samples with different surface treatments and microstructures were studied. Once hydrogen enters the sample, it will interact with solutes, vacancies, dislocations, precipitates and grain boundaries. The effects of hydrogen on deformation behavior and deformation microstructure, especially with different surface treatments, initial microstructures and hydrogen contents, are not yet fully understood, and these factors are crucial for explaining changes in mechanical properties and HE. To clearly elucidate the work content of this study, the following research questions (RQs) are formulated.

RQ1 How does cathodic hydrogen charging affect the microstructure and hydrogen uptake?

RQ2 How does hydrogen uptake affect mechanical properties and deformation behavior?

RQ3 How does carbon affect mechanical properties and deformation behavior?

RQ4 What are the combined effects of carbon and hydrogen on mechanical properties and deformation behavior?

Table 1.1 Research focus and the specific research question (RQ) in each appended paper.

Paper	RQ1	RQ2	RQ3	RQ4
Paper I	🟩			
Paper II	🟩			
Paper III		🟩	🟩	🟩
Paper IV		🟩	🟩	🟩
Paper V		🟩	🟩	🟩
Paper VI		🟩		🟩

The primary objectives of each appended paper can be summarized as follows:

Paper I addressed the effects of cathodic hydrogen charging on the microstructure and hydrogen uptake of 316L.

Paper II addressed the effects of cathodic hydrogen charging on the microstructure of as-received and LTC-treated 304.

Paper III compared the deformation behavior and mechanical properties of LTC-treated 304 and LTC-treated 316L after hydrogen uptake.

Paper IV examined the effect of LTC on the hydrogen embrittlement susceptibility of cold-worked 304.

Paper V investigated the effects of carbon and hydrogen on the deformed microstructure and mechanical properties of thin foil 316.

Paper VI presented an in-situ SEM-EBSD investigation on how hydrogen affects the deformation behavior, deformed microstructure and mechanical properties of NCF 3015 alloy.

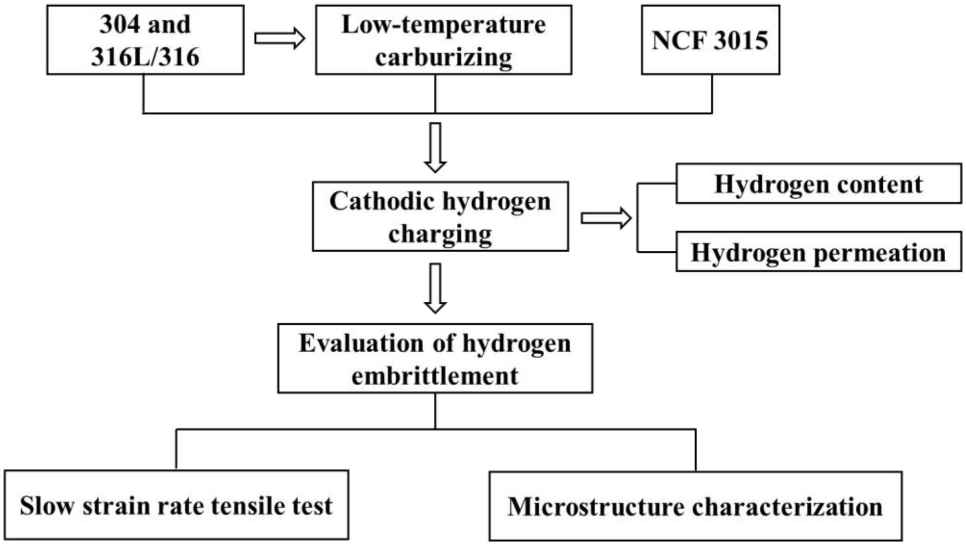

Figure 1.1 Overview of research approach used in this thesis study.

The overall research workflow is illustrated in Figure 1.1. In this study, a few austenitic stainless steels with different alloy compositions were selected for the investigations. AISI304 and 316L/316 are commercial austenitic stainless steels, while NCF 3015 is a precipitation-hardenable austenitic superalloy. Commercial 304 and 316L/316 alloys were subjected to low-temperature carburizing to obtain expanded austenite on the surface region. To investigate hydrogen embrittlement, hydrogen was introduced into steels using an electrochemical cathodic charging method. The effects of hydrogen on the microstructure, hydrogen diffusion and mechanical properties of the as-received and LTC samples were systematically compared. For the 3015 alloy, the focus was on the effects of hydrogen on deformation behavior, post-deformation microstructure, and mechanical properties. Hydrogen embrittlement failure was discussed by addressing hydrogen content, hydrogen diffusion, microstructure and mechanical properties.

2 Austenitic stainless steels

2.1 General introduction

Stainless steel is a chromium-containing, iron-based alloy known for its excellent resistance to corrosion and oxidation. Stainless steel was first discovered by British metallurgist Harry Brearley, who found that adding chromium to carbon steel improves the resistance to chemical attack. He named this new material "stainless steel (SS)" [24]. The development of SS addressed a critical challenge faced by many industries—the rusting and degradation of steel tools and components. Today, SS has become one of the most widely used engineering materials worldwide, finding applications in medical instruments, surgical tools, automotive parts, and aerospace components. Its combination of durability, corrosion resistance, and aesthetic appearance makes it highly desirable across a wide range of industrial and consumer applications.

The performance of SS is closely related to its microstructure and chemical composition. The binary Fe-Cr phase diagram (Figure 2.1) shows the effect of Cr content and temperature on phase composition. When the Cr content exceeds 12.7 wt%, single-phase ferrite (α) can be obtained. However, higher Cr content may accelerate the formation of Cr-rich α'/σ phase, causing embrittlement.

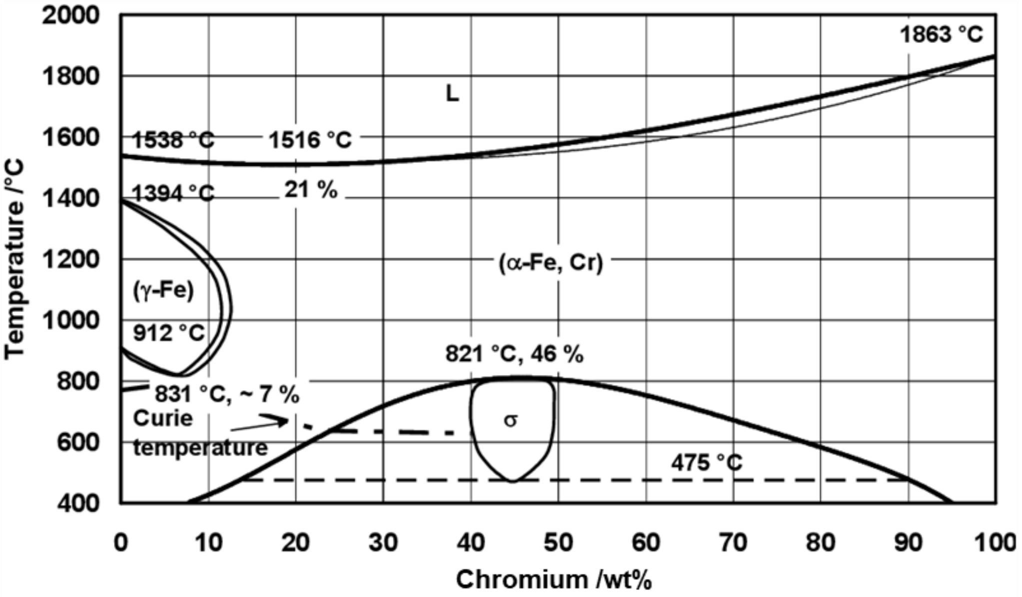

Figure 2.1 The binary Fe-Cr phase diagram [25].

The main components of SS are Fe, Cr, and Ni. As shown in the Fe-Ni-Cr isothermal cross section in Figure 2.2, austenite becomes dominant as the Ni content increases. Adding Ni to low-carbon 18 wt% Cr steel expands the austenitic phase region. When Ni content reaches approximately 8 wt%, full austenitic phase remains at room temperature, resulting in the well-known 18Cr-8Ni (wt%) austenitic stainless steel (ASS). More Ni is required regardless of whether the Cr content is higher or lower. For example, for more corrosion-resistant steels with higher Cr content, such as 25 wt% Cr steel, approximately 15 wt% Ni is needed to retain the austenite at room temperature.

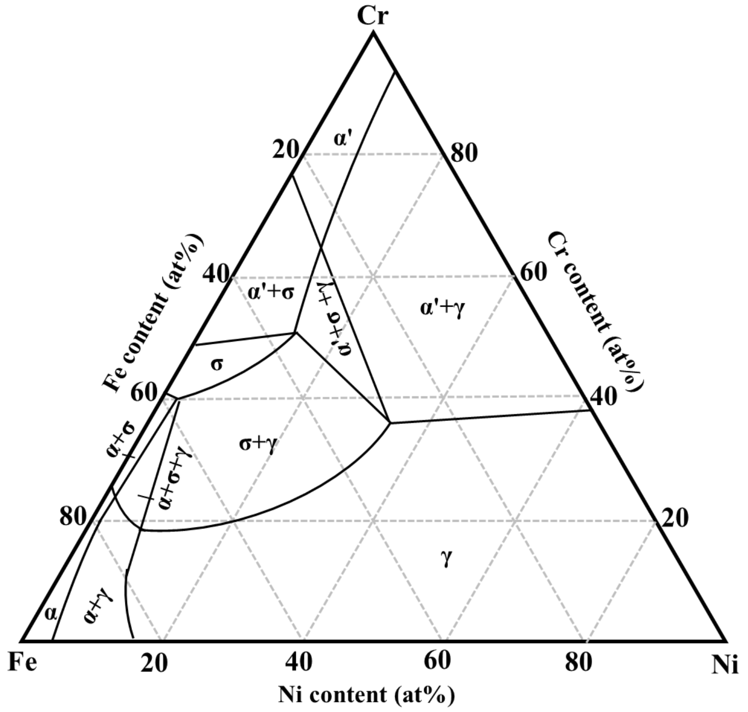

Figure 2.2 Fe-Ni-Cr isothermal section at 650 °C [26].

Typically, SS contains alloy elements such as Cr, Ni, Mo, Nb, Mn, Si, Ti, N, and C [27], each of which plays a crucial role in determining its microstructure and properties. The addition of Cr improves the corrosion resistance by promoting the formation of a stable, protective passive oxide film. The minimum Cr content of approximately 11 wt.% is required for passivation. Ni enhances ductility, toughness and resistance to corrosion as well as stability at high temperatures. Mo increases resistance to pitting and crevice corrosion in chloride-containing environments, while Mo and Nb together contribute to improved high-temperature strength. Si can improve resistance to high-temperature oxidation, while titanium is a strong carbide and nitride former. N and C are added to improve fatigue, wear and hardness of the steel. These alloying elements can be broadly categorized as ferrite stabilizers or austenite stabilizers, depending on their influence on phase stability. Among them, Cr, Mo, Si, and Nb are ferrite stabilizers, while Ni, C, N, and Mn are austenite stabilizers. Generally, increasing the ferrite content in stainless steel can improve its strength and magnetic properties, while increasing the austenite content can improve its ductility, formability and corrosion resistance.

2.2 Alloy grades used in this study

In this study, the materials used were a few selected austenitic stainless steels (ASS). ASS are characterized by a high nickel equivalent, which stabilizes the FCC crystal structure. They are the largest family of SS, accounting for approximately two-thirds of all SS production. ASS maintains an austenite phase at all temperatures from room temperature to melting point.

Consequently, they cannot be hardened by conventional heat treatment (except precipitation hardening), as they retain a single austenite phase at all temperatures. Referring to ASTM standards, 300 series (Cr-Ni) alloys are the largest group and the most widely used. In recent years, precipitation-hardened austenitic stainless steel has been developed to expand its application fields by introducing precipitates (such as carbides and Ni_3Ti) [28,29].

2.2.1 AISI 304

Type 304, also known as AISI/SAEs 304, UNS S30400 and EN 1.4301, is the most widely used stainless steel in the market. It contains both Cr (18~20%) and Ni (8~10.5%) and is also known as 18/8 steel. AISI 304 is a metastable ASS and is prone to deformation-induced martensite transformation. For the 304 ASS used in this study, the XRD and EBSD results in Figure 2.3 confirms that mechanical polishing during sample preparation may introduce a small amount of martensite (α'). AISI 304 is commonly used for applications such as kitchen, food processing, chemical containers, and medical equipment due to its excellent corrosion resistance, high ductility, and good mechanical properties.

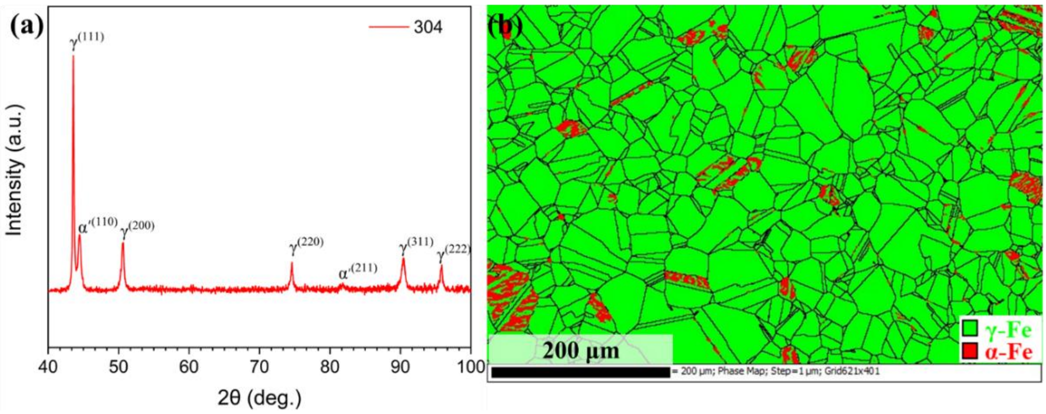

Figure 2.3 XRD pattern (a) and phase map (b) of solution annealed 304 austenitic stainless steel.

2.2.2 AISI 316L/316

Type 316, also known as AISI/SAE 316 UNS S31603 and EN 1.4404, is an evolution of type 304. It contains Cr (16~18%), Ni (10~14%), Mo (2~3%), and small quantities of carbon (≤0.03%). AISI 316L has better corrosion resistance than AISI 304, especially in chloride-rich environments. AISI 316L is typically used in applications requiring enhanced corrosion resistance such as marine equipment, chemical processing, pharmaceuticals, medical equipment, and certain types of food processing equipment. A typical 316L microstructure is shown in Figure 2.4. The IPF map (Figure 2.4a) shows equiaxed grains with various orientations, indicating that the microstructure is homogeneous. A large number of twin structures are observed within the grains. Due to its higher nickel equivalent than 304, it shows a stable austenite phase (Figure 2.4b). AISI 316 (UNS S31600, EN 1.4401) has a slightly higher carbon content (0.06 wt%) than 316L, but its microstructure and properties are very similar to those of 316L.

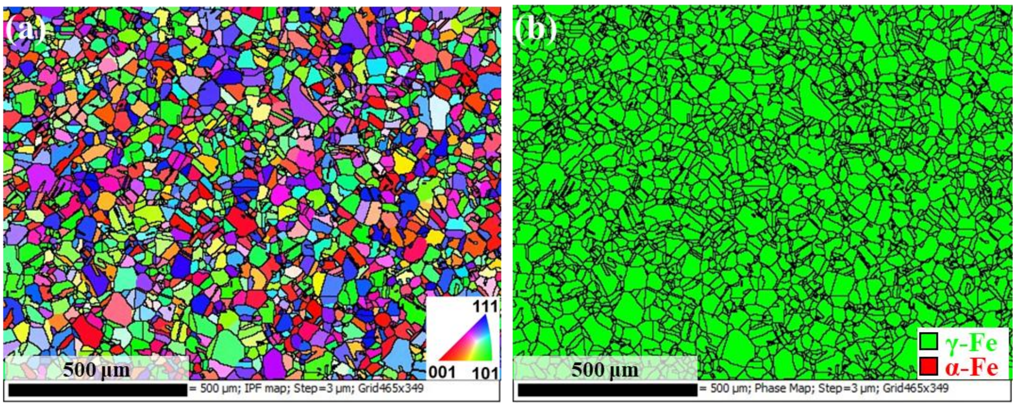

Figure 2.4 IPF map (a) and phase map (b) of solution annealed 316L austenitic stainless steel.

2.2.3 NCF 3015

NCF 3015 alloy (UNS S566315) is a precipitation-hardenable Fe-Cr-Ni-based alloy containing at least 30% Ni and 15% Cr. It is widely used in high-temperature applications such as exhaust valves and turbine blades. Through ageing, this alloy forms strengthening precipitates such as (Ti,Nb)C and $Ni_3(Ti,Al)$ to improve mechanical strength and fatigue resistance up to 700 °C [28]. The phase constituents and microstructure of the 3015 alloy used in this study is shown in Figure 2.5. In addition to the dominant FCC phase, there is also a small amount of carbides (Figure 2.5a). Figure 2.5b reveals that the austenite grains are approximately 10 μm in size, while Figure 2.5c shows that the carbides are mainly located at the triple junctions of the grains. Limited by the resolution, nano precipitates cannot be revealed in SEM images.

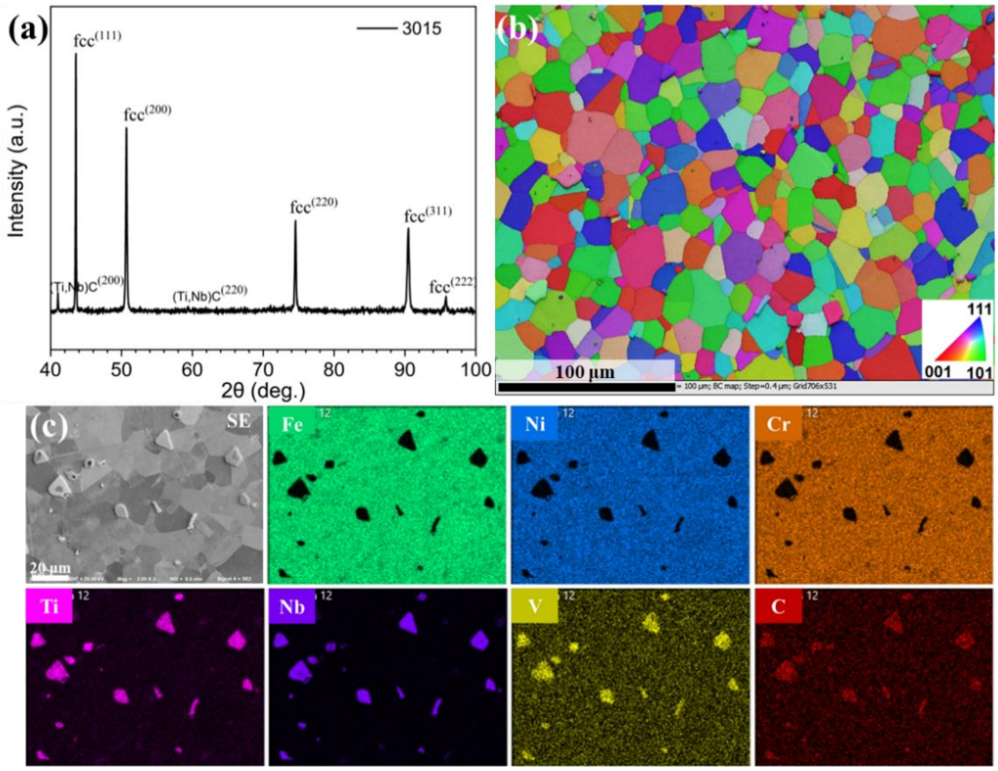

Figure 2.5 (a) XRD parttern, (b) IPF map and (c) EDS elemental map of 3015 alloy.

2.3 Low-temperature carburizing of austenitic stainless steel

2.3.1 Overview

Low surface hardness, unsatisfactory fatigue and tribological properties are the primary drawbacks of austenitic stainless steels, restricting their use in wear-critical applications. Furthermore, the deformation-induced martensitic transformation of metastable austenite can lead to a reduction in corrosion resistance. Consequently, enhancing the surface hardness and tribological properties while maintaining corrosion resistance is of significant economic and industrial importance, as it would expand the application range and extend the service life of components.

Carburizing has proven to be an effective surface treatment for enhancing surface hardness and fatigue properties. The carburizing process of austenitic stainless steels can be understood with reference to the time-temperature transformation diagram (see Figure 2.6) [30]. There are three paths for carburizing: A, B and C. In general, carburization results in the formation of chromium carbides ($Cr_{23}C_6$) or χ/ω-carbides, governed by the equilibrium solubility of carbon in austenite. These carbides, however, can deteriorate both corrosion resistance and ductility. At high temperatures ($T > 1650$ °F, or 900 °C), carbides can only be avoided by extremely high cooling rates (Path A). However, under typical industrial cooling conditions, most interstitial carbon combines with chromium to form carbides (Path B), leading to chromium depletion and reduced corrosion resistance. In contrast, Path C achieves a carburized layer while suppressing the formation of chromium-rich carbides. This process produces an extremely high carbon supersaturation, far higher than that achievable through conventional high-temperature carburizing. Within the temperature range of 350-500 °C, the diffusivity of Ni and Cr is on the order of approximately 10^{-21} m^2/s and 10^{-22} m^2/s, respectively, whereas carbon diffuses much faster, on the order of 10^{-10} to 10^{-12} m^2/s [31-33]. Such large difference in diffusion coefficient enables uniform carburization of ASS without forming detrimental carbides.

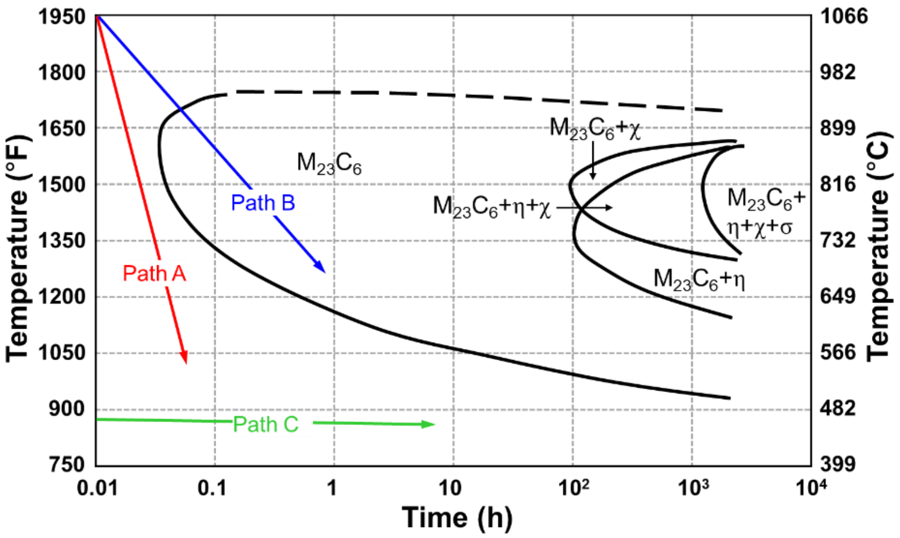

Figure 2.6 Time-temperature-transformation diagram of carbide formation in austenitic stainless steels (Redrawn from [30]).

Low-temperature carburizing (LTC) is a surface hardening technique that introduces interstitial carbon into the austenite without forming carbides. This process produces a hardened carburized layer typically of 20~35 μm thick [12,13] with surface carbon content exceeds 20 at.% due to the supersaturation of interstitial carbon. The LTC process consists of two main stages: surface activation and gaseous carburization. Surface activation is essential for removing the chromium oxide layer so that carbon can diffuse into the substrate. The chromium oxide layer on the surface of stainless steel is the main obstacle to carburizing. In industrial practice, activation can be achieved by exposing the components to a halide-containing gas mixture (such as NF_3 or HCl in N_2) at atmospheric pressure. Following activation, carburization is performed by using a mixture of unsaturated gases containing carbon and/or hydrogen such as CO and C_2H_2 [13].

In this work, LTC was performed with Bodycote's Kolsterising® S^3P K22 treatment [34]. This is a low temperature diffusion process performed at a temperature below 500 °C for several days at a very high carbon potential, which leads to carbon-supersaturated austenite without Cr-rich precipitates. As a result, surface harnesses can reach up to 1200 HV, with diffusion layer thicknesses typically ranging from 20 to 30 μm [13].

2.3.2 Carbon stabilized expanded austenite

Carbon-stabilized expanded austenite (γ_c), also known as S-phase, is a form of austenite supersaturated with interstitial carbon. The S-phase, characterized by a high carbon concentration of approximately 20 at.% and surface hardness exceeding 1000 HV, significantly enhances the wear resistance and fatigue strength of steel components [13]. During the diffusion process, the interstitial carbon gradient generates a corresponding gradient in compressive residual stress within the expanded austenite layer. Very high compressive stresses exceeding 2 GPa has been reported in the subsurface regions [35,36]. The supersaturation of carbon also causes an expansion of the austenitic lattice and increased lattice strain, which are evidenced in X-ray diffraction patterns (Figure 2.7). For AISI 304, austenite (γ) is dominant with a small amount of martensite (α'), while 304 LTC showed carbon-stabilized expanded austenite (S-phase). The diffraction peaks of the S phase are significantly shifted to lower angles and broadened.

Expanded austenite exhibits excellent corrosion resistance and often appears featureless when chemically etched. For low-temperature carburized 304 and 316, the S-phase and the underlying substrate were clearly distinguished using V2A etchant, as shown in Figure 2.8. The S-phase is featureless while grains are revealed clearly in the austenitic substrate, indicating that S-phase is nobler than substrate. In this study, LTC treatment introduced a carburized layer with a thickness of ~ 22 μm on the surface of 304 and 316. The influence of initial composition and processing conditions is insignificant. The thickness of the S-phase is similar for both cold-worked and solution-annealed samples (Figure 2.8a,b). In addition, it is not sensitive to the sample size. Similar thickness of the S-phase has been observed on bulk and thin foil 316 stainless steel (Figure 2.8c,d).

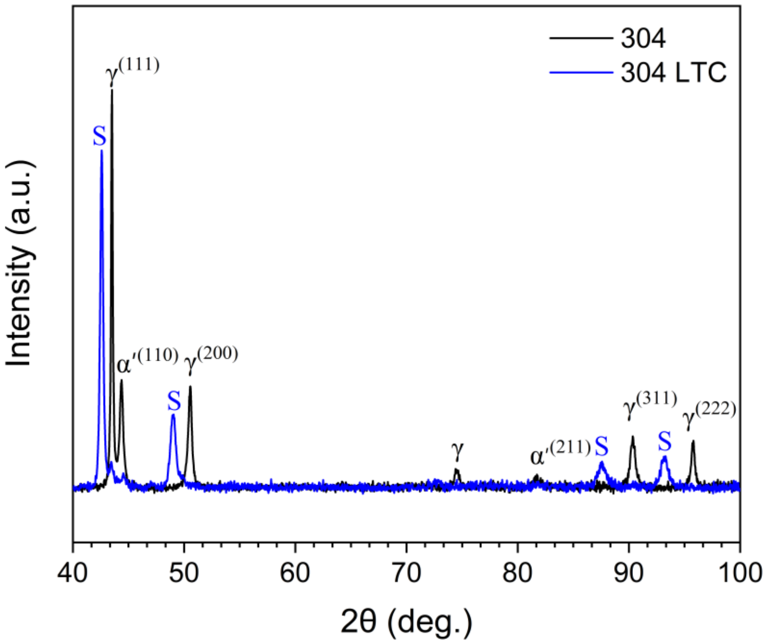

Figure 2.7 XRD patterns from solution annealed 304 with and without LTC treatment.

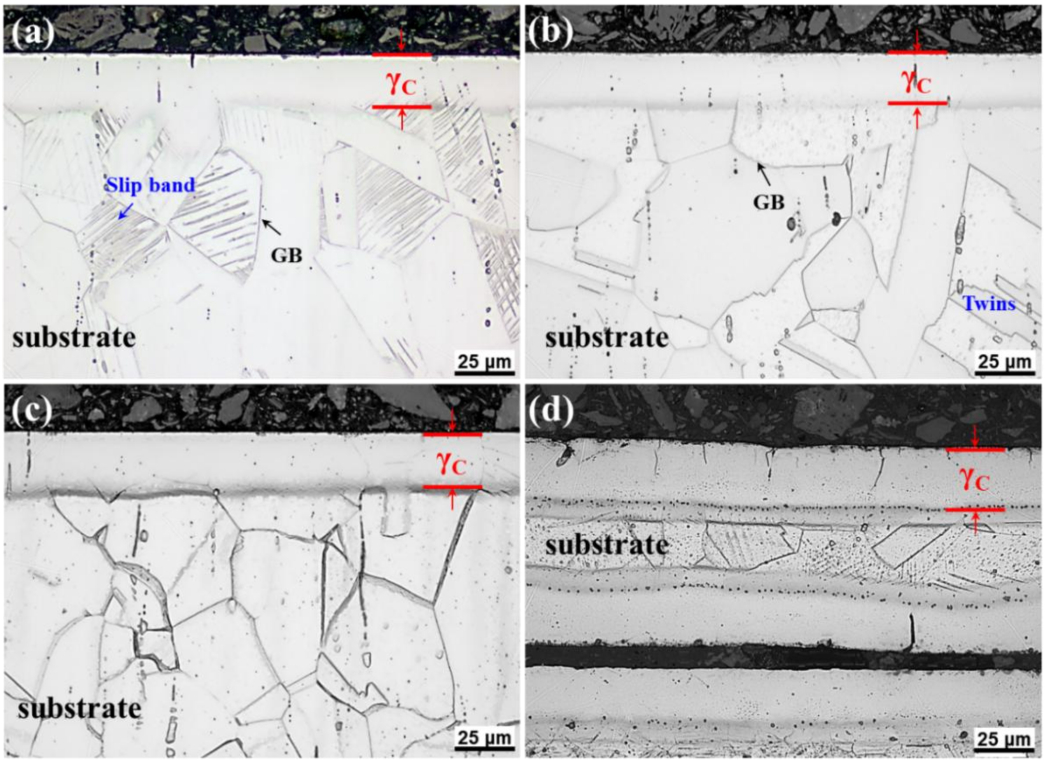

Figure 2.8 Optical micrographs of LTC samples: (a) 304 CW+LTC, (b) 304 SA+LTC, (c) 316L SA+LTC, (d) 316 SA+LTC note: CW=cold working, SA=solution annealing.

Formation of expanded austenite develops surface protrusions as a result of lattice expansion caused by the introduction of supersaturated interstitial carbon. The associated lattice distortion also produces noticeable changes in grain orientation. Figure 2.9 presents the cross-sectional microstructure of 316L after low-temperature carburizing. In Figure 2.9a, the surface protrusions, characteristic of the S-phase, are clearly visible, while Figure 2.9b highlights the orientation variations within the S-phase induced by lattice distortion. The kernel average misorientation (KAM) map further confirms the presence of high local strain within the S-phase layer.

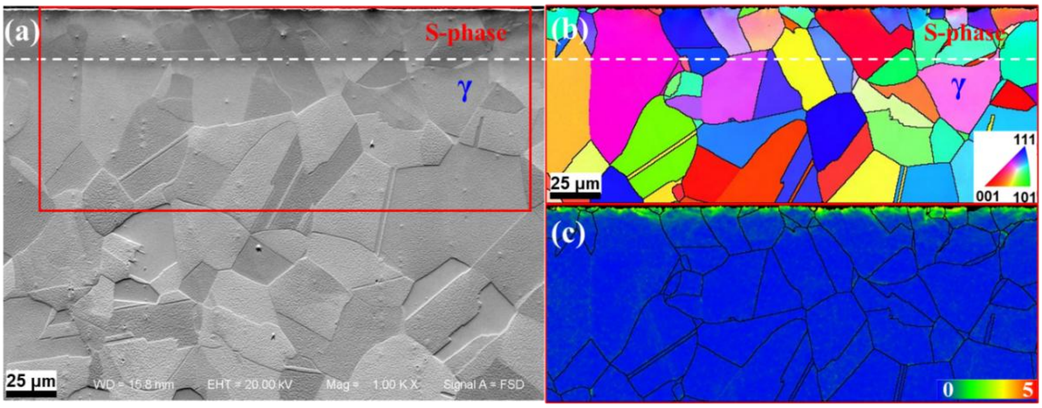

Figure 2.9 Cross-section microstructure of solution annealed 316L LTC. (a) SE image, (b) IPF map and (c) KAM map.

The carbon profile within the S-phase generally follows Fick's second law, decreasing gradually with depth from the surface. As an interstitial, carbon contributes to solid-solution strengthening; therefore, a reduction in carbon concentration results in a corresponding decline in hardness. Figure 2.10 illustrates the depth-dependent changes in carbon concentration and microhardness for 304 subjected to LTC. Both parameters decrease progressively with depth, demonstrating that the S-phase forms a diffusion-controlled, continuous carburized layer. In the substrate below the S-phase layer, the hardness eventually reaches a stable plateau. Additionally, the hardness of 304 CW+LTC is higher than that of 304 SA+LTC. This enhancement arises because cold working introduces a high density of dislocations and promotes deformation-induced martensite formation, both of which contribute to higher hardness after carburizing.

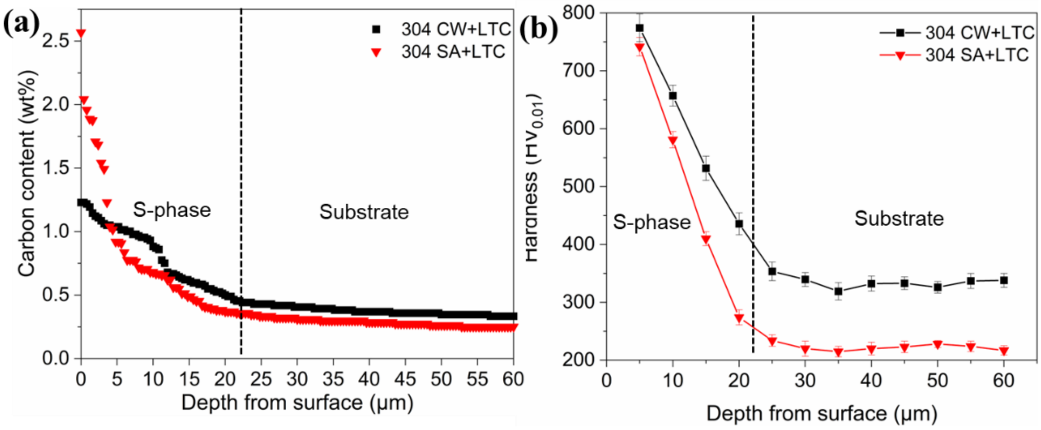

Figure 2.10 (a) Carbon concentration and (b) Vickers hardness as a function of depth for 304 LTC specimens.

2.3.3 Properties of expanded austenite

Expanded austenite exhibits exceptionally high hardness and excellent corrosion resistance. Most studies in literature have concentrated on evaluating its mechanical and corrosion performance, including hardness, tensile properties, fatigue, tribological properties and corrosion resistance [37].

Mechanical properties

The high carbon content within the expanded austenite is the primary reason for its extremely high surface hardness. Numerous studies [12-14,35-37] have shown that the hardness of the expanded austenite can reach up to approximately 1000 HV. This substantial hardening effect arises from lattice distortion induced by the supersaturated interstitial carbon.

Tensile properties are a key for structural materials. Achieving both high strength and high ductility has long been a fundamental challenge in materials design. The S-phase introduces defects such as high dislocation density and pronounces lattice distortion, which hinder dislocation motion and thereby increase hardness and tensile strength. However, the substantial lattice mismatch between the S-phase and the underlying substrate limits their ability to deform compatibly, ultimately causing a reduction in ductility, as illustrated in Figure 2.11. Notably, the extent of strengthening depends strongly on the relative thickness of the expanded austenite layer. For a cylindrical bar with a 5 mm diameter, the 22 μm S-phase layer represents only a tiny fraction of the cross section, resulting in a small strengthening effect (Figure 2.12a). In contrast, for a thin film with a thickness of 0.1 mm, the S-phase constitutes approximately 44% of the total thickness, leading to significant strengthening accompanied by a severe loss of plasticity (Figure 2.12b).

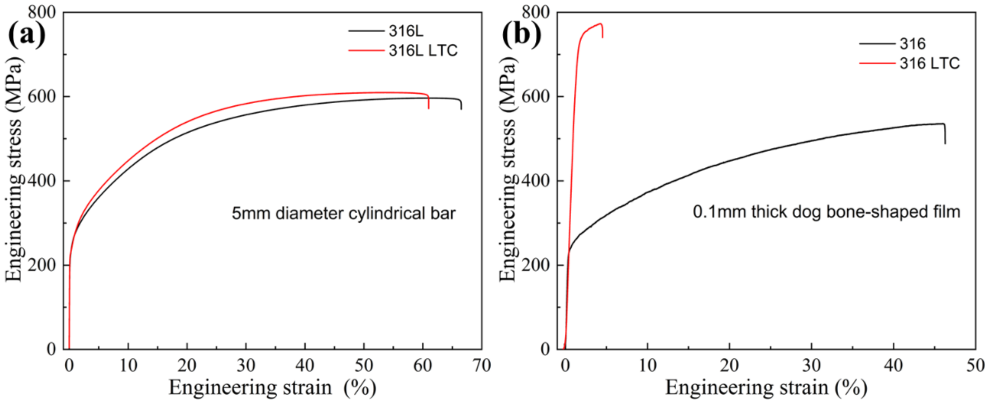

Figure 2.11 Engineering stress-strain curves of untreated and carburized specimens with different thicknesses: (a) 316L cylindrical bar with a 5 mm diameter in gauge section, (b) 316 thin specimens with a thickness of 0.1 mm.

Fatigue properties

The excellent fatigue resistance of S-phase arises from its extremely high surface hardness and residual compressive stress. For 316 stainless steel, LTC has been shown to increase high-cycle fatigue life by nearly two orders of magnitude, raise the maximum fatigue stress from ~ 200

MPa to ~ 350 MPa (~ 75%) [38], and increase the crack-growth threshold ΔK_{th} from 8 to 10 $MPa \cdot m^{1/2}$ [39]. Fatigue tests at different temperatures show that untreated 316L experiences a significant reduction in fatigue resistance at elevated temperatures, with little difference between 300–500 °C. After LTC, however, fatigue performance improves markedly. The endurance limits of carburized 316L are 252 MPa at 300 °C, 248 MPa at 400 °C, and 222 MPa at 500 °C, corresponding to improvement of 41.6%, 42.5%, and 30.5%, respectively. These improvements at elevated temperatures are greater than that observed at room temperature (~ 29.7%), with the strongest benefits appearing at 300–400 °C, followed by a decline at 500 °C [40]. These enhancements are attributed to the high strength of the carburized case layer and the substantial compressive residual stresses generated during low-temperature carburizing.

Tribological properties

Austenitic stainless steels are known for their poor tribological performance, but the high hardness of the S-phase significantly improves their wear behavior. Dry sliding wear tests at room temperature show that the wear rate of LTC-treated 316L (both ball and disc) decreases by roughly two orders of magnitude compared with untreated 316L [41,42]. Morphology examination of worn surface further highlights this improvement: untreated 316L exhibits severe plastic deformation and large flakes of wear debris, whereas LTC-treated 316L shows no such damage, demonstrating the protective effect of the hardened S-phase layer.

Corrosion resistance

ASS is often affected by localized corrosion such as pitting or crevice in chloride-containing solutions. The pitting potential of LTC-treated 316L stainless steel measured using potentiodynamic polarization in 0.6 M NaCl solution increased substantially compared to that of the untreated 316L sample [43-45]. This can be explained by the high carbon concentration on the surface. Carbon may form partial (covalent) bonds with metal atoms (Fe, Cr, Ni), inhibiting the dissolution of iron [45]. It has been shown that the S-phase improves the crevice corrosion resistance as well [46].

The potentiodynamic polarization curve in Figure 2.12a indicates that LTC treatment increases corrosion potential and pitting corrosion potential for 316L. Figure 2.13b shows that the 316L has large corrosion pits while the 316L LTC has almost no serious pitting corrosion, confirming again that S-phase has excellent corrosion resistance.

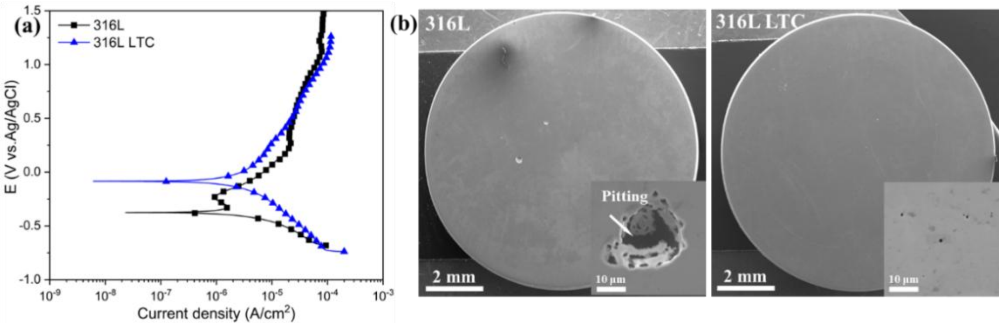

Figure 2.12 The effect of LTC on the corrosion behavior of 316L. (a) Potentiodynamic polarization curves and (b) SEM images after polarization test.

3 Hydrogen embrittlement

3.1 Hydrogen charging, fugacity and diffusion

To investigate hydrogen embrittlement, hydrogen first needs to be introduced into the material. In practice, two common methods are used: electrochemical cathodic hydrogen charging and gaseous hydrogen charging. Although gaseous hydrogen charging can reproduce some service environments, it requires complex, expensive equipment and carries risks. Cathodic hydrogen charging, by contrast, is widely used because it is inexpensive, safe, and easy to operate. In this method, the specimen is immersed in an electrolyte and subjected to cathodic polarization, either potentiostatic or galvanostatic to generate hydrogen on its surface. The cathodic hydrogen evolution reaction proceeds according to the Volmer–Tafel–Heyrovsky mechanism [47], which involves the following steps.

a) Volmer reaction: a proton (or water molecule in alkaline solution) gains an electron at the cathode and becomes an adsorbed hydrogen atom (H_{ad}) on the metal (M) surface, as indicated in eq. 3.1 and 3.2.

$$M + H^+ + e^- \rightarrow M\text{-}H_{ad} \quad \text{(acidic solution)} \qquad (3.1)$$

$$M + H_2O + e^- \rightarrow M\text{-}H_{ad} + OH^- \quad \text{(neutral or alkaline solution)} \qquad (3.2)$$

b) Tafel reaction: two adsorbed hydrogen atoms recombine on the metal surface to form molecular hydrogen, which desorbs, as shown in eq. 3.3.

$$2M\text{-}H_{ad} \rightarrow 2M + H_2\,(g)\uparrow \qquad (3.3)$$

c) Heyrovsky reaction: an adsorbed hydrogen atom reacts with a proton from the electrolyte and another electron to form hydrogen gas, as exhibited in eq. 3.4 and 3.5.

$$M\text{-}H_{ad} + H^+ + e^- \rightarrow M + H_2\,(g)\uparrow \quad \text{(acidic solution)} \qquad (3.4)$$

$$M\text{-}H_{ad} + H_2O + e^- \rightarrow M + OH^- + H_2\,(g)\uparrow \quad \text{(neutral or alkaline solution)} \qquad (3.5)$$

d) Hydrogen absorption: adsorbed hydrogen is converted into dissolved absorbed hydrogen (eq. 3.6).

$$M\text{-}H_{ad} \rightarrow M\text{-}H_{ab} \qquad (3.6)$$

Atomic hydrogen recombines at the metal surface through electrochemical recombination (Heyrovsky reaction) or molecular recombination (Tafel reaction) to form molecular hydrogen H_2. Since molecular hydrogen cannot be absorbed by the metal lattice, it needs to be dissociated into atomic hydrogen, which is then absorbed by a metal, a process similar to gaseous hydrogen charging.

It is worth noting that the surface hydrogen concentration during electrochemical hydrogen charging depends on hydrogen fugacity. The effective hydrogen pressure (fugacity) f_{H_2}on the hydrogen-charged surface can be thermodynamically described using the Nernst equation, as shown in eq. 3.7 [48,49].

$$f_{H_2} = \alpha exp\left(-\frac{\eta F}{\beta RT}\right) \tag{3.7}$$

Where, α and β are empirical constants fitted from experiment. F is the Faraday constant, R is the gas constant, T is the absolute temperature in K, η refers to the overpotential, which can be obtained from eq. 3.8.

$$\eta = E_C - E_H^0 \tag{3.8}$$

Where E_C is the applied cathodic potential, E_H^0 is the equilibrium potential for the hydrogen evolution reaction (HER) at one atmosphere, which can be determined from eq. 3.9 [50].

$$E_H^0 = -0.0591 \times pH - 000295 log f_{H_2} \tag{3.9}$$

As shown in eq. 3.7-3.9, hydrogen fugacity is affected by overpotential, temperature, and pH value. Ref. [51] reports that the hydrogen fugacity of 99.99% iron in 1N H_2SO_4 (acidic) at 24 °C with a current density of 4.5 mA/cm^2 is 1.2×10^8 atm. Ref. [52] reports that the hydrogen fugacity of Armco iron in 0.1N NaOH (alkaline) at 25°C with a current density of 8.1 mA/cm^2 is 2.2×10^1 atm. These findings indicate that hydrogen charging under acidic conditions can significantly increase hydrogen fugacity.

According to Sievert's law, the equilibrium hydrogen concentration C_H on the charging side is linked to hydrogen fugacity, which applies for both gas and electrolytic charging conditions, as given in eq. 3.10 [49].

$$C_H = k_s\sqrt{f_{H_2}} \tag{3.10}$$

Where C_H is hydrogen concentration in the metal, $f_{H_2}$is hydrogen fugacity or gas partial pressure, k_s is Sieverts' constant (temperature-dependent solubility coefficient). Equation 3.10 shows that hydrogen concentration is significantly affected by hydrogen fugacity. Electrochemical hydrogen charging has a hydrogen fugacity as high as ~ 10^8 bar in acid, while gaseous hydrogen charging is generally below 10^3 bar, indicating that the former has a higher concentration of hydrogen absorbed compared to the later.

Once hydrogen is absorbed, it diffuses into the material structure driven by the concentration gradient. In general, diffusion can be expressed by Fick's first law and second law. Fick's first law describes the steady-state diffusion, as expressed by eq. 3.11.

$$J = -D\frac{\partial c}{\partial x} \tag{3.11}$$

Where J represents the diffusion flux, D represents the diffusion coefficient, and $\partial c/\partial x$ is the concentration gradient. Diffusion flux and concentration gradient do not change with time in steady state diffusion. The negative sign in eq. 3.11 indicates that the diffusion flux always flows from the higher concentration region to the lower concentration region.

Fick's second law describes non-steady-state diffusion and explains how concentration changes with time and diffusion distance. It is expressed by eq. 3.12, where $\partial c/\partial t$ represents the change in concentration with time, and $\partial^2 c/\partial x_2$ is the second derivative of concentration for distance, capturing the spatial variation of the concentration gradient.

$$\frac{\partial c}{\partial t} = D\frac{\partial^2 c}{\partial x^2} \qquad (3.12)$$

The rate of hydrogen diffusion depends on factors such as microstructure, temperature, pressure and defects. The hydrogen diffusion coefficient D, as an important parameter for evaluating hydrogen diffusivity, is temperature dependent. It can be expressed by the Arrhenius equation in eq. 3.13.

$$D = D_0 \cdot exp\left(-\frac{Q}{RT}\right) \qquad (3.13)$$

Where D_0 is the pre-exponential factor or Arrhenius factor. Q represents the activation energy which is dependent on the diffused element and the crystal structures. R is the universal gas constant, and T is the absolute temperature.

3.2 Hydrogen distribution in the microstructure

Materials inherently contain a wide variety of defects, including vacancies, solute atoms, dislocations, grain boundaries, phase interfaces, triple junctions, and precipitates. In addition to these common microstructural features, more complex defects such as microcracks, nanocracks, surface steps, voids, and even surface oxide layers may also be present, as illustrated in Figure 3.1. These imperfections create numerous energetically favorable sites that can interact with diffusing species. Hydrogen atoms have extremely small radius and high mobility, making them readily migrate within materials and be captured by numerous defect sites. To more accurately describe its distribution and behavior within the microstructure, hydrogen is generally categorized into two forms: lattice hydrogen, which occupies regular interstitial sites, and trapped hydrogen, which is bound to specific defects. The variations in trapping behavior are a major factor underlying the wide differences in hydrogen-embrittlement susceptibility among different microstructures. In addition, the distribution of hydrogen strongly depends on the type, fraction, and morphology of each phase existed.

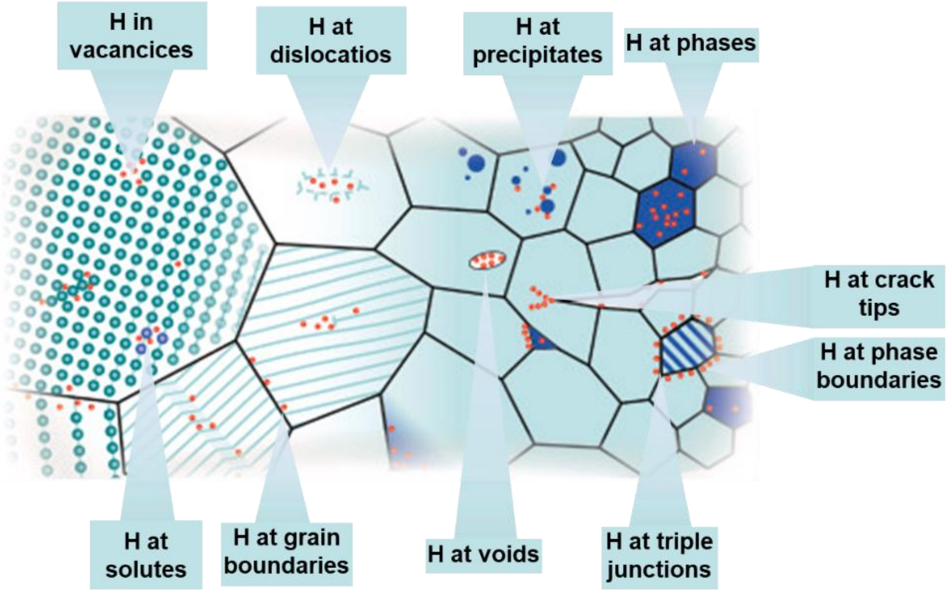

Figure 3.1 The distribution of hydrogen within the bulk material. Reproduced from reference [53], with the permission of Elsevier.

For face-centered cubic (FCC) and body-centered cubic (BCC) metals, lattice hydrogen primarily occupies octahedral and/or tetrahedral interstitial sites, where the available spacing is energetically favorable for accommodation [54] (see Table 3.1 and Figure 3.2). The atomic radius of hydrogen is 0.55 Å. Assuming that only one octahedral/tetrahedral interstitial site in a unit cell can be occupied by hydrogen, the hydrogen solubility can be roughly estimated. For γ-Fe (FCC) unit cell, there are 4 Fe atoms and 1 H atom. The octahedral interstices correspond to a theoretical maximum of 20 at.% hydrogen (equivalent to 4440 wppm). For α-Fe (BCC) unit cell, there are 2 Fe atoms and 1 H atom. This corresponds to a maximum capacity of 33 at.% hydrogen (equivalent to 8850 wppm). However, in practice, the measured hydrogen concentrations are far below these theoretical limits. Moreover, the hydrogen solubility in γ-Fe is significantly higher than that in α-Fe [55]. In γ-Fe (austenite), the octahedral sites provide larger interstitial volumes, leading to significantly higher hydrogen solubility compared with α-Fe and α′-Fe (ferrite and martensite). In contrast, BCC metals having a lower atomic packing factor contain a larger number of interstitial sites, promoting much faster hydrogen transport. As a result, the diffusion coefficient of hydrogen in ferrite or martensite is several orders of magnitude higher than that in austenite [55].

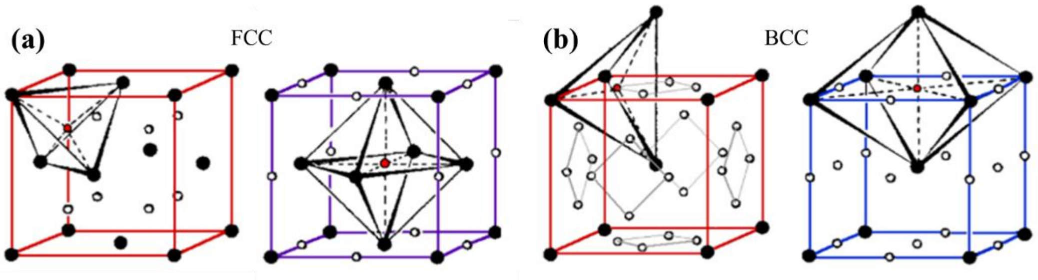

Figure 3.2 Schematic representation of tetrahedral and octahedral interstices for (a) FCC and (b) BCC crystal structures[54].

Table 3.1 Number of interstitial sites and available spacing for foreign atoms in BCC and FCC crystal structures

Crystal structure	Octahedral interstices		Tetrahedral interstices		Atomic packing factor
	Number	Radius [Å]	Number	Radius [Å]	
BCC	6	0.19	12	0.36	0.68
FCC	4	0.53	8	0.29	0.74

It is worth noting that lattice hydrogen causes lattice expansion, thereby altering the stress state, as shown in Figure 3.3a. During diffusion, the surface hydrogen concentration is higher than that of the substrate, creating a residual stress gradient. Under the constraint of the substrate, there is compressive residual stress, while underneath the interstitial enrichment region, due to lattice expansion, there will be a tensile residual stress state. The X-ray diffraction pattern of 316L after hydrogen charging in Figure 3.3b shows that the diffraction peaks of hydrogen-expanded austenite broaden and shift to lower angles, indicating an increased lattice parameter and strain.

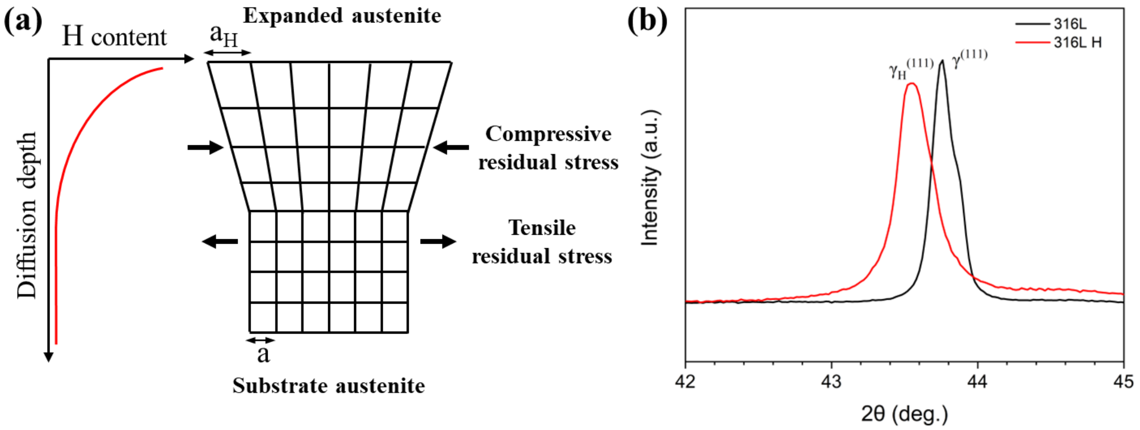

Figure 3.3 (a) Schematic lattice stress-strain state induced by hydrogen expanded austenite formation and (b) XRD pattern of solution-annealed 316L with hydrogen charging.

For trapped hydrogen, defects such as dislocations, precipitates, and grain boundaries can act as hydrogen traps, each with different trapping binding energies. In general, precipitates have higher binding energies than grain boundaries or dislocations [53]. Low binding energy traps (typically 10~40 kJ/mol) can readily release hydrogen at or near room temperature, acting as reservoirs for diffusible hydrogen and thus contributing to hydrogen embrittlement. In contrast, high binding energy traps bind hydrogen more strongly, reducing its mobility and often mitigating hydrogen embrittlement. Therefore, introducing high binding energy traps can be an effective strategy to reduce hydrogen embrittlement susceptibility.

3.3 Hydrogen embrittlement mechanisms

The phenomenon of hydrogen embrittlement was first observed by Johnson [56] in the late 19th century. Since then, extensive research has been devoted to understanding its underlying mechanisms. With in-depth research, different views on the mechanism of hydrogen embrittlement have emerged. Experimental and simulation results seem to indicate that it is impossible to select a single mechanism to explain all hydrogen-related failures. In this section, several mechanisms proposed so far are listed.

3.3.1 Hydrogen-enhanced decohesion (HEDE)

In 1926, Pfeil [57] studied the effect of occluded hydrogen on the tensile strength of iron and concluded that "occluded hydrogen has a remarkable weakening effect on intercrystalline boundary" and "In addition to its effect on the boundaries, hydrogen decreases the cohesion across the cubic cleavage planes". Building on this early insight, Troiano [58] proposed in 1959 that hydrogen reduced the intrinsic fracture strength of transition metal lattices (Fe, Co, Ni). He suggested that electrons from the hydrogen 1s orbit could enter the partially filled 3d orbit of the transition metal, increasing the interatomic repulsive force and thereby lowering the cohesive strength of the lattice. This mechanism was subsequently refined by Oriani, McMahon and Gerberich [59-61]. Figure 3.4 schematically illustrates the HEDE mechanism. In this model, atomic bonds are weakened by (i) hydrogen within the crystal lattice (ii) adsorbed hydrogen and (iii) hydrogen at the particle-matrix interface. The essence of this mechanism is that interstitial hydrogen reduces the cohesive energy within the lattice or grain/phase boundaries. As a result, hydrogen accumulation at crack tips, high hydrostatic pressure and defects lower the critical stress required for decohesion. Intergranular fracture and cleavage morphologies are typical features of the HEDE mechanism.

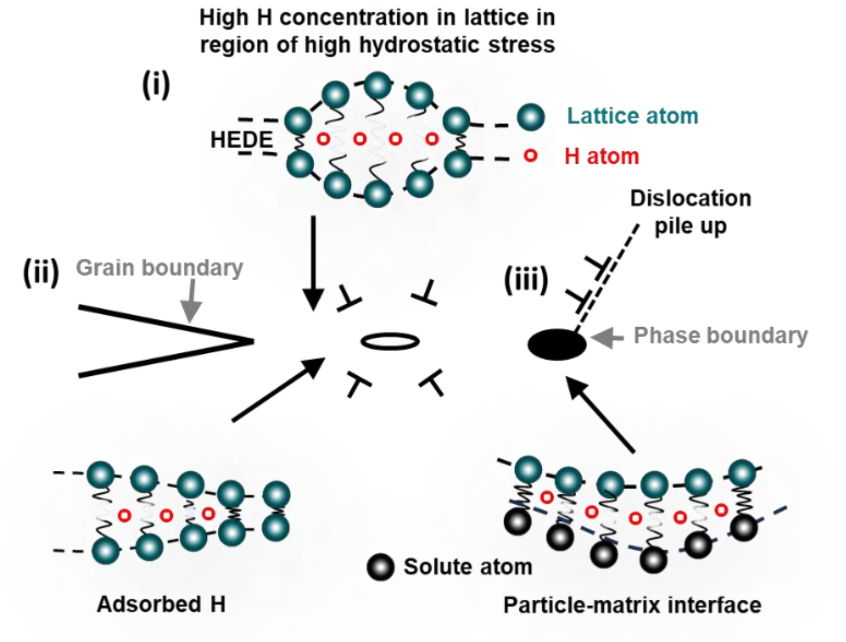

Figure 3.4 Schematic of HEDE mechanism: hydrogen weakens interatomic bonds (i) in the lattice, (ii) at a grain boundary, and (iii) at particle–matrix interfaces, leading to tensile separation. Reproduced from [55] with permission from Elsevier.

3.3.2 Hydrogen-enhanced localized plasticity (HELP)

In 1972, Beachem [62] proposed a hydrogen enhanced localized plasticity model to explain hydrogen-assisted cracking. The model suggests that when a sufficient concentration of hydrogen dissolved into the lattice ahead of the crack tip, it facilitates deformation process allowed by the microstructure. Bimbaum, Robertson, and Sofronis [63-67] performed in-situ TEM in a gaseous hydrogen environment and verified that hydrogen can lower the stress required for dislocation motion. In essence, hydrogen promotes dislocation activity and intensifies strain localization, in part through the formation of microvoids. As illustrated in Figure 3.5, these localized microvoids eventually coalesce, leading to crack initiation and propagation. The high hydrostatic stress at the crack tip enhances hydrogen accumulation, thereby accelerating localized plastic deformation. Consequently, the hydrogen-affected zone experiences significantly higher strain than the hydrogen-free region, resulting in premature fracture. Fractography associated with the HELP mechanism typically includes microvoid coalescence and shallow dimples. Overall, the HELP model suggests that hydrogen-induced cracking arises primarily from enhanced local plasticity rather than from the reduction of atomic cohesive strength, as proposed by the HEDE mechanism.

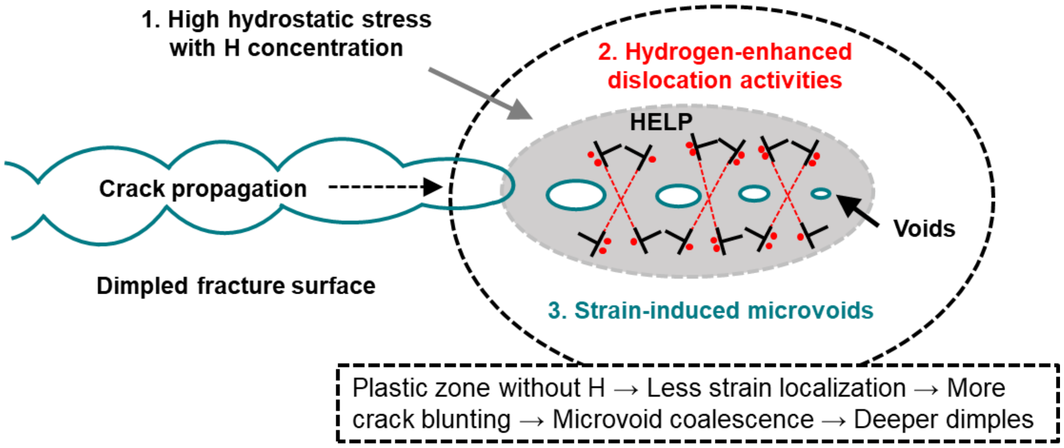

Figure 3.5 Schematic of HELP mechanism: regions of high hydrogen concentrations promote localized plasticity and microvoid coalescence. Reproduced from [55] with permission from Elsevier.

3.3.3 Adsorption-induced dislocation emission (AIDE)

The essence of the AIDE mechanism is the same as the HELP mechanism, both of which involve hydrogen-induced plasticity. The absorption of hydrogen leads to the weakening of the interatomic bonding, which accelerates dislocation emission and nucleation and growth of micro-voids at the crack tip. The AIDE concept was first proposed by Lynch [68-71] through studies on environment-assisted cracking. According to this mechanism, hydrogen absorption at the crack tip accelerates the emission of dislocations, facilitating both their nucleation and subsequent movement, which in turn promotes the coalescence of cracks with the void ahead of cracks. A characteristic feature of the AIDE mechanism is the formation of microvoids at the intersection of slip bands ahead of the crack tip under continuous stress or monotonically increasing stress. Figure 3.5 presents a schematic illustration of the AIDE mechanism at the crack tip.

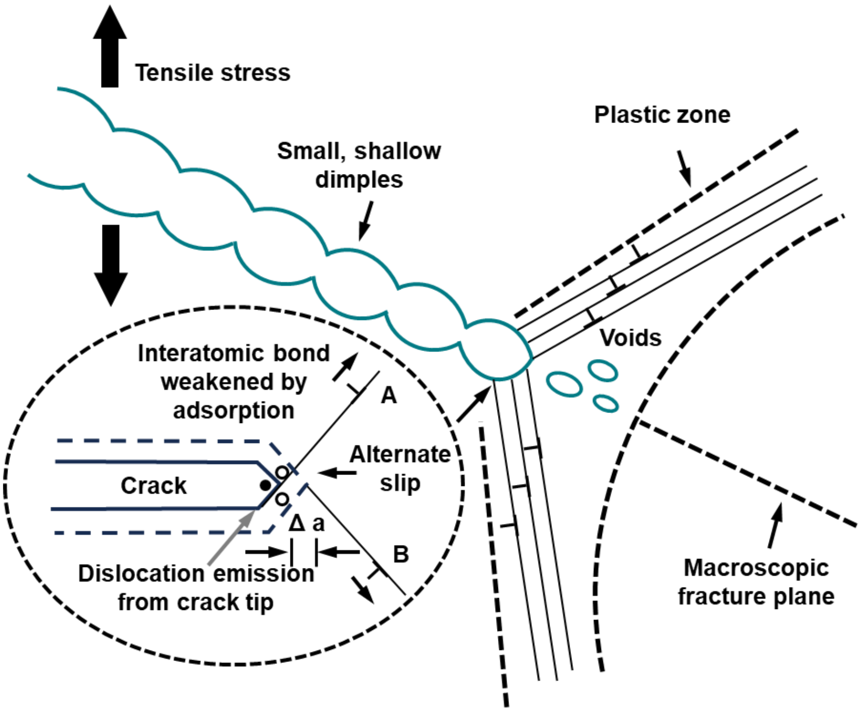

Figure 3.6 Schematic of AIDE mechanism: stress-induced crack grows via alternating slip at crack tips, promoting coalescence with voids in the plastic zone. Reproduced from [55] with permission from Elsevier.

3.3.4 Hydrogen-enhanced strain-induced vacancy (HESIV)

Nagumo [72,73] reported that hydrogen enhances strain-induced vacancy (HESIV) formation and vacancy clustering, based on measurements obtained using newly developed low-temperature thermal desorption spectroscopy (LTDS) and positron lifetime spectroscopy (PAS). The HESIV mechanism can be directly validated because vacancies serve as hydrogen traps and are highly sensitive to temperature, making hydrogen an effective tracer for lattice defects. PAS provides additional support for the HESIV mechanism. The average positron lifetime τ_m in iron increases markedly with tensile strain, and the increase becomes more pronounced when the material is pre-charged with hydrogen prior to straining, consistent with hydrogen-enhanced formation of vacancy-type defects. Hydrogen-induced blistering is a macroscopic feature of HESIV. Numerous studies have reported hydrogen blistering in pure iron and ferritic steels during cathodic hydrogen charging [74,75]. The low hydrogen solubility of bcc-Fe makes it easy for hydrogen to accumulate at vacancies, and strain induces the aggregation and growth of vacancies, thus forming hydrogen blistering.

3.3.5 Defect acting agent (DEFACTANT)

Defect acting agent (DEFACTANT) mechanism provides a thermodynamic framework for understanding hydrogen-assisted degradation in metals. It was proposed first by Kirchheim and co-workers, based on the principle that solute segregation at defects lowers surface energy according to the Gibbs adsorption isotherm [76-78]. According to the principle of minimizing the total free energy of a thermodynamically stable system, hydrogen segregation reduces the formation energy of vacancies, dislocations, grain boundaries, voids, and crack surfaces [79]. Experimental evidence supporting this mechanism comes from in situ electrochemical hydrogen charging nanoindentation experiments on nickel, which show that dissolved hydrogen lowers the activation energy for the onset of plasticity by facilitating dislocation nucleation [80]. Compression tests on α-vanadium microcolumn demonstrate that compressive stress increases with increasing hydrogen concentration. Hydrogen facilitates dislocation formation, leading to increased dislocation density and, consequently, higher strength through forest hardening. This hydrogen-enhanced dislocation generation aligns with the DEFACTANT concept, which predicts that hydrogen lowers the line energy of dislocations. Thus, the observed hydrogen–dislocation interaction can be attributed to a reduction in dislocation formation energy [81]. Studies on annealed Pd with charged hydrogen further confirm this behavior. Hydrogen stabilizes vacancies by significantly lowering their formation energy. When the hydrogen content exceeds 0.017 H/Pd, PdH particles form. The stress associated with hydride growth induces plastic deformation, generating additional dislocations and vacancies [82]. In summary, the DEFACTANT mechanism offers a unified, thermodynamic explanation for many hydrogen-induced phenomena. By reducing defect formation energies, hydrogen acts as an active "defect catalyst," enhancing plastic deformation, accelerating damage accumulation, and promoting hydrogen-assisted cracking.

3.4 Factors affecting hydrogen embrittlement

HE is influenced by multiple factors, which can be broadly classified into three categories: hydrogen sources, loading conditions, and material characteristics [83], as summarized in Figure 3.7.

Hydrogen sources include internal hydrogen and external hydrogen. Internal hydrogen refers to hydrogen introduced during manufacturing and processing, such as welding, electroplating, electropolishing, pickling, and heat treatment. External hydrogen is introduced from the environment. Gaseous charging and electrochemical charging [84] are common methods for introducing external hydrogen. Gaseous hydrogen charging is influenced by temperature, pressure, and gas composition. Elevated temperatures enhance hydrogen diffusion [55], while higher pressures increase solubility [49], raising embrittlement risk. Electrochemical hydrogen uptake depends on electrolyte composition, temperature, and pH [21]. Acidic solutions and high overpotentials accelerate hydrogen evolution and subsequent absorption into the metal [48]. Once inside, hydrogen occupies interstitial sites, with its mobility and concentration determining susceptibility to embrittlement.

Mechanical loading strongly interacts with hydrogen to influence cracking behavior. Under monotonic loading, low strain rates allow hydrogen to accumulate at stress concentrators [85], while pre-strain generates dislocations that increase local hydrogen concentration [86]. Notches or surface irregularities amplify local stresses, facilitating crack initiation [87]. Under cyclic loading, low frequencies provide sufficient time for hydrogen to diffuse to crack tips, promoting crack propagation. The stress ratio R influences crack closure and hydrogen accumulation. In-situ and ex-situ testing can lead to varied degrees of observed embrittlement due to differences in hydrogen diffusion behavior and its spatial distribution within the material [88].

Material factors further determine HE susceptibility. Surface roughness and oxide layer control hydrogen absorption and permeation [89]. Tensile residual stress and microcrack promote hydrogen-induced crack propagation. Bulk characteristics, including grain size, precipitates, phase boundaries, and lattice defects control hydrogen trapping and crack propagation [90]. Fine grains increase boundary density, which can both trap hydrogen and facilitate crack growth [91]. Precipitates and intermetallic compounds interact with hydrogen differently, while vacancies and dislocations locally elevate hydrogen concentration, promoting decohesion [53].

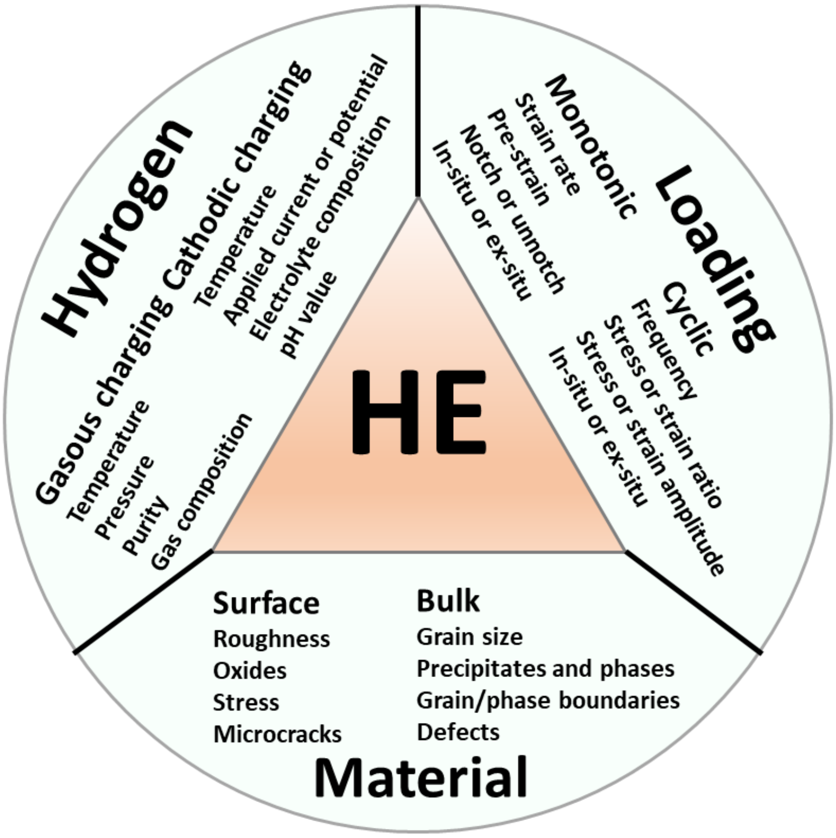

Figure 3.7 Schematic of factors affecting HE. The three regions surrounding the triangle represent the main categories of typical influencing factors [83]. Reproduced with permission from ACS Publications.

To quantitatively evaluate susceptibility to HE, the embrittlement index (EI) is commonly used to convey the effect of some external and internal factors. In principle, EI is the ratio between the relative loss of mechanical properties in hydrogen and the original value in an inert environment, as shown in eq. 3.14.

$$EI = \frac{X_0 - X_H}{X_0} \tag{3.14}$$

Where X_0 denotes the original mechanical properties in air, such as elongation, reduction of area, or ultimate tensile strength. Similarly, X_H represents the mechanical properties under hydrogen-containing conditions.

Figure 3.8 summarizes several key factors that influence the EI [92]. Among these, hydrogen content is the most critical. Increasing hydrogen concentration generally increases EI and may shift the dominant fracture mode. As the hydrogen content increases, the fracture morphology progressively transitions from deep dimples to shallow microvoid coalescence, followed by quasi-cleavage, cleavage, and ultimately intergranular fracture [93]. However, a saturation concentration often exists beyond which additional hydrogen has little effect. This behavior is attributed to the homogenization of hydrogen distribution, which reduces stress-assisted fracture driven by concentration gradients [94]. Temperature also plays a significant role. HE tends to be most severe near room temperature and diminishes at both lower and higher temperatures [95]. At very low temperatures, hydrogen diffuses very slowly and exists almost entirely as trapped hydrogen, whereas at elevated temperatures, diffusible hydrogen escapes and trapped hydrogen predominates [96]. The effect of strain rate is closely tied to hydrogen diffusion. At low strain rates, hydrogen has sufficient time to migrate to defects and crack tips, promoting crack initiation and growth. In contrast, high strain rates (e.g., impact loading) limit hydrogen diffusion, resulting in minimal embrittlement [94]. Many studies indicate that the EI correlates with material strength [83,97]. High-strength alloys generally exhibit pronounced HE, whereas softer metals are typically more resistant. Nonetheless, microstructure often exerts a stronger influence than strength alone. Features such as grain size and phase composition can either enhance or mitigate HE. Consequently, strength cannot be used as a universal parameter to compare EI across materials with different microstructures.

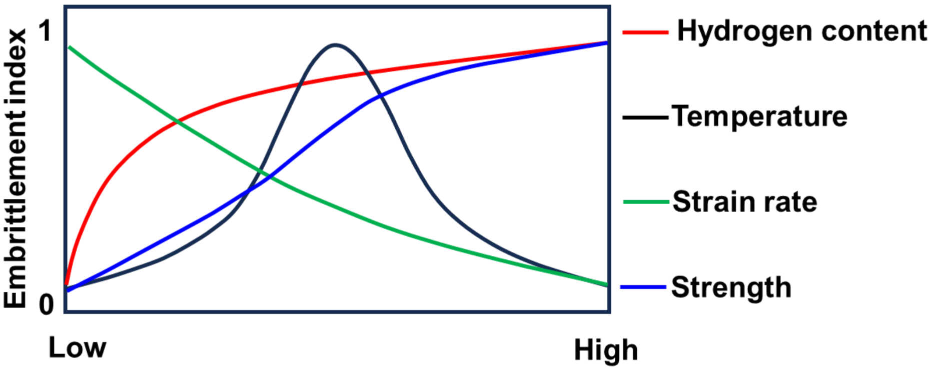

Figure 3.8 Schematic plots of the dependence of embrittlement index on hydrogen content, temperature, strain rate and strength [92]. Reproduced with permission from Springer Nature.

4 Materials and methodology

4.1 Materials and sample preparation

The materials used in this study are three types of austenitic stainless steels with different compositions, and their nominal chemical composition are listed in Table 4.1. For 304 and 316L, the as-received conditions were cold-drawn bars, part of which were solution annealed at 1050 °C for 1 hour followed by water quenching to obtain solution-annealed samples. The microstructure of cold worked and solution annealed 304 are shown in Figure 4.1. Cold working introduces a high density of defects and low-angle grain boundaries (LAGB), indicating significant microstructural deformation, whereas solution annealing removes most deformation-induced defects and produces equiaxed grains dominated by high-angle grain boundaries (HAGB). 3015 is a precipitation hardenable austenitic stainless steel, and the as-received samples were in the aged condition. In addition, some 304 and 316L underwent low-temperature carburizing using the Bodycote Kolsterising® K22 process, which is performed at a temperature below 500 °C for several days at a very high carbon potential. Its characteristics and effects have been widely reported in the literature [98,99]. For ease of description, the material conditions examined in this study are summarized in Table 4.2.

Table 4.1 The nominal composition of austenitic stainless steels investigated (wt%).

ID	**C**	**Mn**	**Si**	**Cr**	**Ni**	**Mo**	**Nb**	**Ti**	**Al**	**Fe**
304	0.06	1.6	0.4	18.2	8.0	-	-	-	-	Bal.
316	0.06	2.0	0.4	16.5	10.5	2.0	-	-	-	
316L	0.02	1.6	0.4	16.7	10.1	2.0	-	-	-	Bal.
3015	0.2	0.8	0.4	15.0	30.0	0.2	2.0	3.0	2.0	Bal.

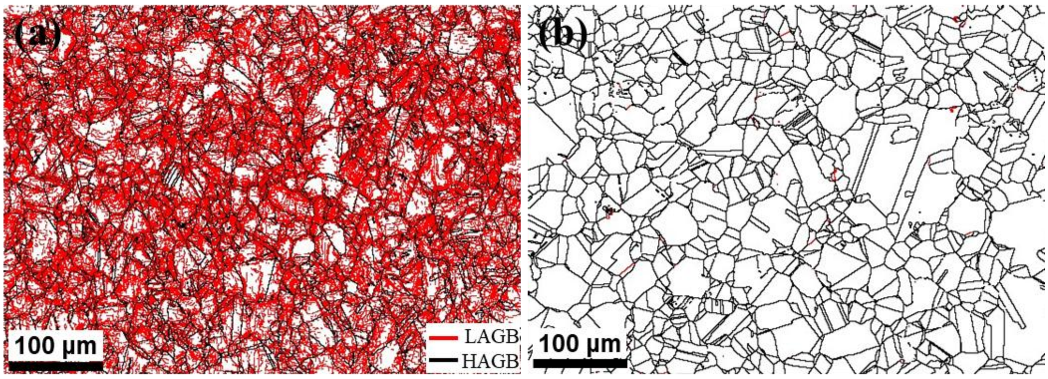

Figure 4.1 Microstructure of (a) cold worked and (b) solution annealed 304.

Table 4.2 Sample designations and their processing conditions

Name of samples	Conditions
CW	Cold-worked
SA	Solution-annealed
CW-H	H-charging of cold-worked steel
-H/SA-H	H-charging of solution-annealed steel

CW+LTC	Cold-worked steel treated by LTC
SA+LTC	Solution-annealed steel treated by LTC
CW+LTC-H	Carburized cold-worked steel followed by H-charging
SA+LTC-H	Carburized solution-annealed steel followed by H-charging
LTC-H	Carburized solution-annealed steel followed by H-charging
LTC H-3d	Carburized solution-annealed steel followed by H-charging 3 days

The metallographic samples were mounted in conductive resin and plane ground using 500# SiC paper, followed by fine grinding with a 9 μm diamond suspension. Polishing was then carried out sequentially with 3 μm and 1 μm diamond suspensions, with OPS (oxide polishing suspensions) as the final polishing step. To reveal and evaluate the S-phase, the samples were etched with V2A reagent (119 mL HCl, 12 mL HNO_3, 119 mL H_2O) for 10 s at room temperature.

4.2 Cathodic hydrogen charging

In this thesis study, hydrogen was introduced into the materials using an electrochemically cathodic charging method. It is well established that parameters such as electrolyte, temperature, current density, and charging duration significantly influence hydrogen diffusion and uptake. Common electrolytes for hydrogen charging include H_2SO_4, NaCl, and NaOH aqueous solutions. To compare the effects of different electrolytes on hydrogen uptake, three solutions were selected in this study: 0.2 mol/L H_2SO_4, 3 wt% NaCl, and 0.2 mol/L NaOH. To inhibit hydrogen recombination at the surface, each electrolyte was supplemented with either 1 g/L Na_2HAsO_4 or 0.3 wt% NH_4SCN [100,101] as a hydrogen poison to avoid recombination of hydrogen. Hydrogen charging was conducted at 80 °C using current densities between 0.3 and 30 mA/cm^2 for durations ranging from 1 to 168 hours. Because different sections of this thesis focus on different research objectives, the specific charging parameters vary; detailed conditions are listed in the appendix papers. It is important to note that H_2SO_4 contains a high concentration of H^+, resulting in substantially higher hydrogen generation compared with NaCl and NaOH solutions. However, its strong corrosiveness is a notable drawback. H_2SO_4 is commonly used to simulate hydrogen uptake under highly aggressive service environments.

4.3 Characterization techniques

4.3.1 Optical microscopy

Optical microscopy (OM) uses visible light to magnify and visualize specimens, making it a common tool for examining the microstructures of geological, biological, and metallic materials. Because its practical resolution limit is about 0.2 - 0.3 μm, OM is well suited for observing features on the micrometer scale. This technique provides spatial information by recording how features are distributed across the image plane. Measured distances in the image maintain a fixed proportionality to distances in the actual specimen, determined by the microscope’s magnification (Figure 4.2). In this study, OM images were obtained using a Zeiss Axioscope 7 optical microscope.

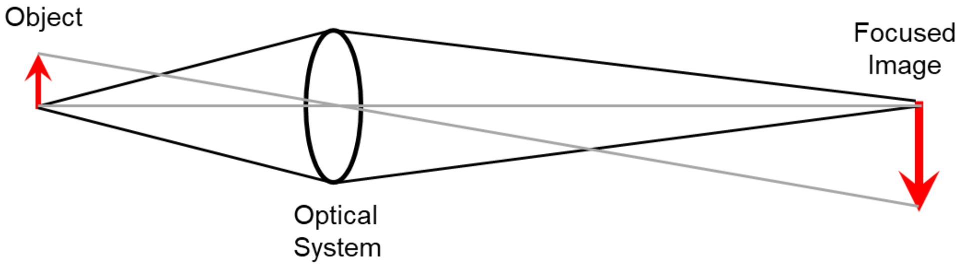

Figure 4.2 Schematic representations of an optical image.

4.3.2 Scanning electron microscopy

When the electron probe hits the sample surface, it produces various signals due to different interactions between the electrons and the sample. These interactions yield several types of signals including Auger electrons, secondary electrons, backscattered electrons, characteristic X-rays and continuous X-rays (Figure 4.4). Scanning electron microscopy (SEM) creates magnified images by scanning a focused electron beam over the surface of the sample. In SEM, the electrons emitted by the electron gun are accelerated by the electric field to the anode. The high-energy electron beam (1~30 keV) is obtained and converged into an electron probe through the electromagnetic lens. In this work, the microstructures and fracture morphologies of the samples were examined using Zesiss Gemini 450 FE-SEM and LEO Gemini 1550 FE-SEM. The working distance was 8-15 mm and the accelerating voltage was set at 15 - 20 kV.

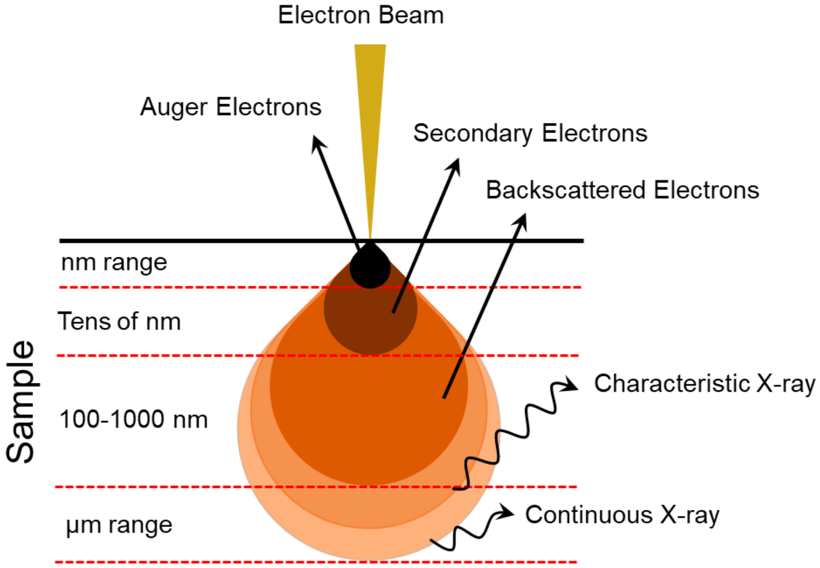

Figure 4.3 Schematic of signals generated by the interaction between electron beam and sample.

4.3.3 Electron backscatter diffraction

Electron back-scatter diffraction (EBSD), originated from Kikuchi's discovery of electron diffraction in mica sheets. It is a microstructural-crystallographic technique usually assembled on the SEM. When the sample surface is irradiated by the electron beam, high-energy backscattered electrons undergo Bragg diffraction, forming Kikuchi patterns on the EBSD detector. These diffraction patterns are determined by the spacing of lattice planes and the crystal structure. By indexing the patterns using known crystal structure databases and unit cell parameters, EBSD provides detailed information on grain orientation, grain boundary character, and phase distribution etc.

The schematic diagram of the EBSD setup is shown in Figure 4.4. During collection, the sample was tilted to 70° to maximize the signal intensity reaching the detector. In the present work, EBSD was performed using a Zessis Gemini 450 FE-SEM coupled with a Symmetry detector. The accelerating voltage was set to 20 kV, and the working distance was 14 mm. The scan step size of EBSD map acquisition was 0.1 - 5 µm. Offline pattern matching indexing was performed using MapSweeper in the AZtecCrystal EBSD data processing software to improve indexing rate. HKL* Channel 5 software was used for data post-processing. The maps involved include image quality (IQ), inverse pole figure (IPF), grain boundary (GB), phase and kernel average misorientation (KAM) maps. High-angle grain boundaries (misorientation >15°) are shown as black lines in the maps.

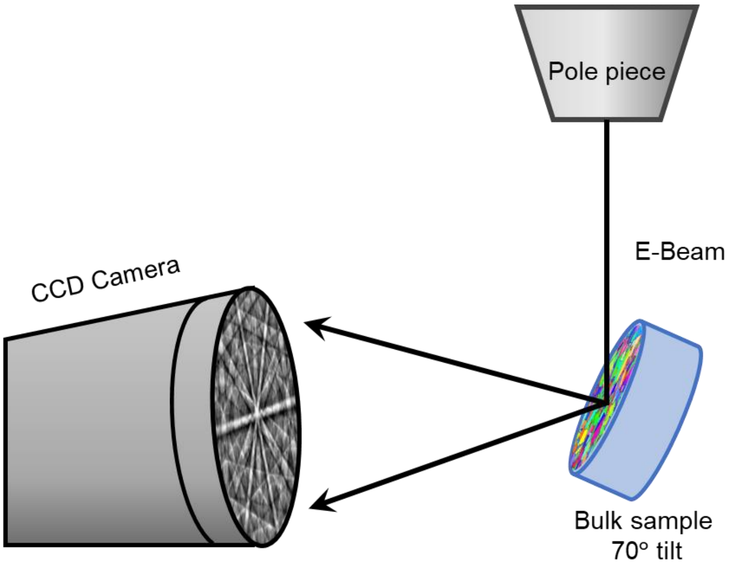

Figure 4.4 The schematic diagram of EBSD collection.

4.3.4 Transmission electron microscopy

Transmission electron microscopy (TEM) uses a transmitted or scanned transmitted electron beam to image thin film samples (20-200 nm thick). TEM can be used to perform high spatial resolution imaging up to atomic scale and to obtain crystallographic and chemical information from samples. In TEM mode, the parallel electron beam through the sample generates unscattered or elastically scattered electrons. The unscattered electrons are used to obtain a bright field (BF) image of the sample. This imaging mode provides thickness and diffraction contrast.

In this study, TEM foils were polished using a dual-jet electropolisher (Struers, TenuPol-5, Denmark) in an electrolyte containing perchloric acid and methanol (1:9) at temperatures below

–30 °C and a voltage range of 15 V. A FEI Tecnai F30 (300 kV) and Talos F200X (200 kV) TEM was used to study microstructure.

4.3.5 Electron probe micro-analysis

Electron probe microanalysis (EPMA) is mainly used for non-destructive chemical analysis of bulk samples. It is also known as an electron microprobe, can detect elements from Li to Pu with a detection limit of 100 ppm. The working principle of EPMA is that electron beam bombards the sample to produce electrons and X-rays. Wavelength dispersive X-ray spectroscopy (WDS) has high peak resolution and peak-to-background ratio for chemical analysis. In this study, JEOL JXA-8230 EPMA was used for determining carbon concentration as a function of depth.

4.3.6 X-ray diffraction

The X-ray diffraction (XRD) produces diffraction patterns by the interaction of a monochromatic X-ray beam with electrons in the atoms of a crystal lattice. The working principle of X-ray diffraction is based on Bragg's law given in eq. 4.1.

$$n\lambda = 2d\sin\theta \tag{4.1}$$

where n is the diffraction order, λ is the wavelength of the X-ray source, d is the diffraction interplanar spacing, and θ is the diffraction angle. XRD can be used to identify phases (qualitative/quantitative phase analysis) and lattice parameters in materials. Phase identification is achieved by matching diffraction peaks with a database (PDF-4, ICSD). For a cubic crystal system, the relationship between the lattice parameters and the interplanar spacing is given by eq. 4.2.

$$a = d\sqrt{h^2 + k^2 + l^2} \tag{4.2}$$

Here, a is the lattice parameter, h, k, l are Miller indices. In this study, Bruker D8 Discover with Cu-radiation source (λ = 0.154056 nm) was used with operating voltage at 40 kV and the tube current of 40 mA.

4.3.7 X-ray photoelectron spectroscopy

X-ray photoelectron spectroscopy (XPS) is a surface-sensitive analytical technology used to study the surface composition and chemical state of materials. It can also be combined with argon ion beam etching to perform depth profiling. XPS measures the kinetic energy and number of electrons that escape from the top 1-10 nm of surface. Soft characteristic X-rays interact with surface atoms and excite photoelectrons from different core energy levels of the atoms. The chemical state and content of the elements on the surface of the sample can be obtained by detecting the kinetic energy and quantity of the photoelectrons by the detector. The binding energy of certain core level photoelectrons E_B can then be determined using eq. 4.3.

$$E_B = h\nu - E_K - \varphi \tag{4.3}$$

where E_K is the kinetic energy of photoelectrons, hv is the energy of incident photons, and φ is the work function.

In this study, PHI VersaProbe III Scanning XPS microprobe (ULVAC-PHI) equipped with a monochromatic Al Kα X-ray source (h_γ = 1486.6 eV) was used. The X-ray beam size was 100 µm and take-off angle was 45°. The obtained spectra were analysed using Multipak software.

4.3.8 Hydrogen measurement

Thermal desorption analysis (TDA), often called thermal desorption spectroscopy (TDS), is a technique used to quantify and characterize trapped gases or volatiles in solids. In TDS, a sample is gradually heated in a controlled environment, causing adsorbed or absorbed species to desorb from the material's surface. As the temperature increases, these substances are released and are detected by a mass spectrometer (MS) or thermal conductivity detector (TCD). TDMS typically employs hot extraction, yielding desorption spectra that gives the amount of desorbed species as a function of temperature. It can be used to analyze hydrogen trapping behavior and desorption kinetics in metals. From a TDS, several key pieces of information can be extracted: desorption peaks, activation energy, and hydrogen concentration. TCD utilizes inert gas fusion/carrier gas hot extraction to directly detect hydrogen content based on differences in thermal conductivity.

In this study, the total hydrogen content was measured using a Bruker G8 GALILEO ONH analyzer based on inert gas fusion technology. Diffusible hydrogen measurement was carried out using Bruker G8 GALILEO ONH Analyzer and external infrared furnace IR07 setup with a heating rate of 0.5 °C/s. Figure 4.5 shows the hydrogen content obtained using inert gas fusion and carrier gas hot extraction. Hydrogen content was measured using specimens a) in the disc form with a diameter of 10 mm and a thick of 2 mm, b) from the gauge length of tensile specimens.

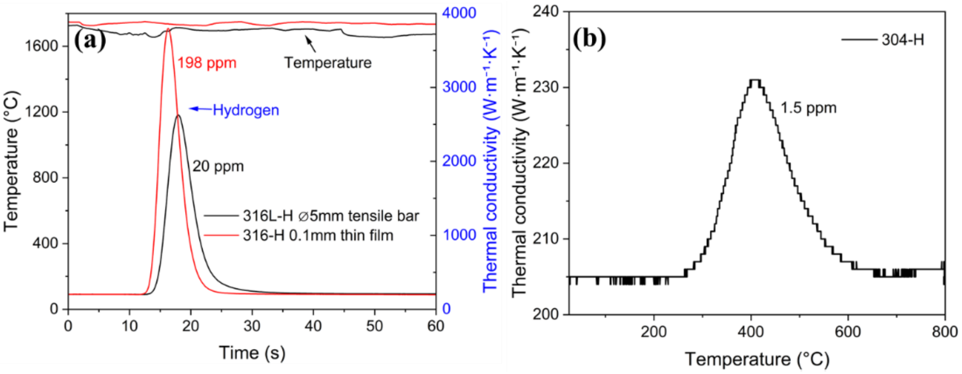

Figure 4.5 Hydrogen content obtained based on (a) inert gas fusion and (b) carrier gas hot extraction.

4.4 Hydrogen permeation test

Hydrogen permeation testing is widely used for characterizing the diffusion behavior of hydrogen in metallic materials, providing critical parameters such as the hydrogen diffusion coefficient and permeability. These parameters are essential for assessing material reliability and safety in hydrogen-containing environments, and provide an important basis for material selection and structural design to ensure long-term service performance.

In this study, hydrogen permeation was assessed using a Devanathan-Stahurski (D-S) cell [102]. The test sample is a 0.1 mm thick membrane with an exposed area of 1 cm^2. Before the experiment, a thin nickel film was plated on the anode side to catalyze hydrogen ionization and prevent the substrate from dissolving. The anode chamber was filled with 0.2 M NaOH solution, while the cathode chamber contained 3wt% NaCl+ 0.3wt% NH_4SCN solution. A Hg/HgO electrode was used as the reference electrode (RE), and two platinum electrodes were used as the counter electrode (CE). A schematic of the setup is shown in Figure 4.6. First, a constant potential of 200 mV (vs Hg/HgO) was applied to the anode side. When the background current density value measured on the anode side drops below 0.2 $\mu A/cm^2$, a constant current was applied to introduce hydrogen. The hydrogen atoms generated on the cathode side diffused through the sample and finally escaped on anode side. The escaped hydrogen atoms were then ionized by the constant potential of the anode to obtain transient curve.

The effective diffusion coefficient D_{eff} can be calculated from the elapsed time (t_{lag}), as shown in eq. 4.4.

$$D_{eff} = \frac{L^2}{6t_{lag}} \tag{4.4}$$

Here, t_{lag} is defined as the time at which the current ratio $i_t/i_{ss} = 0.63$, i(t) is the hydrogen current at time t, and i_{ss} is the steady-state hydrogen current. Figure 4.6 shows the schematic D-S cell used for hydrogen permeation testing and the obtained hydrogen permeation curves.

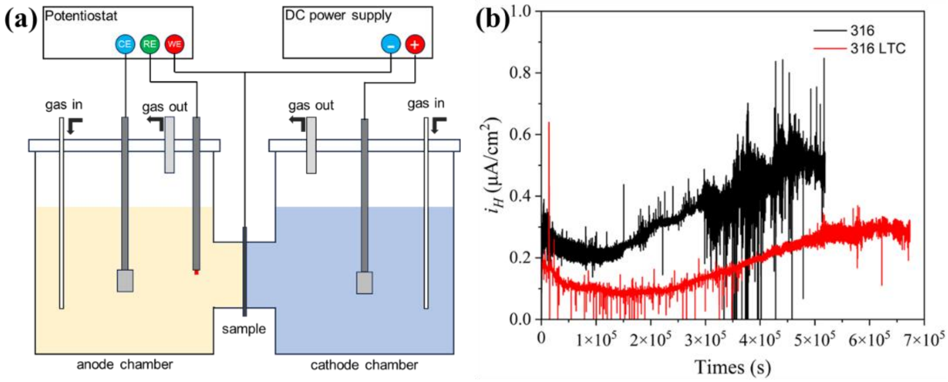

Figure 4.6 (a) Schematic of Devanathan-Stahurski cell and (b) electrochemical hydrogen permeation curves.

4.5 Mechanical testing

4.5.1 Hardness measurement

Hardness reflects material resistance to local plastic deformation. It is generally correlated with strength, toughness and wear resistance. Materials with high hardness typically exhibit high strength and wear resistance but may also become brittle. In contrast, low-hardness materials tend to be more ductile and capable of sustaining large deformations without fracture. Various methods exist for measuring hardness, and the appropriate choice depends on the material type and the required accuracy. In this study, the micro-indentation Vickers hardness was applied due to the thin carburized layer (20 - 30 μm).

Vickers hardness uses a square-based pyramidal diamond indenter with a face angle of 136°. According to ASTM E384-22 standard [103], the hardness is calculated using eq. 4.5.

$$HV = 1854.4 \times \frac{F}{d_V^2} \tag{4.5}$$

Here F is the applied load (gf) and d_V is the mean diagonal length of Vickers indentation (μm). To minimize experimental error, the microhardness was measured on the polished cross-section using a DuraScan 70 G5 micro-Vickers hardness tester under a load of 10-20 gf. The distance between the indentations (> $3d_V$) follows the ASTM E92-17 standard to avoid overlapping deformation fields. The size of the indentation was measured using SEM, and each reported hardness value represents the average of five measurements.

4.5.2 Slow strain rate tensile testing

The slow strain rate tensile (SSRT) test was conducted in accordance with ASTM E8M-22 [104]. Limited by the geometry of the received steels, two types of tensile specimens were machined, as shown in Figure 4.7. The cylindrical specimens for 304 and 316L had a diameter of 5 mm, and the dog bone-shaped specimens for 316 and 3015 had thicknesses of 0.1 mm and 0.8 mm, respectively. The tensile tests were performed at ambient temperature using universal testing machines (Instron 5500R, USA and Kammrath & Weiss, Germany) under constant strain rates of 1×10^{-3} s^{-1}, 1×10^{-4} s^{-1} and 5×10^{-5} s^{-1}.

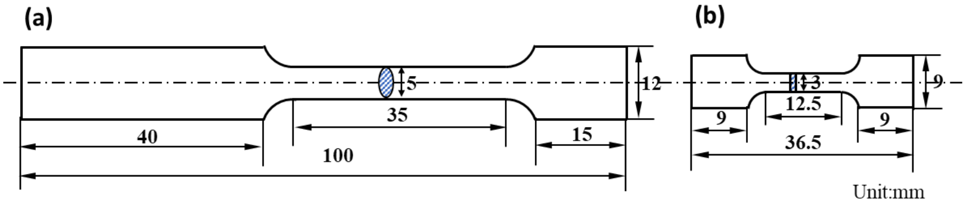

Figure 4.7 Geometries of tensile specimens (a) cylindrical (b) dog-bone shape.

For hydrogen charged samples, the tensile test was performed immediately after charging was completed. The susceptibility to hydrogen embrittlement was evaluated using hydrogen embrittlement index δ_L, or φ_L, namely relative plasticity loss, are defined in eq. 4.6 and 4.7.

$$\delta_L = \frac{\delta_0 - \delta_H}{\delta_0} \times 100\% \tag{4.6}$$

$$\varphi_L = \frac{\varphi_0 - \varphi_H}{\varphi_0} \times 100\% \tag{4.7}$$

where δ_0 and δ_H are total elongation of uncharged and H-charged specimens, respectively. φ_0 and φ_H are area reduction of uncharged and H-charged specimens, respectively. In general, high δ_L or φ_L indicates high plasticity loss and high susceptibility to hydrogen embrittlement.

5 Summary of results

This study systematically investigates HE in a few selected austenitic stainless steels. Hydrogen was introduced into the samples by cathodic hydrogen charging, a technique widely used in experimental research. It is well established that charging parameters strongly influence hydrogen fugacity and uptake, surface condition, and even near-surface microstructure, thus affecting mechanical properties [20,21,48,49]. **Paper I** focused on the influence of charging parameters on surface morphology and hydrogen uptake in ASS with different surface roughness. This paper provided a reference for subsequent sample machining and hydrogen charging parameter selection. **Paper II** investigated the microstructure evolution during cathodic hydrogen charging in samples with different initial microstructures (cold worked and solution annealed) subjected LTC treatment. This work demonstrated that microstructure and charging parameters were critical factors governing hydrogen-induced cracking. Building upon the studies on hydrogen charging parameters, microstructure, and hydrogen uptake in **Papers I & II**, **Paper III** focused on the impact of hydrogen uptake on mechanical properties. This paper investigated the effects of hydrogen uptake on the deformation behavior and HE of 304 and 316L after LTC treatment. To address conditions of practical relevance, **Paper IV** investigated the effect of LTC treatment on susceptibility to HE in cold-worked 304, a material state widely used in industrial applications. This work bridges fundamental mechanisms and engineering practice by evaluating hydrogen effects under realistic processing conditions. The comprehensive results of **Paper I-IV** show that hydrogen and carbon have limited diffusion depths in bulk samples. To maximize the diffusion depth relative to the sample thickness, 316 thin film specimens were used, with carbon introduced by LTC and hydrogen by cathodic hydrogen charging in **Paper V.** The effects of hydrogen and carbon on deformation behavior and mechanical properties were compared, further revealing the hydrogen-carbon-austenite interaction, and confirming the dominant role of concentration gradient in controlling HE in ASS. **Paper VI** shifted to precipitation hardened NCF 3015 austenitic superalloy to further investigate the effects of hydrogen, carbon, and carbides on deformation behavior and mechanical properties. In-situ EBSD-SEM was employed to track direct experimental evidence of the interaction between hydrogen and microstructure during the plastic deformation of H-charged 3015. Essentially, this doctoral thesis addressed four research questions (RQs).

5.1 Microstructural evolution and hydrogen uptake induced by cathodic hydrogen charging

The effects of different charging parameters were systematically examined, including electrolyte type (0.2M H_2SO_4, 3wt% NaCl, and 0.2M NaOH), current density (0.1-30 mA/cm^2), and charging duration (1-24 h). The resulting microstructural evolution and hydrogen uptake were characterized to elucidate the relationships between charging conditions, surface condition, and hydrogen uptake. In addition, initial microstructure itself plays a critical role in hydrogen diffusion and uptake. Surface treatments can effectively modify the near-surface microstructure and thus alter hydrogen absorption and transport behavior. Accordingly, the influence of surface microstructure on hydrogen uptake and microstructural evolution was further investigated by employing surface grinding and LTC treatments. Through these controlled modifications, the interplay between surface microstructure, hydrogen diffusion, and hydrogen uptake was systematically assessed. These results provide guidelines for selecting appropriate sample surfaces and hydrogen charging parameters.

5.1.1 Effects of current density, electrolyte type, and charging time

Current density strongly influences surface morphology and hydrogen uptake during cathodic hydrogen charging in 0.2M H_2SO_4. As shown in Figure 5.1a, at low current density (0.3 mA/cm^2), the surface remained intact, although dense slip bands are observed, indicating hydrogen-assisted plastic deformation. As the current density increased, cracks and localized corrosion developed (Figure 5.1b & c). These cracks preferentially initiated along slip bands, typically appearing as straight cracks, and at grain boundaries, highlighting the role of deformation-induced microstructural features in hydrogen-assisted damage. Quantitative crack density analysis (Table 5.1) shows a strong dependence on current density. No cracking was observed at 0.3 mA/cm², whereas both crack density metrics nearly doubled as the current density increased from 3 mA/cm² to 30 mA/cm². The significantly increased crack density correlated closely with hydrogen content, which rose from 2.08 ppm to 17.50 ppm, a 7.4-fold increase. High current densities lead to high hydrogen fugacity, thereby enhancing hydrogen absorption and promoting internal stress accumulation. The resulting surface cracking further facilitates hydrogen ingress. Hydrogen uptake and surface damage are positively correlated.

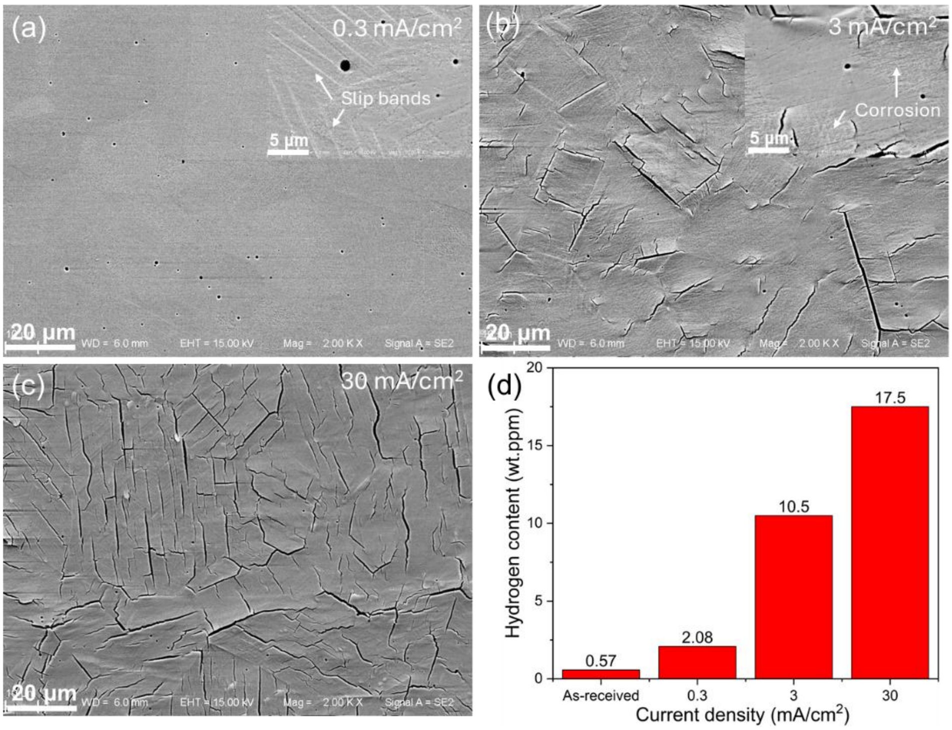

Figure 5.1 Surface morphologies corresponding to hydrogen charging at different current densities in 0.2M H_2SO_4: (a) 0.3 mA/cm^2, (b) 3 mA/cm^2, (c) 30 mA/cm^2. (d) Total H content versus current densities of solution-annealed 316L.

Table 5.1 Cracks density in solution-annealed 316L during cathodic hydrogen charging in 0.2 M H_2SO_4

Current density (mA/cm^2)	0.3	3	30
ρ_l (10^4 μm mm^{-2}) ^{a}	-	1.1	1.9
ρ_{nr} (10^5 mm^{-2}) ^{b}	-	2.7	5.3

a: ρ_l is defined as the length of cracks per unit area

b: ρ_{nr} is defined as the number of cracks per unit area

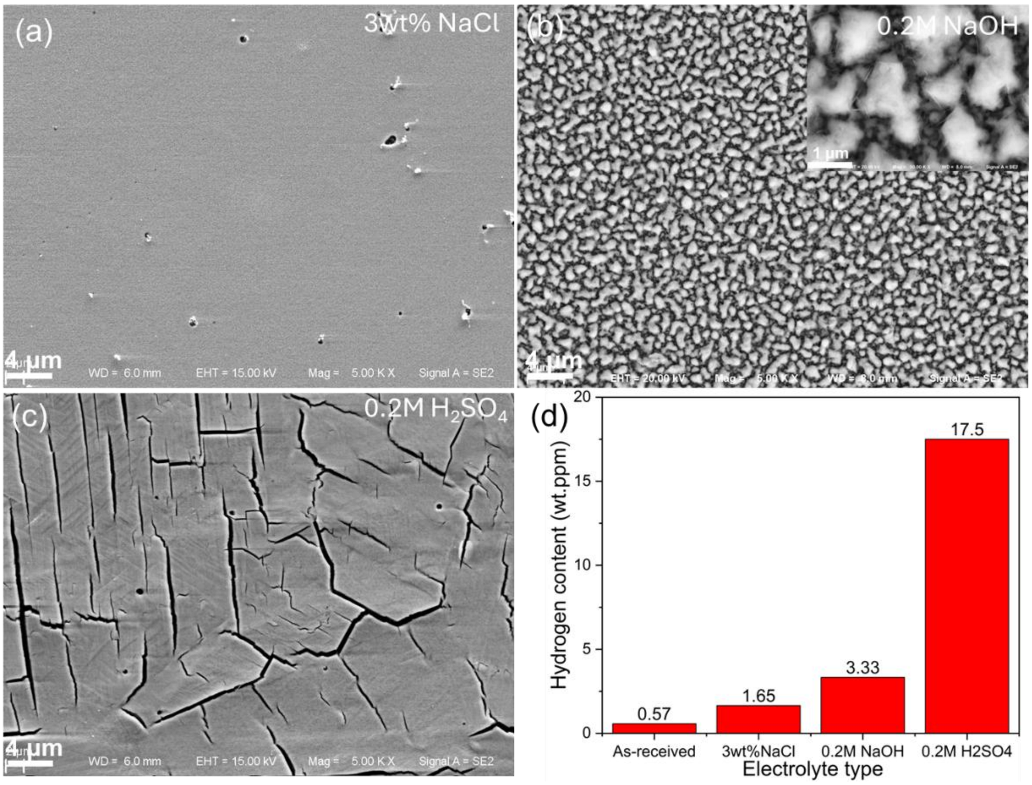

Figure 5.2 Surface morphologies corresponding to hydrogen charging at different electrolytes: (a) 3wt% NaCl, (b) 0.2M NaOH, (c) 0.2M H_2SO_4. (d) Total H content versus electrolyte type of 316L during cathodic hydrogen charging at current density of 30 mA/cm^2.

Electrolyte type is another dominant factor controlling surface morphology and hydrogen uptake during electrochemical hydrogen charging. At the same current density of 30 mA/cm^2, as shown in Figure 5.2a, hydrogen charging in 3 wt% NaCl resulted in minimal surface modification, with no surface damage or corrosion features. Hydrogen charging in 0.2 M NaOH led to surface deposition (Figure 5.2b), while charging in 0.2 M H_2SO_4 produced severe surface cracking (Figure 5.2c). XPS chemical analysis identified the surface deposits as hydrocerussite ($2PbCO_3 \cdot Pb(OH)_2$) when using 0.2 M NaOH. Detailed characterization and discussion were provided in **Paper I**. Correspondingly, hydrogen content measurements (Figure 5.2d) show that specimens charged in NaCl exhibit the lowest hydrogen uptake (~ 1.65 ppm), followed by NaOH, whereas charging in H_2SO_4 results in the highest hydrogen content. These differences can be attributed to variations in hydrogen fugacity and surface condition associated with electrolyte pH and chemistry. Acidic solutions with high H^+ activity promote the highest hydrogen fugacity and, when combined with extensive surface cracking, lead to the greatest hydrogen uptake in H_2SO_4. Although NaCl is neutral (pH ≈ 7), hydrogen generation is limited to the reduction of H_2O. In contrast, alkaline NaOH solutions provide hydrogen from both H_2O and OH^- reduction, resulting in higher hydrogen uptake than in NaCl. In addition, surface cracking further enhances hydrogen ingress by increasing the effective surface area and providing additional hydrogen entry pathways. Overall, these observations highlight the critical role of electrolyte chemistry in governing hydrogen uptake through its combined effects on hydrogen fugacity, surface reactions, and surface integrity.

Hydrogen charging time also has a pronounced effect on microstructural evolution. As shown in Figure 5.3, increasing charging duration in 0.2 M H_2SO_4 led to the progressive development of surface cracking. These cracks were primarily associated with hydrogen-assisted martensitic phase transformation in metastable 304 stainless steel, as discussed in detail in **Paper II**.

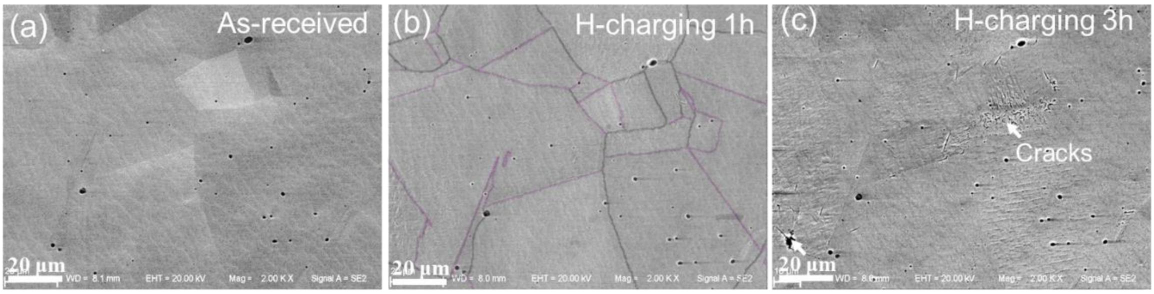

Figure 5.3 Microstructure corresponding to different hydrogen charging time: (a) as-received, (b) H-charging for 1h, (c) H-charging for 3h. Solution-annealed 304 stainless steel was cathodic hydrogen charged at 1 mA/cm² in 0.2 M H_2SO_4.

5.1.2 Effects of surface roughness and low-temperature carburizing

Surface finish is an important but often overlooked factor influencing hydrogen absorption in industrial components. As shown in Figure 5.4, samples with different surface roughness exhibit markedly different surface morphologies and hydrogen contents after cathodic hydrogen charging. Surfaces prepared by grinding with coarse grits remain intact (Figure 5.4a & b) after hydrogen charging, whereas specimens polished to a fine finish exhibit pronounced surface cracking (Figure 5.4c) accompanied by a significant increase in hydrogen content (Figure 5.4d). These observations indicate that increased surface roughness suppresses hydrogen-induced cracking and reduces hydrogen uptake. In-situ hydrogen charging combined with optical microscopy observations in **Paper I** further revealed that rough surfaces promoted hydrogen recombination at the surface, resulting in more frequent hydrogen bubble formation and lower net hydrogen absorption. In contrast, smooth surfaces exhibited fewer hydrogen bubbles, suggesting inhibited hydrogen recombination and enhanced hydrogen ingress. Overall, these findings highlight the critical role of surface roughness in regulating hydrogen absorption through its influence on surface reactions and damage evolution.

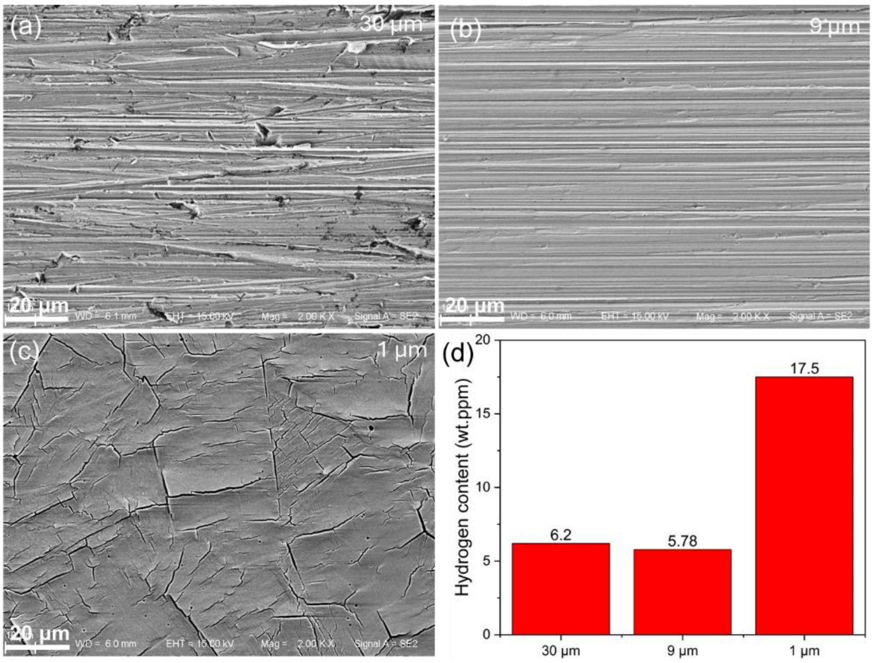

Figure 5.4 Surface morphologies corresponding to hydrogen charging with prior grinding using different grit size: (a) 30 µm, (b) 9 µm, (c) 1 µm. (d) Total H content versus grit size of solution-annealed 316L during cathodic hydrogen charging at 30 mA/cm^2 in 0.2 M H_2SO_4.

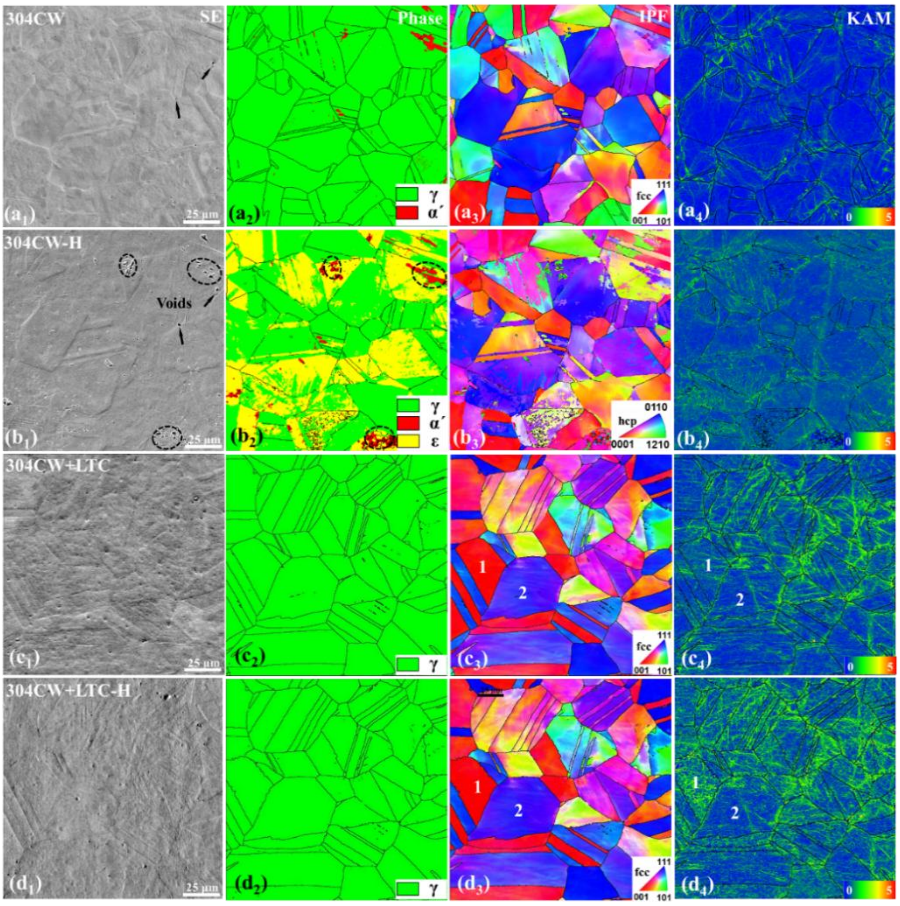

Figure 5.5 The effect of LTC and hydrogen uptake on the microstructure of cold-worked 304. The sample was hydrogen charged at a current density of 1mA/cm^2 for 1 h in 0.2M H_2SO_4.

LTC treatment on ASS leads to the formation of a supersaturated interstitial carbon solid solution in surface region, known as expanded austenite, which greatly improves surface hardness and austenite stability. As shown in Figure 5.5, distinct differences in microstructural evolution were observed between as-received and LTC-treated samples before and after hydrogen uptake. Cold-worked 304 exhibited a small amount of martensite and predominant austenite (Figure 5.5a$_2$). Following hydrogen uptake, the formation of surface microvoids (Figure 5.5b$_1$) and hydrogen-assisted martensitic transformation (Figure 5.5b$_2$) was observed, accompanied by a pronounced increase in local strain (Figure 5.5b$_4$). In contrast, LTC-treated cold-worked 304 exhibits a more stable austenitic microstructure (Figure 5.5c$_2$), despite an overall increase in local strain (Figure 5.5c$_4$) induced by carburization. Notably, the austenitic phase in the LTC-treated material remains stable after hydrogen uptake (Figure 5.5d$_2$), indicating that carburization effectively suppresses hydrogen-induced martensitic transformation. Kernel average misorientation (KAM) analysis further reveals that hydrogen uptake increases local strain in an orientation-dependent manner, highlighting the combined influence of hydrogen and crystallographic orientation on deformation behavior.

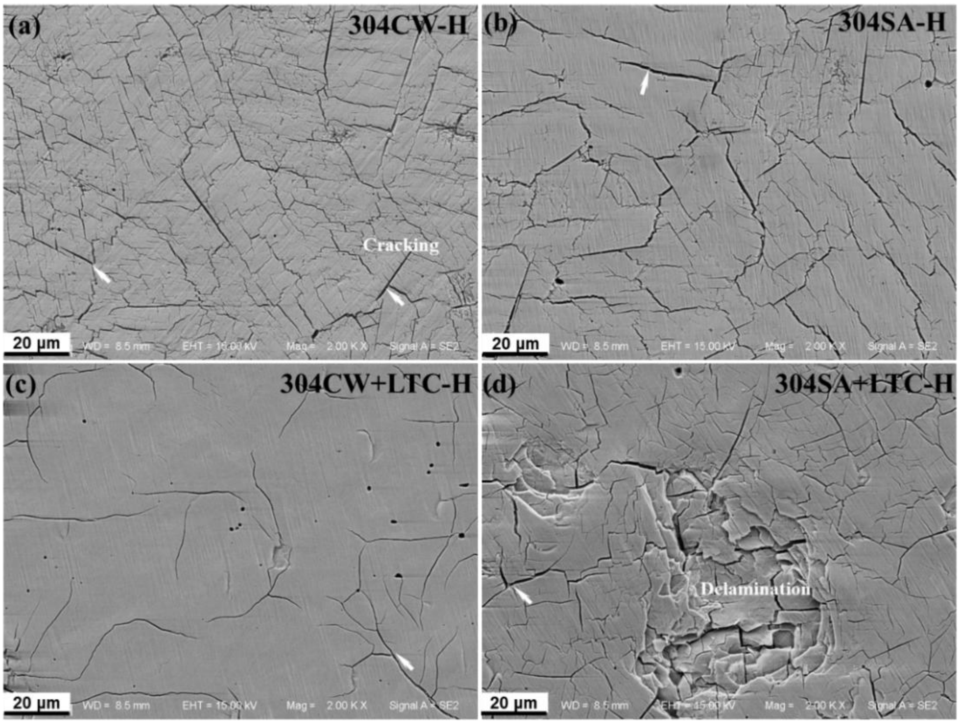

Figure 5.6 SEM images of sample surfaces in different conditions after hydrogen charging (a) 304 CW-H, (b) 304 SA-H, (c) 304 CW+LTC-H and (d) 304SA+LTC-H. All samples hydrogen charging at 30 mA/cm^2 in 0.2 M H_2SO_4 for 24h.

Table 5.2 Density of cracks in 304 with hydrogen charging at 30 mA/cm^2 in 0.2 M H_2SO_4 for 24h

Sample	304 CW-H	304 SA-H	304 CW+LTC-H	304SA+LTC-H
ρ_l (10^4 µm mm^{-2}) [a]	8.8	3.5	0.8	4.2
ρ_{nr} (10^5 mm^{-2}) [b]	2.8	1.1	0.1	1.1

a: ρ_l is defined as the length of cracks per unit area

b: ρ_{nr} is defined as the number of cracks per unit area

The influence of different material conditions, i.e., cold worked and solution annealed, on surface cracking at high current density charging is further illustrated in Figure 5.6. All specimens exhibit hydrogen-induced surface cracking, although pronounced differences in crack morphology and density are observed. The cracks observed on 304 CW-H and 304 SA-H were sharp and straight (Figure 5.6a,b), characteristic of rapid crack initiation and propagation. In contrast, LTC-treated specimens exhibit more tortuous crack paths (Figure 5.6c,d), indicating impeded crack propagation by LTC. Quantitative analysis of crack density was performed using Image-Pro Plus and is summarized in Table 5.2. For cold-worked material, LTC treatment led to a substantial reduction in crack density compared with the untreated condition. However, in the solution-annealed state, LTC treatment resulted in a slightly higher crack density compared with the untreated material. Consistent with this observation, localized delamination and fracture are observed in the LTC-treated solution-annealed specimens. These results indicate that the effect of LTC on hydrogen-induced cracking is strongly dependent on the initial microstructural state, with crack-mitigating behavior in cold-worked material and a more complex, potentially adverse response in the solution-annealed condition.

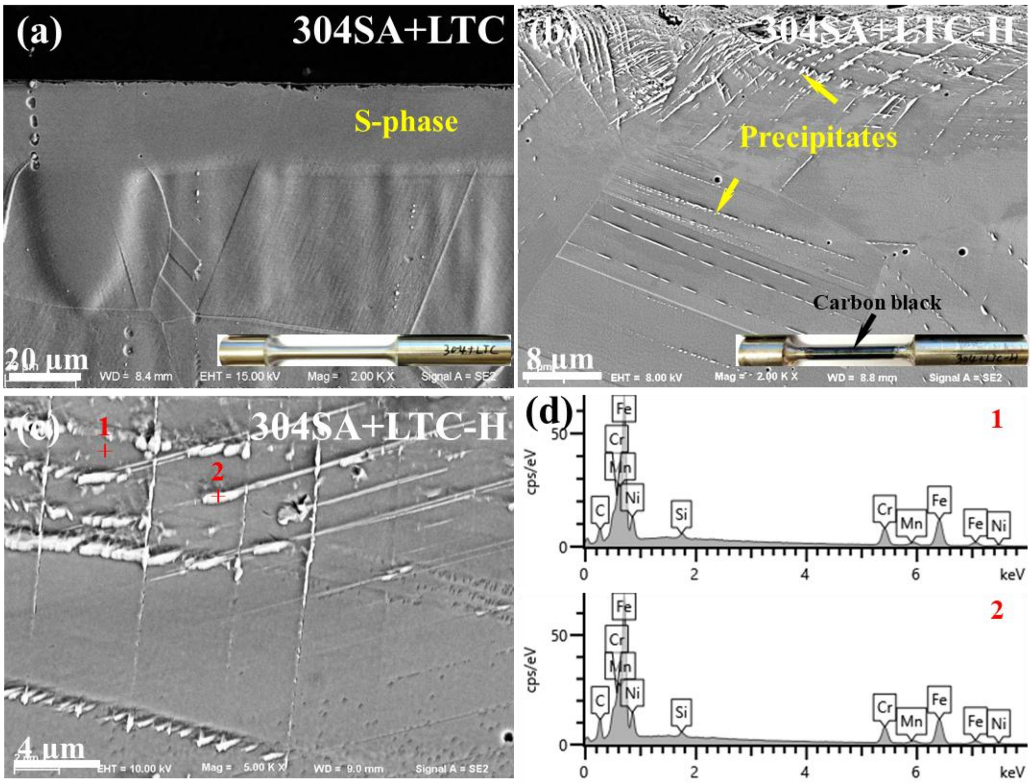

Figure 5.7 Cross-sectional SEM images of (a) 304 SA+LTC, (b,c) 304 SA+LTC-H, (d) EDX analysis of the points in Figure 5.7(c).

To elucidate surface delamination, cross-sectional SEM observations were conducted on 304 SA+LTC specimens before and after hydrogen charging. In the uncharged condition, a well-defined S-phase layer was observed without evident precipitation (Figure 5.7a). In contrast, hydrogen charging led to the formation of a high density of precipitates within the S-phase (Figure 5.7b,c). Elemental point analysis revealed that the precipitates (point 2) had higher carbon intensity compared to the matrix (point 1) (Figure 5.7d). Microcracks are observed in the vicinity of these precipitates, particularly near the surface, resulting in pronounced surface embrittlement. In fact, as observed in the insert of Figure 5.7b, the carbon black on the 304 SA+LTC-H surface forms compared to 304 SA+LTC (Figure 5.7a).

Phase stability is a critical microstructural factor governing hydrogen embrittlement, and numerous studies have shown that martensitic phase transformation increases susceptibility to hydrogen-assisted damage [7-9]. Figure 5.8 compares the XRD patterns of solution-annealed and LTC-treated 304 and 316L before and after hydrogen charging. LTC treatment caused all diffraction peaks of both alloys to shift to lower angles, reflecting lattice expansion due to interstitial carbon incorporation. For 304, hydrogen charging induced a ε-martensite phase transformation, while LTC treatment stabilized austenite even after hydrogen charging (Figure 5.8a). Although 316L exhibited higher intrinsic austenite stability than 304, ε-martensite was still observed after hydrogen charging (Figure 5.8b). However, LTC treatment again effectively suppressed this transformation, confirming its stabilizing effect on austenite. Notably, hydrogen charging led to shifts in diffraction peaks that depend on carbon content. For 304 and 304 LTC, hydrogen charging resulted in diffraction peak shifts to higher angles, indicating lattice contraction (Figure 5.8c). This behavior contrasts with previous reports of hydrogen-expanded austenite, in which hydrogen uptake produces lattice expansion and peak shifts to lower angles [105,106]. In comparison, hydrogen charging shifted the diffraction peaks of 316L-H to lower angles, whereas peaks of 316L LTC-H shifted to higher angles after charging (Figure 5.8d). These contrasting trends indicate that carbon concentration in the expanded austenite strongly influences the lattice response to hydrogen. The decrease in lattice parameters in 304 LTC-H was likely associated with precipitation. Consistent with this interpretation, cross-sectional observations (Figure 5.7b) revealed extensive precipitation in the S-phase after hydrogen charging. In addition, the $\gamma_{(200)}$ peak of 304 LTC-H in the inset of Figure 5.8a showed peak splitting, suggesting the possible presence of hydrogen induced precipitates, likely carbides. However, this requires further confirmation. Given the high carbon concentration (~ 2.5 wt%) in the S-phase of 304 LTC, the system is in a thermodynamically metastable state. According to the temperature-pressure phase diagram of the Fe-C system, Fe_3C and free carbon are thermodynamically stable at temperatures above 300 K under pressures exceeding approximately 10 GPa [107]. Under the combined effects of extremely high hydrogen-induced stress (~ 10^{11} Pa) [106] and elevated temperature (80 °C), carbide precipitation becomes plausible. The appearance of a black powdery residue on the surface of 304 LTC-H further supports carbide precipitation or decarburization.

In addition to stabilizing austenite, LTC treatment significantly affects hydrogen uptake. As shown in Figure 5.9, LTC treatment markedly increased hydrogen uptake in 304, whereas it reduced hydrogen uptake in 316L. The enhanced hydrogen absorption in 304 LTC-H was attributed to precipitates acting as strong hydrogen traps, indicating that excessive carbon supersaturation in the S-phase promoted hydrogen-induced precipitation. These findings highlight the complex interplay between carbon supersaturation, phase stability, lattice response, and hydrogen uptake in LTC-treated ASS.

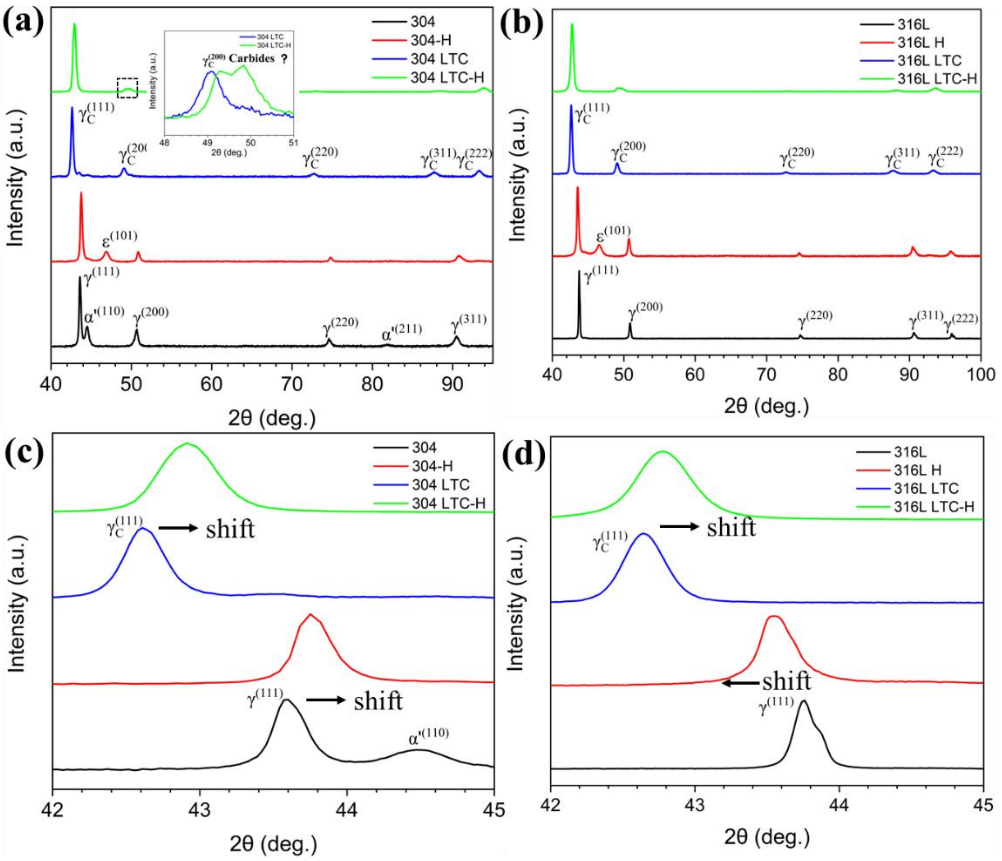

Figure 5.8 XRD patterns of (a,c) solution-annealed 304/304 LTC and (b,d) 316L/316L LTC with and without hydrogen charging. Hydrogen charging at 30 mA/cm^2 in 0.2 M H_2SO_4 for 24h at 80 ℃.

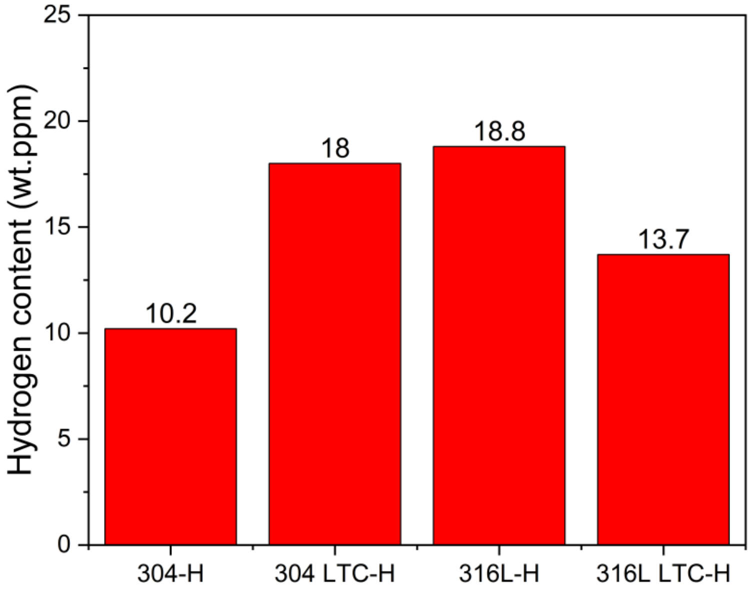

Figure 5.9 Hydrogen content of solution-annealed and LTC-treated samples with hydrogen charging at 30 mA/cm^2 in 0.2 M H_2SO_4 for 24h at 80 ℃.

5.2 Effects of hydrogen uptake on mechanical properties and deformation behavior

Components used in industrial applications typically have varying wall thicknesses, which can lead to different HE behaviors when exposed to hydrogen environments. Under the same hydrogen charging conditions, thicker specimens have a smaller hydrogen diffusion depth relative to the entire specimen thickness, potentially resulting in lower HE susceptibility. Conversely, thinner specimens have a larger hydrogen diffusion depth relative to the entire specimen thickness, potentially impacting mechanical properties significantly. Here, two main factors need to be considered: nominal hydrogen content and stress state. Nominal hydrogen content, the hydrogen content per unit mass or volume, increases significantly as the specimen thickness decreases. Regarding stress state, as illustrated in Figure 3.3, the low hydrogen diffusivity and high solubility of austenite lead to hydrogen expanded austenite formation on the surface. The supersaturated hydrogen in the surface and the low hydrogen in the substrate is expected to create a steep hydrogen concentration gradient. In this case, the hydrogen-expanded austenite on the surface is constrained by the substrate, exhibiting compressive residual stress, while the substrate experiences tensile residual stress. This section will investigate the mechanical properties and deformation behavior of bulk and thin-film tensile bar after hydrogen charging.

5.2.1 Bulk tensile bar - low nominal hydrogen content

The effects of hydrogen uptake on deformation behavior and mechanical properties have been evaluated using cylindrical tensile specimens (5 mm in diameter) subjected to prolonged cathodic charging. All samples were hydrogen charged in 0.2 M H_2SO_4 at a current density of 30 mA/cm^2 at 80 °C for 72 hours. Post-charging inspection confirmed the absence of surface cracking on tensile specimens, ensuring that the measured mechanical properties were not influenced by surface damage. 316L-H typically exhibits higher hydrogen uptake compared to 304-H (7.6 ppm), reaching level on the order of 19.8 ppm. Representative engineering stress-strain curves and corresponding true strain-hardening responses for 304 and 316L, with and without hydrogen, are shown in Figure 5.10. In 304, hydrogen uptake led to a reduction in flow stress and strain-hardening rate, indicative of hydrogen-induced softening (Figure 5.10a,b). This behavior is commonly attributed to hydrogen-assisted surface cracking during deformation, which effectively reduces the load-bearing cross-section area and lowers the true stress. In contrast, 316L-H primarily reduces ductility while having little effect on strength (Figure 5.10c), demonstrating its superior resistance to HE in terms of strength retention. Consistently, the strain-hardening curves of 316L and 316L-H nearly overlap prior to the onset of localized deformation (Figure 5.10d), indicating a negligible influence of hydrogen on its strain-hardening behavior. Despite this strength retention, the elongation loss, expressed as the hydrogen embrittlement index, was higher in 316L than in 304. This trend might be attributed to the finer grain size of 316L (~ 40 μm) compared with 304 (~ 60 μm). Grain boundaries act as effective hydrogen trapping sites and fast diffusion pathways, which can increase hydrogen uptake and exacerbate hydrogen-assisted damage [89].

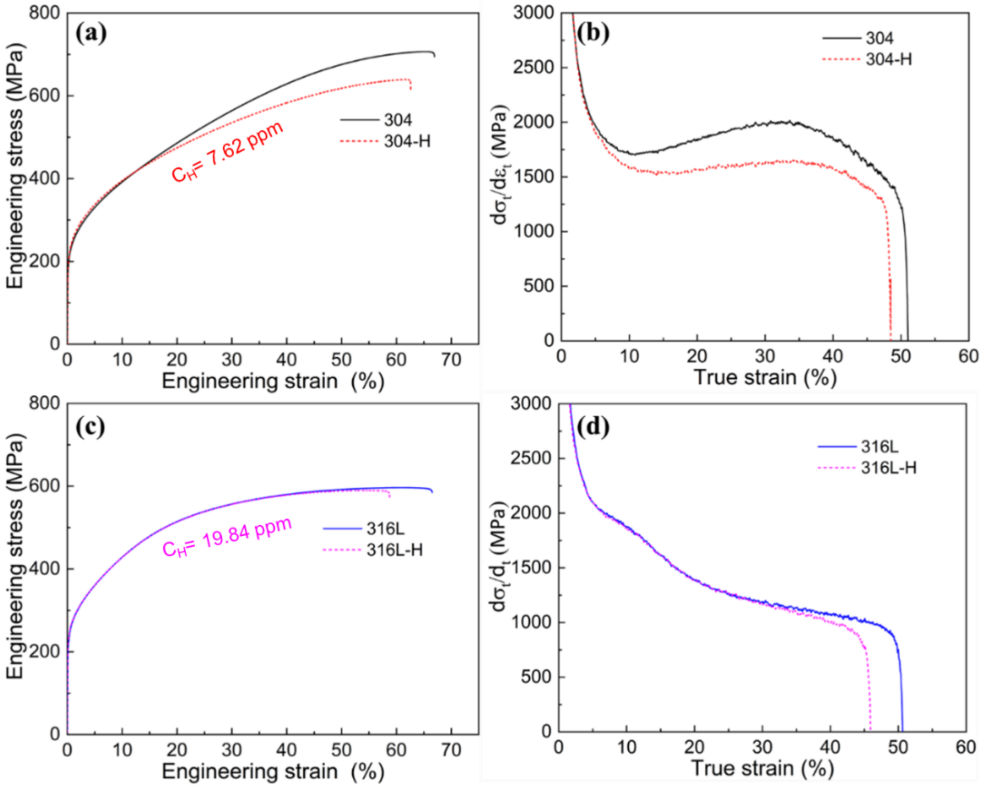

Figure 5.10 Tensile engineering stress-strain and corresponding strain-hardening curves of (a,b) solution-annealed 304 and (c,d) 316L with and without hydrogen charging.

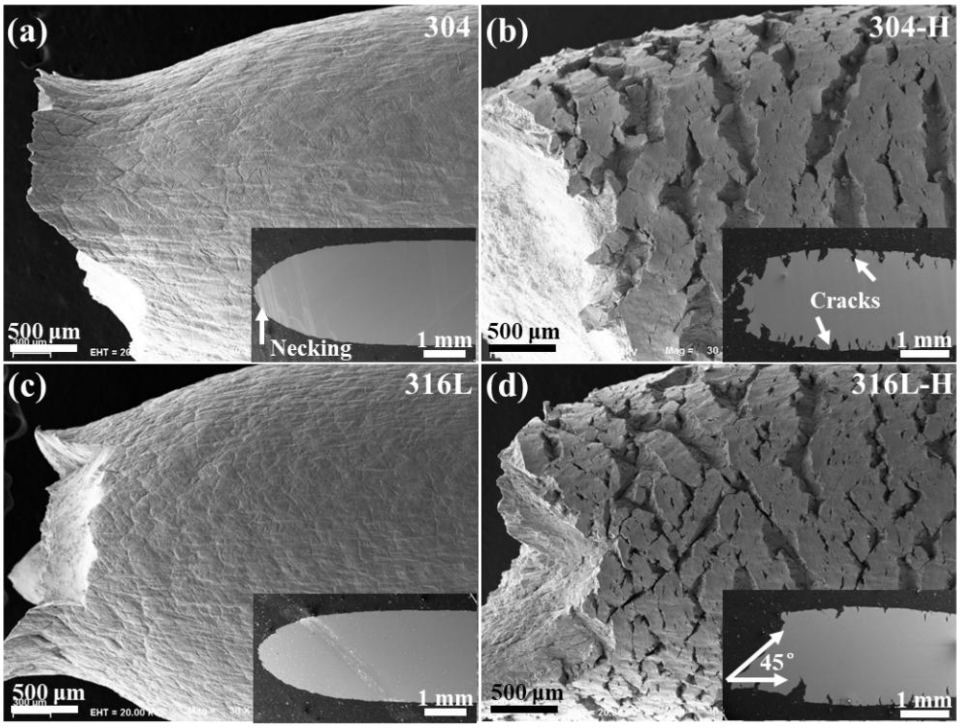

Figure 5.11 Surface of SSRT samples under different conditions after fracture. (a) 304, (b) 304-H, (c) 304 LTC, (d) 304 LTC-H. The inserts show a cross section of the SSRT sample parallel to the loading direction.

Post-test surface morphologies after slow strain rate tensile testing (SSRT) further support these observations. Both 304 and 316L exhibited pronounced necking, with most of the surface remaining intact (Figure 5.11a,c), consistent with ductile fracture. In contrast, H-charged specimens displayed reduced necking accompanied by extensive cracking of peripheral surface, with crack depths reaching several hundred micrometers (Figure 5.11b,d). Notably, hydrogen-assisted cracks in 316L-H were shorter and shallower than those in 304, accounting for the relatively minor effect of hydrogen on the strength of 316L compared with the more pronounced strength degradation observed in 304.

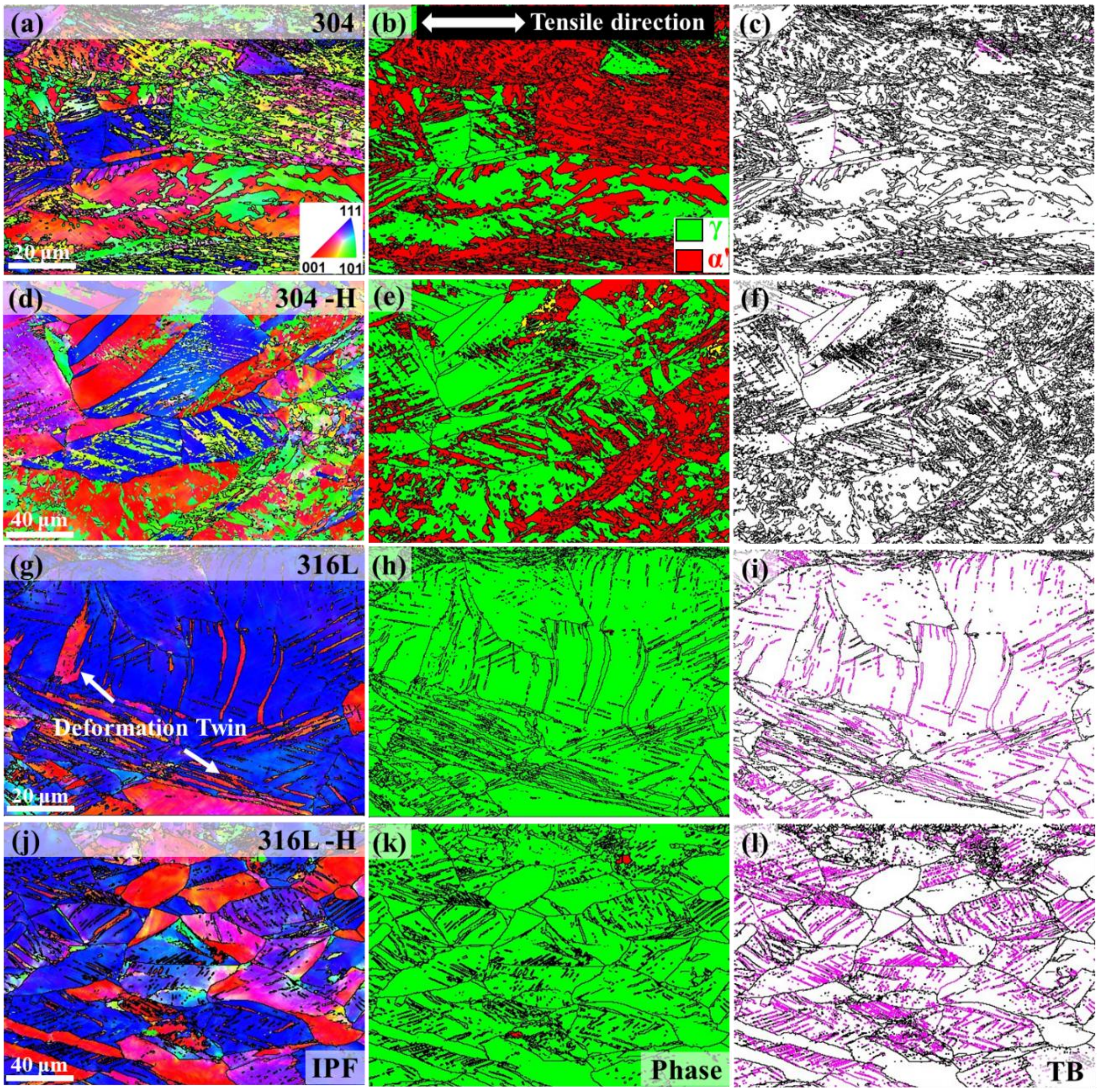

Figure 5.12 EBSD results from the longitudinal cross section of the solution-annealed 304 (a-c), 304-H (d-f), solution-annealed 316L (g-i) and 316L-H (j-l) after tensile testing.

The SSRT specimens were sectioned longitudinally along the tensile direction, and the cross sections close to the fracture surface were examined by post-test EBSD to gain further insight into hydrogen-induced microstructural evolution. As shown in Figure 5.12, distinct differences were observed in the deformed microstructures of 304 and 316L with and without hydrogen charging. In 304, the uncharged condition exhibited a higher martensite fraction than the H-charged condition, with martensitic transformation preferentially occurring in {101}-oriented grains (Figure 5.12b). The reduced martensite content (Figure 5.12e) in 304-H was partly attributable to the lower accumulated plastic strain prior to fracture. Owing to the high near-surface hydrogen concentration, 304-H was more prone to premature failure, which limited plastic deformation. This behavior was consistent with the observed reductions in strain-hardening rate and elongation. In contrast, hydrogen charging had a relatively minor effect on the phase constitution of 316L (Figure 5.12h,k). However, an increased density of deformation twins was evident after hydrogen charging (Figure 5.12i,l). This observation was consistent with previous reports indicating that hydrogen lowered the stacking fault energy, thereby promoting deformation twinning [108–111].

5.2.2 Thin tensile specimen - high nominal hydrogen content

316 thin tensile specimen (~ 0.1 mm) was subjected to hydrogen charging in 3 wt% NaCl at a current density of 3 mA/cm^2 for 1 day and 3 days to investigate the effect of hydrogen on deformation behavior and mechanical properties. The bulk hydrogen content of 316 after 1 day (316 H-1d) and 3 days (316 H-3d) of hydrogen charging was 74.29 ppm and 198.23 ppm, respectively. As shown in Figure 5.13a, hydrogen uptake markedly increased flow stress, with the magnitude of strengthening scaling with hydrogen content. This behavior was attributed to the solid-solution strengthening effect of hydrogen. While hydrogen uptake reduced ductility, the extent of plasticity loss decreased at higher hydrogen contents. This means that increasing the hydrogen charging time may reduce stress-induced premature failure as a result of lowered hydrogen concentration gradients. Strain-hardening curves indicate that hydrogen has a negligible influence on the work-hardening behavior of these thin film specimens.

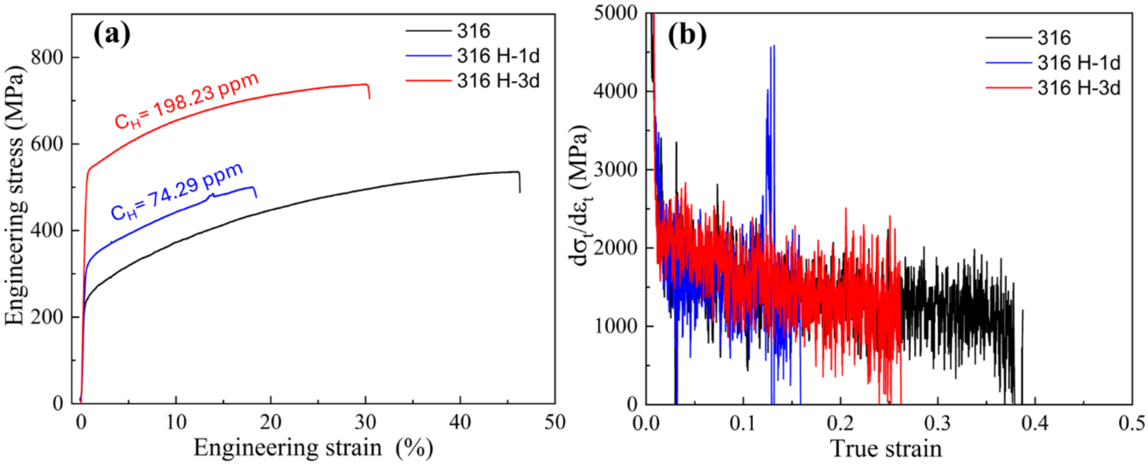

Figure 5.13 (a) Engineering stress-strain and (b) work-hardening rate of thin foil 316 and 316 H specimens.

Fracture surface analyses provide further insight into the underlying deformation mechanisms (Figure 5.14). Solution annealed 316 exhibited pronounced necking, shear lips at the edges, and central dimples, consistent with ductile fracture (Figure 5.14a,a$_1$). For 316 H-1d, the fracture surface was relatively flat, with extensive surface cracking and few central dimples. High-magnification images revealed cleavage features at the edges, indicative of brittle fracture and consistent with the observed loss of elongation (Figure 5.14b,b1). In contrast, 316 H-3d showed quasi-cleavage fracture with some shallow dimples and no surface cracks (Figure 5.14c,c1). The transition from brittle cleavage in 316 H-1d to quasi-cleavage in 316 H-3d suggests that prolonged hydrogen charging reduces hydrogen concentration gradients, thereby mitigating hydrogen-assisted embrittlement. These results demonstrate that hydrogen content and distribution strongly influence both the strength and fracture mode of thin-film ASS.

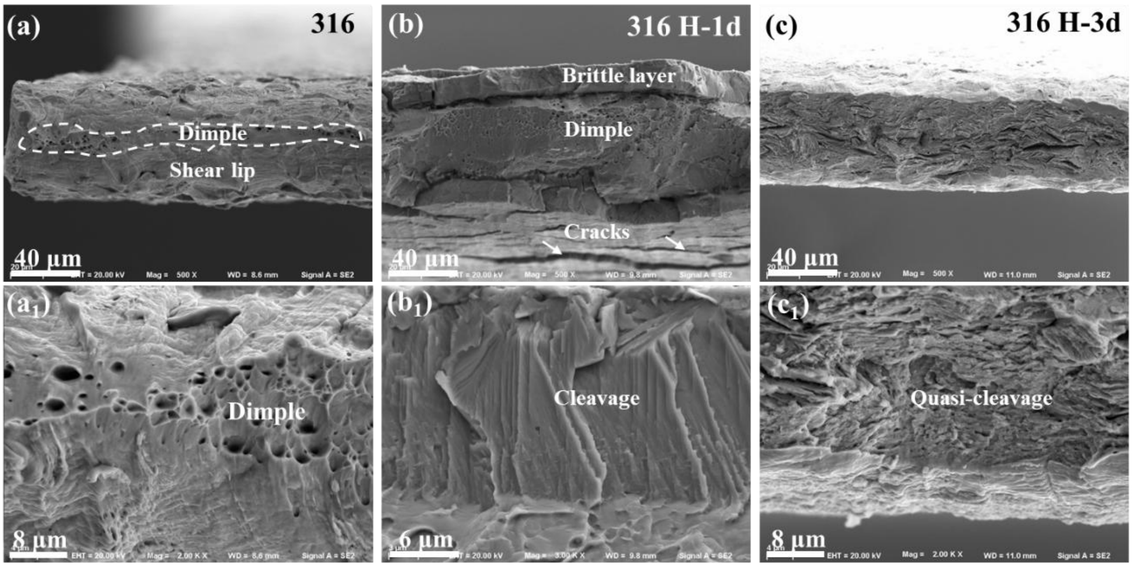

Figure 5.14 Fractography of thin samples in different conditions. (a,a$_1$) 316, (b,b$_1$) 316 H-1d, (c,c$_1$) 316 H-3d.

5.3 Effects of carbon on mechanical properties and deformation behavior

Low-temperature carburizing and cathodic hydrogen charging share a common feature: interstitial atoms diffuse from the surface into the interior driven by a concentration gradient. In this section, the effects of LTC on deformation behavior, microstructural evolution, and mechanical properties are considered. Similarly, LTC affects the mechanical properties and deformation behavior of samples with different thicknesses. This is because carbon forms supersaturated carbon expanded austenite on the steel surface, while the carbon content in the substrate is relatively low, leading to changes in concentration gradient and stress state. This section discussed the effects of LTC treatment on bulk and thin tensile samples.

5.3.1 Bulk tensile bar

The expanded austenite obtained by LTC treatment of solution-annealed 304 and 316L bulk tensile bar with a diameter of 5 mm is approximately 22 μm thick. Figure 5.15 illustrates the influence of LTC on the engineering stress-strain and work-hardening response of 304 and 316L bulk tensile bars. In both alloys, the effect of LTC on yield or tensile strength was relatively small (Figure 5.15a), owing to the shallow carburized layer (~ 22 μm) relative to the specimen diameter. The strain hardening response shows that LTC affects elongation and strain hardening rate (Fig. 5.15b). For solution-annealed 304, high plasticity is achieved through martensitic transformation-induced plasticity (TRIP), while for solution-annealed 316L, high plasticity is achieved through deformation twinning-induced plasticity (TWIP). In solution-annealed 304, LTC slightly enhanced strain hardening rate during early plastic deformation due to carbon solid solution strengthening. The reduced work hardening rate in the later stages of deformation is related to the delayed martensitic transformation. Similarly, LTC treatment increases slightly the early strain hardening rate in solution-annealed 316L due to carbon solid solution strengthening. A detailed discussion was provided in **paper III**.

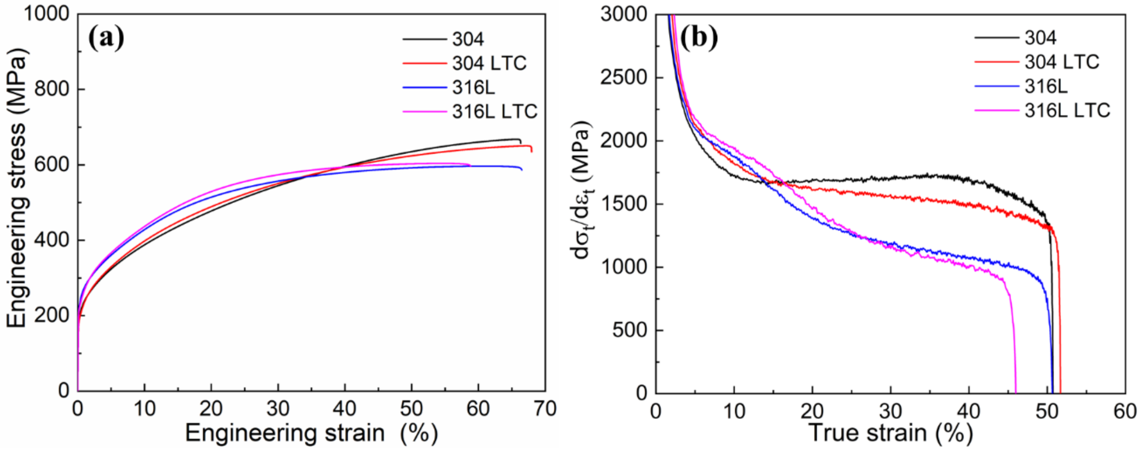

Figure 5.15 (a) Engineering stress-strain and (b) strain hardening curves of solution-annealed and LTC-treated 304 and 316L.

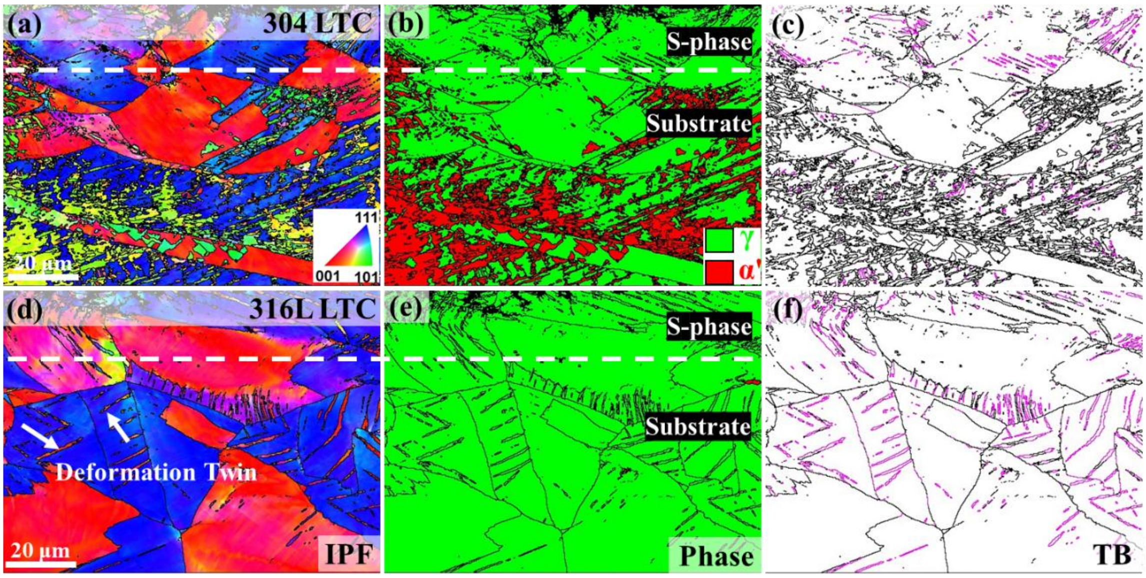

Figure 5.16 EBSD results of the 304 LTC (a-c), 316L LTC (d-f) after tensile testing.

The LTC-treated specimen was sectioned longitudinally along the tensile direction after SSRT, and post-test EBSD analysis was conducted in the edge region containing S-phase, providing insight into the microstructural evolution of LTC-treated specimens during deformation. In 304 LTC, IPF map (Figure 5.16a) and phase maps (Figure 5.16b) show that the S-phase consists of stable austenite, while the underlying substrate undergoes martensitic transformation. This indicates that the S-phase effectively stabilizes austenite and suppresses martensitic transformation. Limited deformation twinning was observed within the S-phase (Figure 5.16c). Similarly, 316L LTC retained a predominantly austenitic microstructure (Figure 5.16d,e) with a small fraction of fine deformation twins (Figure 5.16f), suggesting that LTC treatment enhanced austenite stability and inhibits twinning in the carburized layer relative to the substrate.

5.3.2 Thin tensile specimen

Solution-annealed 316 thin tensile specimen (0.1 mm) were subjected to low-temperature carburizing treatment. The engineering stress-strain curves (Figure 5.17a) of the solution-annealed 316 and 316 LTC thin specimens further highlight the influence of carbon on mechanical properties. LTC significantly increased flow stress while reducing overall ductility. Given that the ~ 22 μm carburized layer constituted approximately 44% of the cross section, carbon contributed substantially to solid-solution strengthening. However, a large carbon concentration gradient can lead to stress-induced cracking and premature failure. The strain hardening response (Figure 5.17b) shows that the strain hardening rate of 316 LTC increased compared to that of solution-annealed 316. However, once plastic deformation was activated, strain accumulates rapidly, resulting in premature failure.

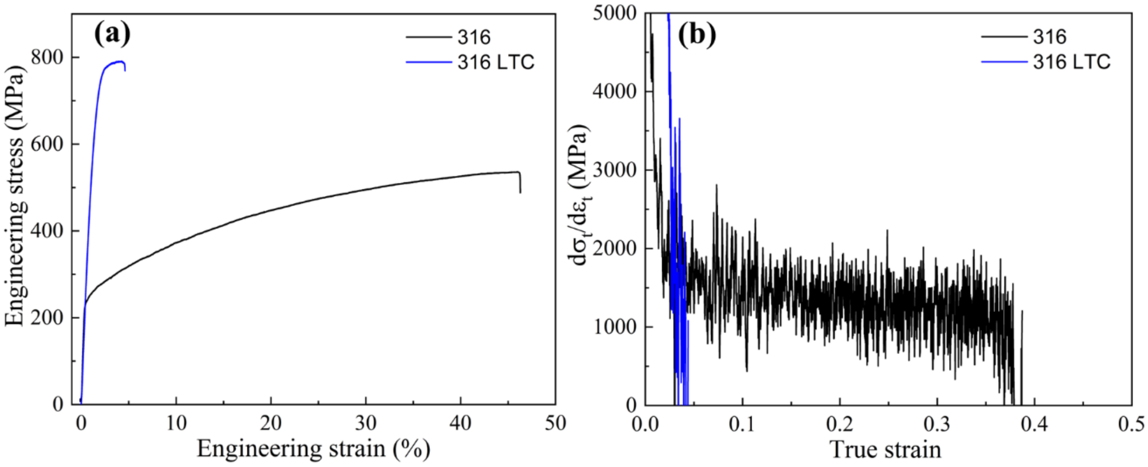

Figure 5.17 (a) Engineering stress-strain curve and (b) work-hardening response of thin 316 and 316 LTC.

5.4 Comparative influence of hydrogen and carbon, and their combined effects on mechanical properties and deformation behavior

For components used in industrial applications, the different processing conditions (cold working and solution annealing), wall thickness, and microstructure homogeneity may affect their mechanical properties and deformation behavior. Low-temperature carburizing and cathodic hydrogen charging can also influence their mechanical properties and deformation behavior. In this section, firstly, the mechanical properties and deformation behavior of cold-worked 304 stainless steel thick tensile bars with low-temperature carburizing and cathodic hydrogen charging were investigated. Secondly, the mechanical properties and deformation behavior of solution-treated 316 thin tensile specimens with low-temperature carburizing and cathodic hydrogen charging were checked. Finally, considering that low-temperature carburizing and cathodic hydrogen charging would introduce a steep interstitial concentration gradient and change the surface stress state, a 3015 alloy with a homogeneous C concentration (~ 0.2 wt%) was used for long-term hydrogen charging to reduce the gradient effect. In-situ EBSD-SEM was used to track the influence of carbon and hydrogen on deformation behavior and microstructure evolution in real time during the deformation process.

5.4.1 Cold worked 304 bulk tensile bars

The effects of LTC and cathodic hydrogen charging on the mechanical properties and deformation behavior of cold-worked 304 bulk tensile bar were evaluated. As shown in Figure 5.18a, both LTC and hydrogen charging increase flow stress while reducing elongation. Analysis of the strain-hardening response in (Figure 5.18b) revealed that the behavior of 304 LTC-H was similar to that of 304 LTC before the true strain level of ~ 12%, indicating that the microstructural stability provided by LTC was largely preserved prior to localized deformation, even in the presence of hydrogen. In contrast, 304-H exhibited a reduced strain-hardening rate, reflecting hydrogen-induced degradation of work-hardening capability. These results demonstrated that LTC treatment effectively stabilized the microstructure, mitigated hydrogen-induced loss of strain hardening, and substantially reduced susceptibility to HE in cold-worked 304 stainless steel.

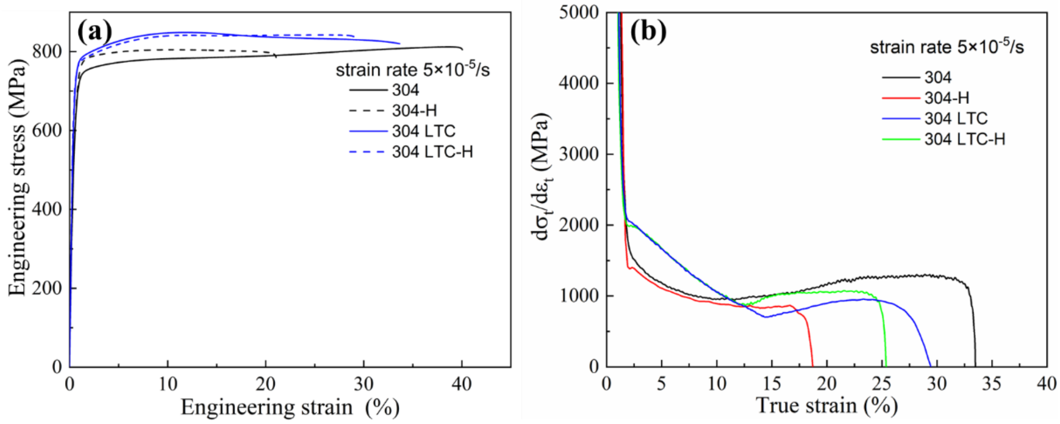

Figure 5.18 (a) Engineering stress-strain and (b) strain-hardening of cold-worked and LTC-treated 304 with and without hydrogen charging.

Microstructure examination of the H-charged samples on the longitudinal section close to the fracture surface after SSRT further elucidates the microstructural origins of embrittlement (Figure 5.19). In 304-H, cracks initiated at the surface and propagated nearly perpendicular to the tensile axis, with additional subsurface microcracks arising from hydrogen-assisted micropore nucleation, growth, and coalescence. Severe plastic deformation near the fracture surface led to fragmented grains, and phase analysis showed a microstructure dominated by α′ martensite. Crack initiation and propagation preferentially occur within α′ grains or along α′/α′ and α′/γ grain boundaries, highlighting the high susceptibility of strain-induced martensite to hydrogen-assisted cracking. By contrast, 304 LTC-H exhibited substantially lower crack density. Austenite stabilization by supersaturated carbon limited α′ martensite formation, resulting in a significantly lower martensite volume fraction compared with 304-H. This suppression of strain-induced martensitic transformation provides a mechanistic explanation for the enhanced resistance to HE conferred by LTC treatment.

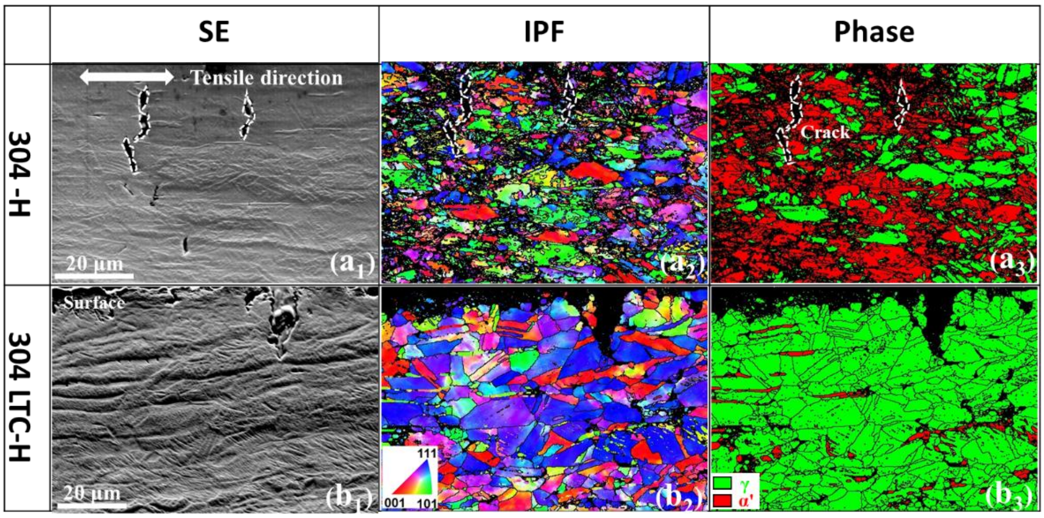

Figure 5.19 Microstructures of the H-charged 304 and 304 LTC on the longitudinal section close to the fracture surface.

Fracture surface analyses reveal the effects of hydrogen uptake and LTC on embrittlement in cold-worked 304 (Figure 5.20). Both cold-worked 304 and 304 LTC exhibited fully ductile fracture, characterized by pronounced necking, equiaxed fine dimples in the central region, and shear lips with elongated dimples at the edges, consistent with microvoid coalescence (MVC) as the dominant fracture mechanism. H-charged specimens, in contrast, displayed flat fracture surfaces with distinct brittle features. A quasi-cleavage morphology emerged along the near-surface region, while the interior exhibited shallow dimples, reflecting a transition from ductile to brittle fracture. High hydrogen fugacity from electrochemical charging generated a hydrogen-supersaturated solid solution in the near-surface region, which promotes localized decohesion and cleavage under stress. Quantitatively, the brittle surface layer was thicker in 304-H (~ 175 μm) than in 304 LTC-H (~ 137 μm), indicating that LTC reduced the depth of hydrogen-affected damage and enhanced embrittlement resistance.

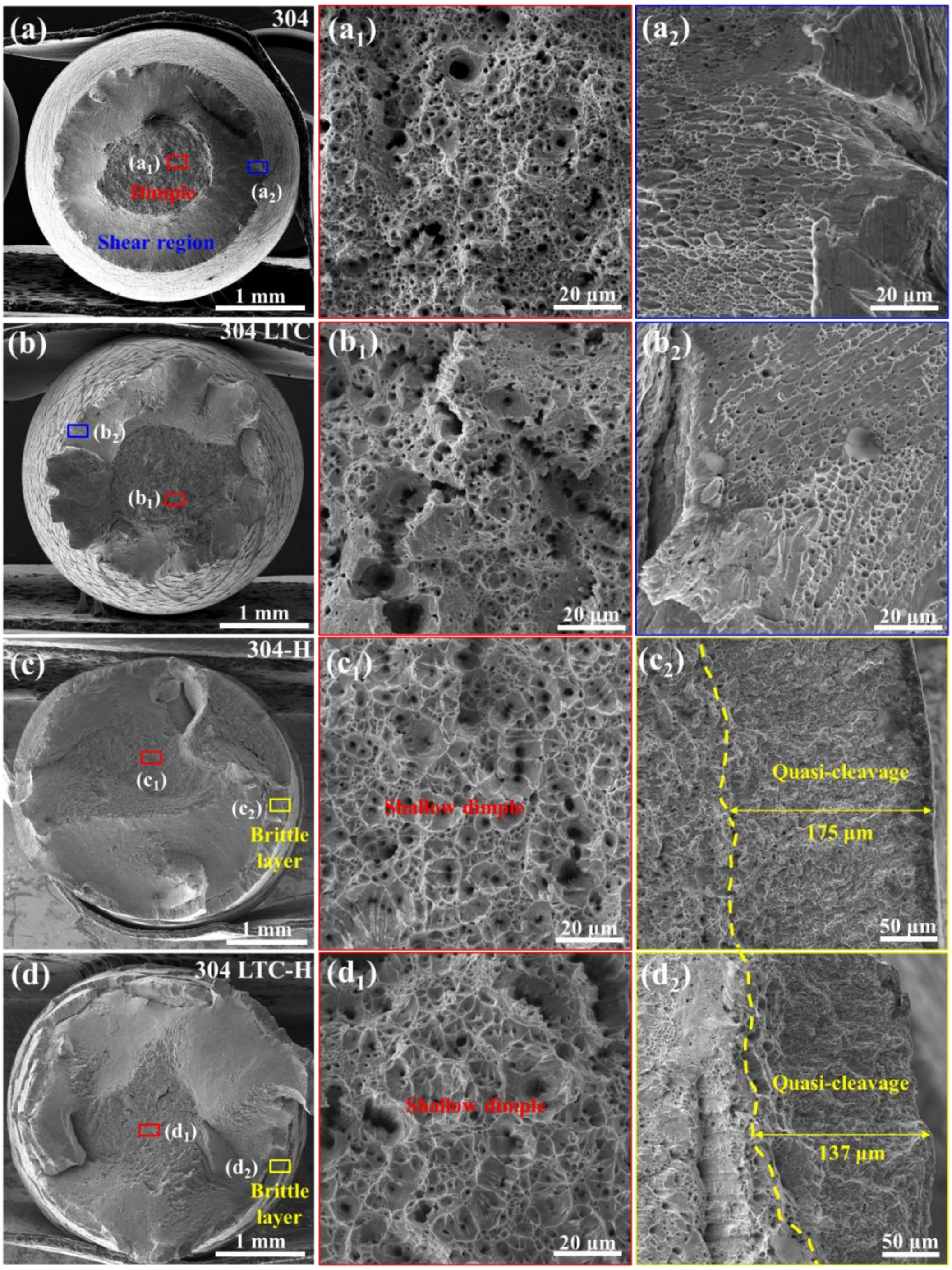

Figure 5.20 Fractography of samples in different conditions (a) 304, (b) 304 LTC, (c) 304-H and (d) 304 LTC-H. The middle column (a$_1$-d$_1$) is from the middle of the sample while the right column (a$_2$-d$_2$) is from the edge of the sample.

5.4.2 Solution annealed 316 thin tensile specimens

Figure 5.21a and Table 5.3 compare the mechanical properties of solution-annealed and LTC-treated 316 thin-film specimens with and without cathodic hydrogen charging. Both carbon and hydrogen increased yield strength and flow stress, consistent with solid-solution strengthening effects relative to reference 316. However, 316 LTC H-3d exhibited lower yield and flow stress than 316 LTC or 316 H-3d, indicating that hydrogen partially offset the strengthening effect of LTC. Analysis of strain-hardening behavior (Figure 5.21b) showed that LTC enhanced strain-hardening rate due to carbon supersaturation. In contrast, hydrogen charging shifted the work-hardening curve of LTC-treated specimens slightly toward lower strains, indicating reduced strain-hardening capacity. These observations suggest that, while carbon promotes deformation stability and strain hardening, hydrogen uptake tends to form precipitates (see Fig. 5.23), thereby lowering solid solution strengthening and weakening the strain-hardening response of 316 LTC.

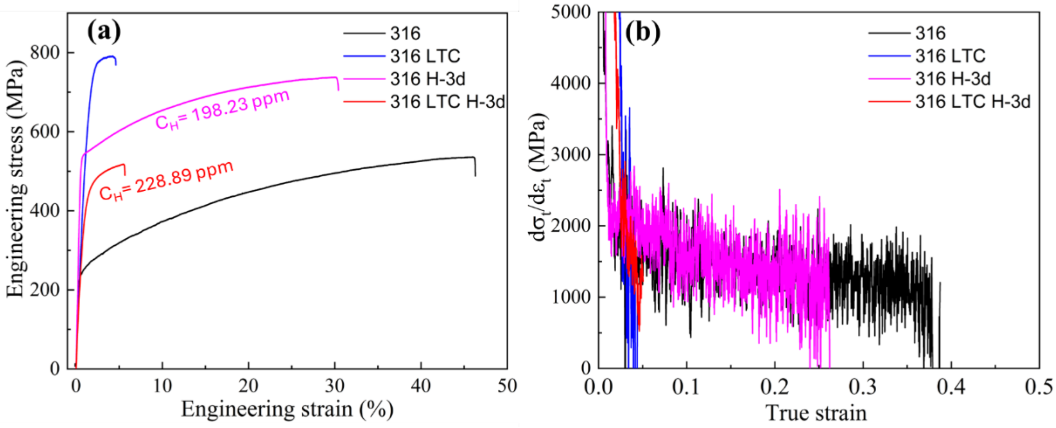

Figure 5.21 (a) Engineering stress-strain and (b) work-hardening responses of thin specimens 316 and 316 LTC with and without hydrogen.

Table 5.3 Mechanical properties of thin 316 and 316 LTC with and without hydrogen charging.

Samples	$R_{p0.2}$ (MPa)	R_m (MPa)	δ (%)
316	222	534	46.3
316 H-3d	528	737	30.2
316 LTC	727	789	4.5
316 LTC H-3d	401	517	5.7

Figure 5.22 compares the fracture morphologies of thin 316 LTC and 316 LTC H-3d to elucidate the effects of carbon and hydrogen on elongation. The 316 LTC exhibited an overall flat fracture surface with extensive surface cracking (Figure 5.22a). High-magnification observations reveal a small population of dimples in the central region (Figure 5.22a$_1$) and a distinct brittle surface layer along the specimen edges (Figure 5.22a$_2$). A transition zone with tear-ridge features separated the brittle layer from the dimpled core. The brittle layer, approximately 17 μm thick, displayed a cleavage (transgranular) fracture morphology, consistent with the extremely low elongation of 316 LTC. The fracture surface of 316 LTC H-3d resembled that of 316 LTC, indicating that hydrogen uptake did not significantly modify the fracture characteristics of the LTC-treated sample. The fracture center remained weakly dimpled (Figure 5.22b$_1$), while the edge regions were dominated by a brittle layer (Figure 5.22b$_2$), accompanied by a transitional

tear ridge beneath the transgranular fracture zone. Notably, no pronounced interfacial delamination was observed in the fracture surfaces of 316 LTC and 316 LTC H-3d compared to 316 H-1d. This phenomenon indicates that the strong bond between the carbon-expanded austenite and the substrate effectively resists hydrogen-induced delamination.

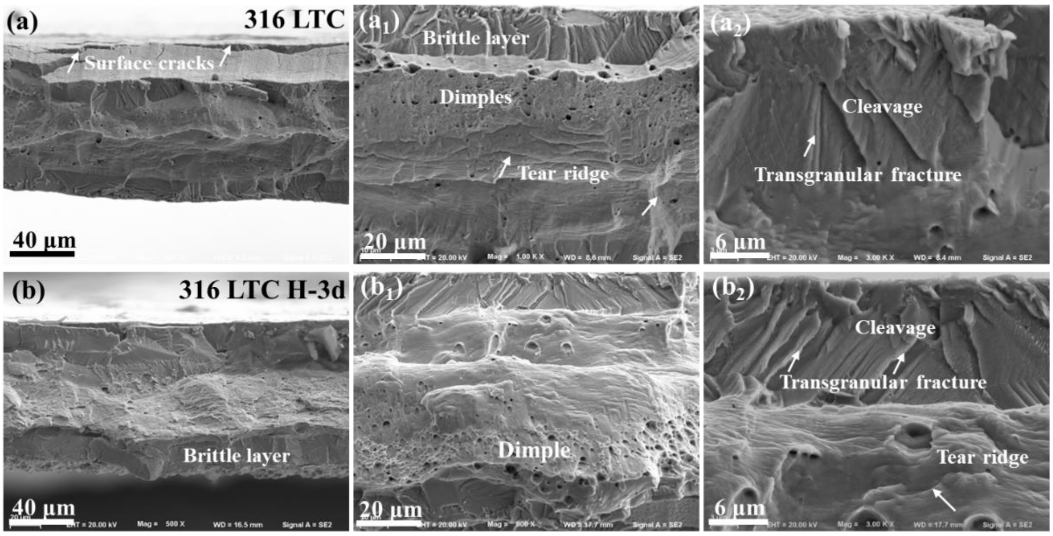

Figure 5.22 Fractography of thin samples in different conditions. (a-a_2) 316 LTC, (b-b_2) 316 LTC H-3d.

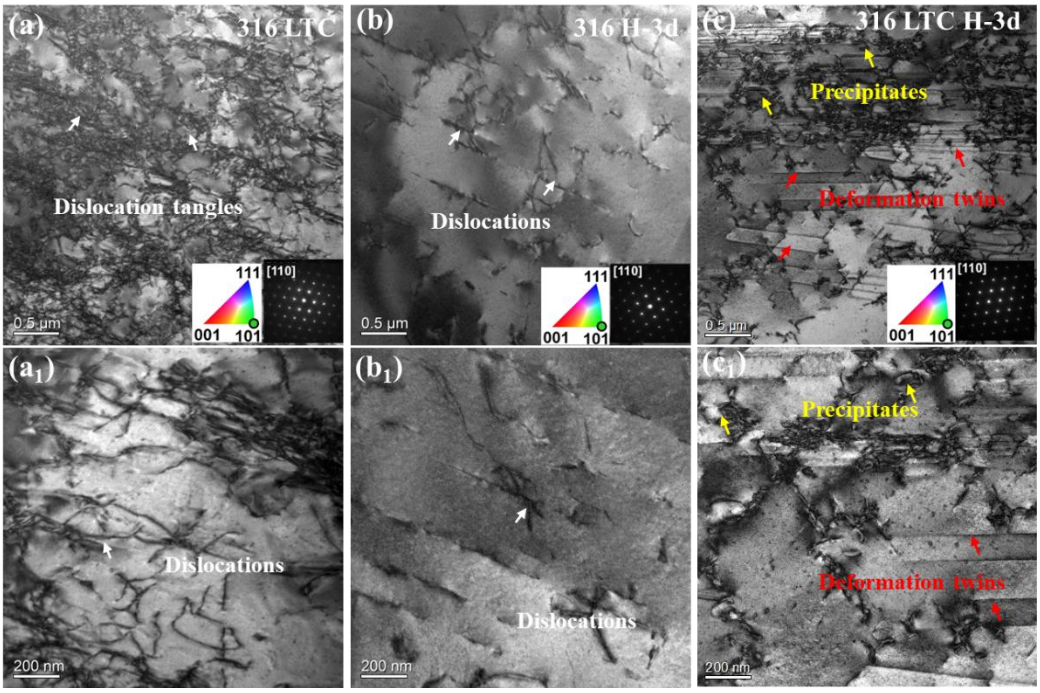

Figure 5.23 Dislocation structures of {110}-oriented grains of thin samples under different conditions after deformed to a strain of 4%. (a-a_1) 316 LTC, (b-b_1) 316 H-3d, (c-c_1) 316 LTC H-3d.

Figure 5.23 compares the dislocation substructures in {110}-oriented grains of 316 LTC, 316 H-3d, and 316 LTC H-3d after 4% prestrain. 316 LTC exhibits a high density of entangled dislocations arranged into well-developed dislocation walls, reflecting strong dislocation interactions and efficient strain accommodation. In contrast, 316 H-3d shows a noticeably lower dislocation density. Strikingly, the 316 LTC H-3d displays a high density of precipitates and deformation twins. This microstructural state is fundamentally different from that of 316 LTC, in which no precipitation is observed. Because low-temperature carburizing produces a supersaturated carbon solid solution without carbide precipitation, the emergence of precipitates in 316 LTC H-3d indicates hydrogen induces precipitation. This effect is likely promoted by the extremely high local stresses and enhanced carbon activity associated with cathodic hydrogen charging, which provide thermodynamic driving force to enhance precipitate formation. Hydrogen-induced precipitation, presumably carbides, has been rarely reported and remains poorly understood. In addition, the abundant deformation twins observed in 316 LTC-H imply a reduction in stacking fault energy, consistent with previous reports that hydrogen decreases the stacking fault energy of austenitic stainless steels [107–109].

5.4.3 3015 alloy bulk tensile bar

Considering the concentration gradient and surface stress caused by LTC treatment, a 3015 super alloy with uniform carbon distribution (~ 0.2 wt%) was selected to reduce carbon-induced stress and microstructure inhomogeneity. To increase the relative hydrogen diffusion depth, tensile bar in a thickness of ~ 0.8 mm was cathodic charging at a current density of 1 mA/cm^2 in 3 wt% NaCl at 80 °C for 168 h, resulting in a bulk hydrogen content of 121.42 ppm. In-situ EBSD–SEM techniques provide direct insight into the effects of hydrogen on deformation behavior, microstructural evolution, and mechanical response in the presence of carbon. As illustrated in Figure 5.24, for the 3015 alloy, hydrogen uptake led to reduced flow stress and elongation, accompanied by a slight decrease in the strain-hardening rate. These changes were indicative of hydrogen-induced softening and increased brittleness. This result is consistent with the softening phenomenon of 316 LTC H-3d thin-film samples caused by hydrogen. Mechanistically, hydrogen uptake results in a reduced lattice parameter and a decrease in solid solution strengthening contribution. Hydrogen-induced localized strain and carbide cracking lead to premature failure.

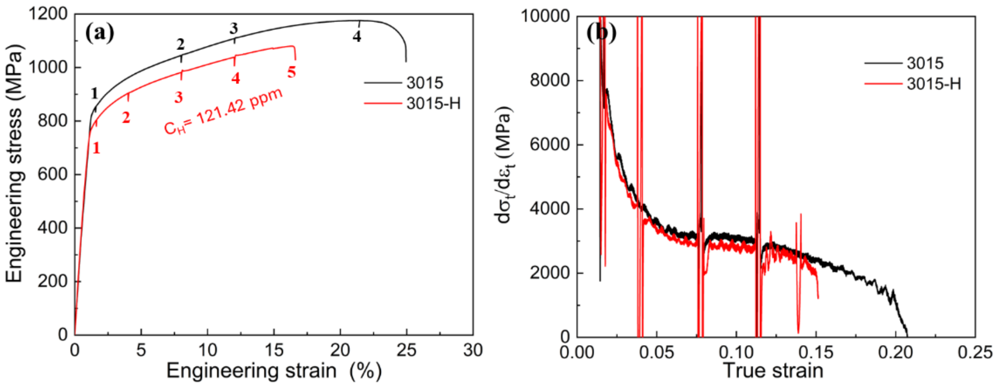

Figure 5.24 (a) Engineering stress–strain curve and (b) strain hardening rate as a function of true strain in 3015 and 3015-H alloy.

Figure 5.25 further illustrates the influence of hydrogen on deformation-induced microstructural evolution in 3015 alloy using inverse pole figure (IPF) and corresponding secondary electron (SE) images at representative strain levels. To account for the strong orientation dependence of plastic deformation, four grains with distinct crystallographic orientations were selected: {111} (G1), {112} (G2), {110} (G3), and {100} (G4). With increasing strain, IPF maps revealed progressive orientation changes in most grains, reflecting increasing lattice distortion during plastic deformation, whereas hard carbide particles retain stable orientations. Correspondingly, SE images showed the gradual development of slip bands within grains, followed by grain extension and rotation, ultimately leading to increased surface roughness. The deformation morphology was orientation dependent. G1 exhibited multiple-slip activity, G2 and G3 primarily displayed single-slip behavior, and G4 showed little to no slip activity. Moreover, G3 contained a higher density of slip bands than G2. Hydrogen markedly altered the onset and progression of deformation. At a low engineering strain (~ 1.6%), the 3015 exhibited minimal microstructural change, whereas the 3015-H already displayed pronounced slip band formation, indicating an earlier onset of yielding. At higher strain (~ 8%), cracks were observed both within carbide particles and the surrounding matrix, demonstrating that hydrogen accelerated localized deformation and promotes deformation-induced failure.

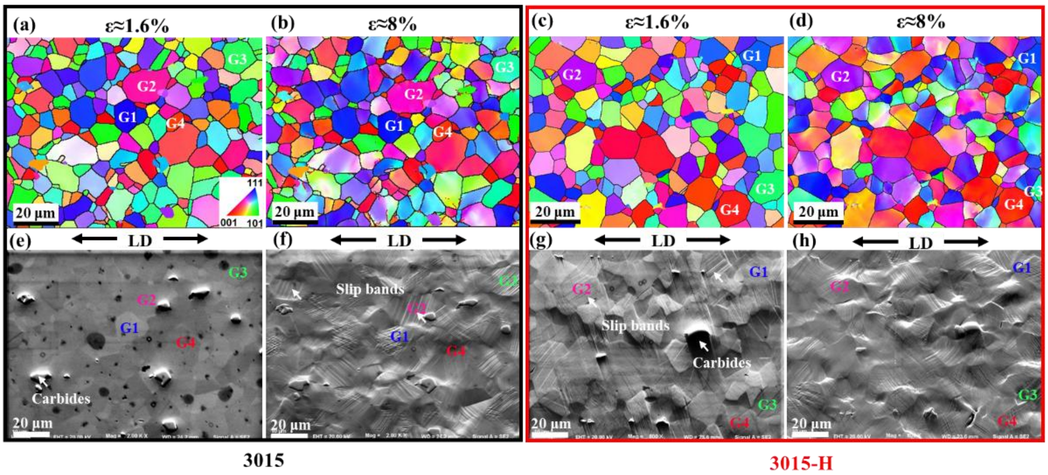

Figure 5.25 (a-d) IPF maps and (e-f) SE images at engineering strain of 1.6% and 8% during tensile load 3015 and 3015-H. G1, G2, G3, and G4 are marked.

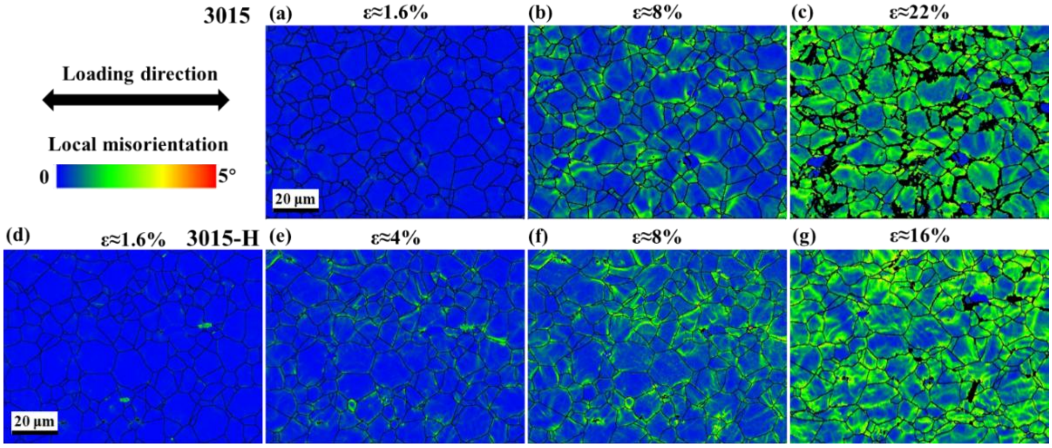

Figure 5.26 Evolution of kernel average misorientation (KAM) of 3015 (a-c) and 3015-H (d-g) at different tensile strain stages.

KAM analysis provided insight into intragranular strain evolution during deformation. As shown in Figure 5.26, KAM values for both 3015 and 3015-H generally increased with increasing strain, reflecting progressive strain accumulation. At low strain (~ 1.6%), the KAM distributions of 3015 and 3015-H were nearly identical. The KAM value at 16% strain for 3015-H is comparable to that at 22% strain for 3015, indicating more strain accumulation with hydrogen uptake.

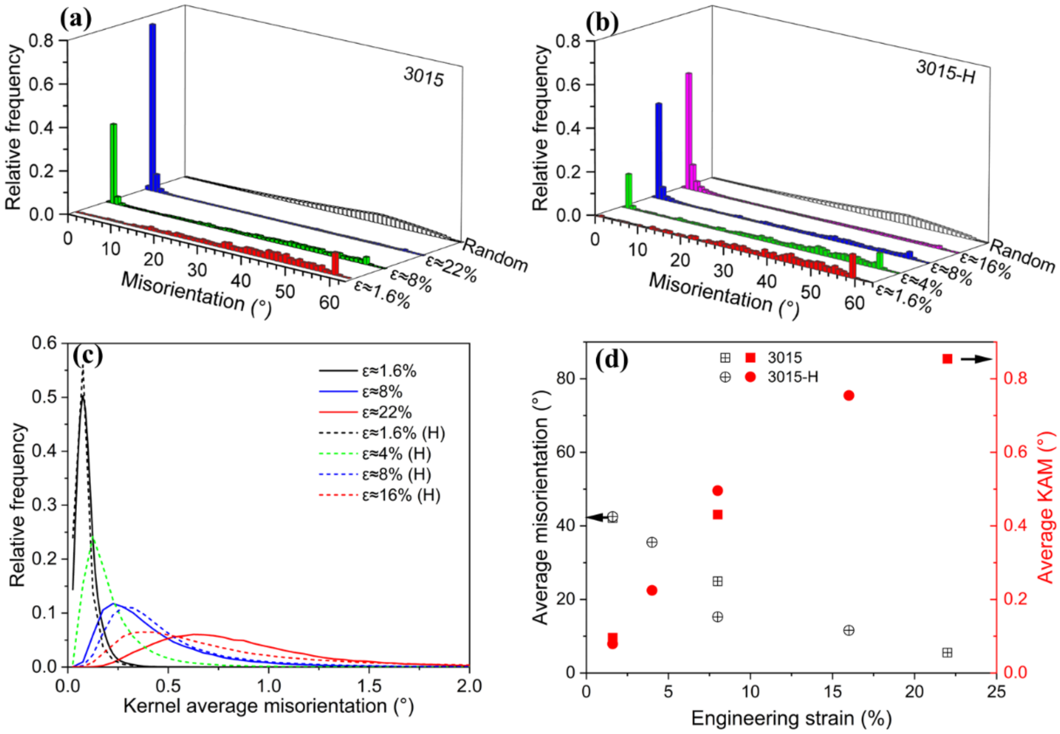

Figure 5.27 (a) (b) Distribution of misorientaion and (c) KAM at different engineering strains and (d) Average KAM and misorientaion as a function of engineering strain.

Figure 5.27 shows a quantitative comparison of the misorientation and KAM distribution of 3015 and 3015-H. With increasing strain, the fraction of low-angle misorientations (< 15°) increased markedly, while high-angle misorientations (≥ 15°) decreased (Figure 5.27a & b), indicating a progressive dominance of dislocation-based deformation. At an engineering strain of 8%, the 3015-H exhibited a substantially higher fraction of low-angle misorientations than the 3015, consistent with accelerated local deformation in the presence of hydrogen. KAM distributions shifted toward higher values with increasing strain, reflecting increased intragranular distortion. Notably, 3015-H exhibited similar KAM values at low strain of 1.6% but higher KAM values at intermediate strain of 8% compared with 3015 (Figure 5.27c), indicating a hydrogen-induced enhancement of strain localization as deformation progresses. Averaged KAM and misorientation values (Figure 5.27d) further confirm that with increasing strain, KAM increases while average misorientation decreases. These results demonstrate that hydrogen promotes localized plastic deformation and enhances strain heterogeneity during tensile loading, consistent with hydrogen-assisted deformation mechanisms.

6 Conclusions

This study focuses on hydrogen embrittlement of austenitic stainless steel, investigating the effects of cathodic hydrogen charging, microstructure and low-temperature carburizing on hydrogen uptake, microstructure evolution, and mechanical properties. The conclusions of this doctoral thesis are based on three research questions (RQs).

RQ1 How does cathodic hydrogen charging affect the microstructure and hydrogen uptake?

Microstructure

- In NaOH electrolyte, hydrogen charging results in a deposition layer enriched in lead on the surface, whereas such effects are negligible in NaCl electrolyte.
- During hydrogen charging in a H_2SO_4 electrolyte, increasing current density and charging time cause a transition in surface damage from slip bands to severe cracking, accompanied by localized strain accumulation and hydrogen-induced martensitic transformation.
- Increased roughness suppresses the initiation of hydrogen-assisted cracking.
- Hydrogen charging reduces the lattice parameters of high-carbon-content samples, while increasing the lattice parameters of low-carbon-content samples.

Hydrogen uptake

- Surface roughening enhances hydrogen recombination on the surface, thereby suppressing hydrogen absorption.
- For polished samples under identical hydrogen charging conditions, hydrogen uptake is lowest in NaCl, intermediate in NaOH, and highest in H_2SO_4 electrolyte.
- Hydrogen content increases markedly with increasing current density and decreasing pH, consistent with high hydrogen fugacity.

RQ2 How does hydrogen uptake affect mechanical properties and deformation behavior?

Hydrogen diffusion depth and nominal hydrogen content have a significant impact on mechanical properties and deformation behavior, which can be achieved by controlling the sample thickness.

Bulk tensile bars-low nominal hydrogen content

- For thick, bulk tensile bars, the reduced elongation and strain hardening rate caused by hydrogen are related to stress cracking induced by high surface hydrogen concentration.
- Hydrogen causes different mechanical properties and deformation behaviors in solution-annealed 304 and 316. The former mainly exhibits reduced flow stress and work hardening rate, while the latter mainly exhibits reduced elongation.
- Microstructure affects hydrogen uptake and hydrogen embrittlement. The finer grains of 316L result in higher hydrogen content and hydrogen embrittlement susceptibility compared to 304.

Thin-film tensile specimens-high nominal hydrogen content

- In solution-annealed 316 thin-film, the flow stress is increased due to hydrogen solid-solution strengthening, and this strengthening effect intensifies with increasing hydrogen content.
- Hydrogen embrittlement susceptibility decreases with increasing hydrogen content because prolonged hydrogen charging reduces the hydrogen concentration gradient.

RQ3 How does carbon affect mechanical properties and deformation behavior?

- Carbon, as an austenite stabilizer and alloying element, can improve the stability of austenite and provide solid solution strengthening, but it will reduce elongation, the extent of which depends on the thickness of C enriched region relative to the steel thickness.
- Carbon increases the work hardening rate through solid solution strengthening. It also increases stacking fault energy, inhibits martensitic phase transformation and deformation twinning, thereby altering work hardening behavior.

RQ4 What are the combined effects of carbon and hydrogen on mechanical properties and deformation behavior?

- Hydrogen or carbon provides solid solution strengthening in 316 thin film, significantly improving yield strength and flow stress, but reducing elongation.
- Carbon can stabilize austenite and suppress hydrogen-induced martensitic transformation. However, austenite containing high carbon faces challenges such as hydrogen-induced carbon desolvation, increased hydrogen uptake, and brittleness.
- Hydrogen induces softening in 316 LTC films and 3015 alloys possibly due to hydrogen-induced precipitation and reduced lattice parameters of austenite.

7 Future work

Hydrogen embrittlement has been a major challenge restricting the widespread application of hydrogen energy, and its importance will become more prominent as society moves towards a low-carbon and sustainable future. Based on the findings of this thesis, several promising research directions can be explored in the future.

1. **Role of surface roughness and residual stress in hydrogen-induced cracking**

Surface roughness plays a critical role in hydrogen absorption and hydrogen-induced cracking, particularly under cathodic hydrogen charging in H_2SO_4 solution. In addition, residual stress is expected to contribute to crack initiation and propagation. Therefore, characterizing the distribution of residual stress on the surface before and after hydrogen charging would provide valuable insight into the mechanisms governing crack nucleation and growth. Such analysis would help clarify the coupled effects of surface morphology, stress state, and hydrogen uptake on hydrogen-assisted cracking behavior.

2. **Hydrogen-induced hardening versus softening and the role of carbide precipitation**

The engineering stress–strain curves reveal hydrogen-induced hardening in 316-H, whereas hydrogen-induced softening is observed in 316 LTC-H and 3015-H. The hardening behavior is attributed to hydrogen-induced solid-solution strengthening. In contrast, the softening behavior is associated with hydrogen-induced surface cracking and possible carbide precipitation, as supported by the presence of surface cracks on tensile specimens, TEM and SEM observations of precipitates, and XRD results showing a reduction in lattice parameters.

Notably, hydrogen-induced carbon desolvation leading to carbide precipitation has rarely been reported in the literature. To further elucidate this mechanism, advanced characterization techniques such as FIB, TEM, and atom probe tomography (APT) are required to investigate hydrogen-induced precipitation at the atomic scale. Such studies may reveal a previously unrecognized mechanism contributing to hydrogen embrittlement in austenitic stainless steels.

3. **Hydrogen concentration gradient and embrittlement behavior**

In the LTC sample, expanded austenite exhibits a pronounced carbon concentration gradient. The surface expanded austenite, constrained by the substrate, exhibits compressive residual stress, while the substrate is subjected to tensile residual stress. Stress-induced surface cracking leads to a significant reduction in elongation an effect often referred to as carbon embrittlement. The substantial loss of elongation observed in the cathodically hydrogen-charged sample is similar to that of the LTC sample, suggesting the presence of a hydrogen concentration gradient. However, with increasing hydrogen charging time, both hydrogen diffusion depth and hydrogen content increase, leading to simultaneous improvements in elongation and strength. This phenomenon is attributed to a decrease in the hydrogen concentration gradient.

To verify this hypothesis, heavy water (D_2O) shall be used as the hydrogen source during cathodic charging, and the deuterium (D) distribution can be characterized using Time-of-Flight

Secondary Ion Mass Spectrometry (TOF-SIMS). Simultaneously, residual stress measurements will be performed at different deuterium concentration locations. These analyses are expected to confirm whether H (D) gradients induced stress cracking is responsible for the observed embrittlement behavior.

4. **Effect of electrolyte chemistry on hydrogen uptake**

An interesting phenomenon was observed during cathodic hydrogen charging in H_2SO_4, NaCl, and NaOH solutions under identical conditions. It was found that the hydrogen content was the highest in the samples charged in H_2SO_4. This behavior can be attributed to two factors: (i) surface cracking, which enhances hydrogen absorption and diffusion, (ii) the abundant hydrogen source provided by H_2SO_4, and (iii) the high hydrogen fugacity by low pH and high overpotential.

In contrast, no surface cracking was observed in samples charged in NaCl or NaOH solutions. Nevertheless, the hydrogen content in NaOH-charged samples was higher than that in NaCl-charged samples. This suggests that OH^- species in NaOH may also contribute to hydrogen uptake. To validate this hypothesis, cathodic charging experiments using H_2O/NaOD or D_2O/NaOH could be performed, followed by quantitative characterization of hydrogen or deuterium content. Such experiments would help determine whether OH^- (or OD^-) ions indeed act as an additional hydrogen source during cathodic charging.

Acknowledgements

First, I would like to thank my supervisor Prof. Emmy Yu Cao for giving me the opportunity to complete my doctoral studies. Your guidance and insights have been invaluable whenever I encountered problems and difficulties. I am also impressed by your rigorous research attitude. You are not only my supervisor but also my friend. At the same time, I am grateful to my examiner Prof. Lars Nyborg and co-supervisor Prof. Huiqun Liu, who gave me timely help when I turned to them.

Here, I would like to especially thank Bodycote GmbH for providing samples and low-temperature carburizing for this study. I also thank SCANIA AB for providing samples and project support. Special thanks to Alexandra Bauer, Rachel Pettersson, Peter Skoglund, Åsa Gustafsson, and Peter Skoglund for their helpful discussions.

I would like to thank Eric Tam and Yiming Yao for their support and help in experiments and equipment training. Eric Tam gave me instructions on electrochemical measurements and experiments. Yiming Yao helped me with metallographic sample preparation and electron microscopy. I would like to thank Bala Malladi for his assistance with the hydrogen content measurement, in-situ tensile test and EBSD analysis. I would like to thank Antonio Mulone for his training on SEM, in-situ EBSD-SEM, and tensile testing. Thanks to Roger Sagdahl for helping me assemble and repair the experimental setup for hydrogen charging.

I would like to express my sincere gratitude to Shi Yao and Vishnu Anilkumar for their academic discussions. I am grateful to Professor Gaoyong Lin for his help in my life and studies. I am also grateful to my office mate, James Randall, Mukesh Murali for their help in my life and study. Thanks to all colleagues at the Department of Industrial and Material Science (IMS), I would like to thank you for creating an enjoyable work environment.

Last but most importantly, I would like to express my deepest gratitude and love to my wife and family for their unselfish support and help.

Xiao Qin

Göteborg, January 2026

Bibliography

[1] A. Mehtab, S.A. Ali, I. Sadiq, S. Shaheen, H. Khan, M. Fazil, N.A. Pandit, F. Naaz, T. Ahmad, Hydrogen energy as sustainable energy resource for carbon-neutrality realization, ACS Sustainable Resource Management, 1 (2024) 604-620.

[2] S.K. Dwivedi, M. Vishwakarma, Hydrogen embrittlement in different materials: A review, International Journal of Hydrogen Energy, 43 (2018) 21603-21616.

[3] I.M. Robertson, P. Sofronis, A. Nagao, M.L. Martin, S. Wang, D.W. Gross, K.E. Nygren, Hydrogen embrittlement understood, Metallurgical and Materials Transactions A, 46 (2015) 2323-2341.

[4] S. Lynch, Hydrogen embrittlement phenomena and mechanisms, Corrosion Reviews, 30 (2012) 105-123.

[5] J Liu, M Zhao, L Rong, Overview of hydrogen-resistant alloys for high-pressure hydrogen environment: on the hydrogen energy structural materials, Clean Energy, 7 (2023) 99-115.

[6] A. Fukunaga, Hydrogen embrittlement behaviors during SSRT tests in gaseous hydrogen for cold-worked type 316 austenitic stainless steel and iron-based superalloy A286 used in hydrogen refueling station, Engineering Failure Analysis, 160 (2024) 108158.

[7] M. Okayasu, T. Fujiwara, Effects of microstructural characteristics on the hydrogen embrittlement characteristics of austenitic, ferritic, and γ–α duplex stainless steels, Materials Science and Engineering: A, 807 (2021) 140851.

[8] G. Han, J. He, S. Fukuyama, K. Yokogawa, Effect of strain-induced martensite on hydrogen environment embrittlement of sensitized austenitic stainless steels at low temperatures, Acta Materialia, 46 (1998) 4559-4570.

[9] M. Koyama, S. Okazaki, T. Sawaguchi, K. Tsuzaki, Hydrogen embrittlement susceptibility of Fe-Mn binary alloys with high Mn content: effects of stable and metastable ε-martensite, and Mn concentration, Metallurgical and Materials Transactions A, 47 (2016) 2656-2673.

[10] T. Michler, C. San Marchi, J. Naumann, S. Weber, M. Martin, Hydrogen environment embrittlement of stable austenitic steels. International Journal of Hydrogen Energy, 37 (2012) 16231-16246.

[11] B.K. Hwang, H.T. Kim, S.J. Cha, G.S. Park, J.T. Yoon, J.H. Kim, J.M. Lee, Comparative study of hydrogen embrittlement in 310S, 304L, and 316L stainless steels under in situ electrochemical hydrogen charging. Part 1: Experimental study, Engineering Failure Analysis, 176 (2025) 109641.

[12] L. Ceschini, C. Chiavari, E. Lanzoni, C. Martini, Low-temperature carburised AISI 316L austenitic stainless steel: Wear and corrosion behaviour, Materials & Design, 38 (2012) 154-160.

[13] S.R. Collins, P.C. Williams, S.V. Marx, A. Heuer, F. Ernst, H. Kahn, Low-temperature carburization of austenitic stainless steels, ASM International, 4 (2014) 451-460.

[14] Y. Peng, Z. Liu, C. Chen, J. Gong, M.A.J. Somers, Effect of low-temperature surface hardening by carburization on the fatigue behavior of AISI 316L austenitic stainless steel, Materials Science and Engineering: A, 769 (2020) 138524.

[15] Y. Jiang, Q. Wu, Y. Wang, J. Zhao, J. Gong, Suppression of hydrogen absorption into 304L austenitic stainless steel by surface low temperature gas carburizing treatment, International Journal of Hydrogen Energy, 44 (2019) 24054-24064.

[16] Y. Li, W. Li, X. Zhu, H. Zhou, X. Jin, Mechanism of improved hydrogen embrittlement resistance of low-temperature plasma carburised stainless steel, Surface Engineering, 34 (2018) 189-192.

[17] Y. Jiang, Y. Li, Y. Peng, J. Gong, Mechanical properties and cracking behavior of low-temperature gaseous carburized austenitic stainless steel, Surface and Coatings Technology, 403 (2020) 126343.

[18] M. Koyama, M. Rohwerder, C.C. Tasan, A. Bashir, E. Akiyama, K. Takai, D. Raabe, K. Tsuzaki, Recent progress in microstructural hydrogen mapping in steels: quantification, kinetic analysis, and multi-scale characterisation, Materials Science and Technology, 33 (2017) 1481-1496.

[19] Q. Liu, A.D. Atrens, Z. Shi, K. Verbeken, A. Atrens, Determination of the hydrogen fugacity during electrolytic charging of steel, Corrosion Science, 87 (2014) 239-258.

[20] X. Lu, D. Wang, R. Johnsen, Hydrogen diffusion and trapping in nickel-based alloy 625: An electrochemical permeation study, Electrochimica Acta, 421 (2022) 140477.

[21] P. Zhang, M. Laleh, A.E. Hughes, R.K.W. Marceau, T. Hilditch, M.Y. Tan, A systematic study on the influence of electrochemical charging conditions on the hydrogen embrittlement behaviour of a pipeline steel, International Journal of Hydrogen Energy, 48 (2023) 16501-16516.

[22] X. Lu, D. Wang, D. Wan, Z.B. Zhang, N. Kheradmand, A. Barnoush, Effect of electrochemical charging on the hydrogen embrittlement susceptibility of alloy 718, Acta Materialia, 179 (2019) 36-48.

[23] D.P Escobar, C. Miñambres, L. Duprez, K. Verbeken, M. Verhaege, Internal and surface damage of multiphase steels and pure iron after electrochemical hydrogen charging, Corrosion Science, 53 (2011) 3166-3176.

[24] J.R. Davis, Stainless steels, ASM international, 1994.

[25] S. Sgobba, Vacuum for accelerators: introduction to materials and properties. arXiv: Accelerator Physics, 2020.

[26] Metals Handbook, Metallography, Structures and Phase Diagrams, American Society for Metals, Metals Park, Ohio, 8th edition, (1973) 425.

[27] P.J. Cunat, Alloying elements in stainless steel and other chromium-containing alloys, Euro Inox, (2004) 1-24.

[28] D. Pierce, A. Haynes, J. Hughes, R. Graves, P. Maziasz, G. Muralidharan, A. Shyam, B. Wang, R. England, C. Daniel, High temperature materials for heavy duty diesel engines: Historical and future trends. Progress in Materials Science, 103 (2019) 109-179.

[29] F. Bayata, A.T. Alpas, The high temperature wear mechanisms of iron-nickel steel (NCF 3015) and nickel based superalloy (inconel 751) engine valves, Wear 480 (2021) 203943.

[30] B. Weiss, R. Sticker, Phase instabilities during high temperature exposure of 316 austenitic stainless steel, Metallurgical and Materials Transactions B, 3 (1972) 851-866.

[31] A.W. Bowen, G.M. Leak, Solute diffusion in alpha- and gamma-Iron, Metallurgical and Materials Transactions B, 1(1970) 1695-1700.

[32] C. Wells, R.F. Mehl, Rate of diffusion of carbon in austenite in plain carbon, in nickel and in manganese steels, Transactions of the Metallurgical Society of AIME, 140 (1940) 279-306.

[33] W. Batz, R.F. Mehl, C. Wells, Diffusion coefficient of carbon in austenite, the Journal of the Minerals, Metals & Materials Society, 2 (1950) 553-560.

[34] O. Rey, P. Jacquot, Kolsterising: hardening of austenitic stainless steel, Surface Engineering, 18 (2002), 412-414.

[35] T. L. Christiansen, M. A. J. Somers, Stress and composition of carbon stabilized expanded austenite on stainless steel, Metallurgical and Materials Transactions A, 4 (2009) 1791-1798.

[36] Y. Jiang, Q. Wu, Y. Li, Y. Peng, J. Gong, Mechanical properties of low-temperature gaseous carburizated layer in 316L stainless steel based on nano-indentation and four-point bending tests. Surface and Coatings Technology, 387 (2020) 125501.

[37] F. Borgioli, From austenitic stainless steel to expanded austenite-S phase: formation, characteristics and properties of an elusive metastable phase, Metals, 10 (2020) 187.

[38] N. Agarwal, Improvement of fatigue properties of stainless steel by low temperature carburization, M.S. thesis, Case Western Reserve University, 2002.

[39] J.P. Hsu, Influence of low-temperature carburization on fatigue crack growth of austenitic stainless steel 316L, M.S. thesis, Case Western Reserve University, 2008.

[40] Z. Liu, S. Wang, Y. Feng, X. Wang, Y. Peng, J. Gong, Exploration on the fatigue behavior of low-temperature carburized 316L austenitic stainless steel at elevated temperature, Materials Science and Engineering: A, 850 (2022) 143562.

[41] J. Qu, P.J. Blau, B.C. Jolly, Tribological properties of stainless steels treated by colossal carbon supersaturation, Wear, 263 (2007) 719-726.

[42] L.J. O'Donnell, G.M. Michal, F. Ernst, H. Kahn, A.H. Heuer, Wear maps for low temperature carburized 316L austenitic stainless steel sliding against alumina, Surface Engineering, 26 (2010) 284-292.

[43] F.J. Martin, P.M. Natishan, E.J. Lemieux, T.M. Newbauer, R.J. Rayne, R.A. Bayles, H. Kahn, G.M. Michal, F. Ernst, A.H. Heuer, Enhanced corrosion resistance of stainless steel carburized at low temperature, Metallurgical and Materials Transactions A, 40 (2009) 1805-1810.

[44] A.H. Heuer, H. Kahn, F. Ernst, G.M. Michal, D.B. Hovis, R.J. Rayne, F.J. Martin, P.M. Natishan, Enhanced corrosion resistance of interstitially hardened stainless steel: Implications of a critical passive layer thickness for breakdown, Acta Materialia, 60 (2010) 716-725.

[45] T. Li, S.C. Chien, Z. Ren, W. Windl, F. Ernst, G.S. Frankel, Understanding the efficacy of concentrated interstitial carbon in enhancing the pitting corrosion resistance of stainless steel. Acta Materialia, 221 (2021) 117433.

[46] F. Borgioli, E. Galvanetto, T. Bacci, Corrosion behaviour of low temperature nitrided nickel-free, AISI 200 and AISI 300 series austenitic stainless steels in NaCl solution, Corrosion Science, 136 (2018) 352-365.

[47] F. Bao, E. Kemppainen, I. Dorbandt, R. Bors, F. Xi, R. Schlatmann, R. Van de Krol, S. Calnan, Understanding the hydrogen evolution reaction kinetics of electrodeposited nickel-molybdenum in acidic, near-neutral, and alkaline conditions. ChemElectroChem, 8 (2021) 195-208.

[48] J.O'M Bokris, P.K. Subramanyan, The equivalent pressure of molecular hydrogen in cavities within metals in terms of the overpotential developed during the evolution of hydrogen, Electrochimica Acta, 16 (1971) 2169-2179.

[49] M. Campo, A. Tanaka, A. Mendes, J.M. Sousa, 3-Characterization of membranes for energy and environmental applications, Advanced membrane science and technology for sustainable energy and environmental applications, Woodhead Publishing, 2011, 56-89.

[50] P. Delahay, M. Pourbaix, P. Van Rysselberghe, Potential-pH diagrams, Journal of Chemical Education, 27 (1950) 683-688.

[51] J.P. Hirth, Effects of hydrogen on the properties of iron and steel, Metallurgical and Materials Transactions A 11 (1980) 861-890.

[52] R.A. Oriani, J.P. Hirth, M. Śmiałowski, Hydrogen degradation of ferrous alloys, Park Ridge, Noyes Publications, 1985.

[53] Y.S. Chen, C. Huang, P.Y. Liu, H.W. Yen, R. Niu, P. Burr, K.L. Moore, E. Martínez-Pañeda, A. Atrens, J.M. Cairney, Hydrogen trapping and embrittlement in metals–a review, International Journal of Hydrogen Energy, 136 (2025) 789-821.

[54] H. Föll, Defects in Crystals, University of Kiel, © Prof. Dr. Helmut Föll. Launch Site, 2019.

[55] A. Turnbull, Hydrogen diffusion and trapping in metals, In Gaseous hydrogen embrittlement of materials in energy technologies, Woodhead Publishing, 2012, 89-128.

[56] W.H. Johnson, II. On some remarkable changes produced in iron and steel by the action of hydrogen and acids, Proceedings of the Royal Society of London, 23 (1875) 168-179.

[57] L.B. Pfeil, The effect of occluded hydrogen on the tensile strength of iron, Proceedings of the Royal Society of London. Series A, Containing Papers of a Mathematical and Physical Character, 112 (1926) 182-195.

[58] A.R. Troiano, The role of hydrogen and other interstitials in the mechanical behavior of metals, Transactions of the ASM, 52 (1960) 54-81.

[59] R.A. Oriani, A mechanistic theory of hydrogen embrittlement of steels, Berichte der Bunsengesellschaft für physikalische Chemie, 76 (1972) 848-857.

[60] C.J. McMahon Jr, Hydrogen-induced intergranular fracture of steels, Engineering Fracture Mechanics, 68 (2001) 773-788.

[61] W.W. Gerberich, R.A. Oriani, M.J. Lji, X. Chen, T. Foecke, The necessity of both plasticity and brittleness in the fracture thresholds of iron, Philosophical Magazine A, 63 (1991) 363-376.

[62] C.D. Beachem, A new model for hydrogen-assisted cracking (hydrogen “embrittlement”)", Metallurgical and Materials Transactions B, 3 (1972) 441-455.

[63] H.K. Birnbaum, P. Sofronis, Hydrogen-enhanced localized plasticity—a mechanism for hydrogen-related fracture, Materials Science and Engineering: A, 176 (1994) 191-202.

[64] P.J. Ferreira, I.M. Robertson, H. K. Birnbaum, Hydrogen effects on the interaction between dislocations, Acta Materialia, 46 (1998) 1749-1757.

[65] T. Matsumoto, J. Eastman, H.K. Birnbaum, Direct observations of enhanced dislocation mobility due to hydrogen, Scripta Metallurgica, 15 (1981) 1033-1037.

[66] T. Tabata, H.K. Birnbaum, Direct observations of hydrogen enhanced crack propagation in iron, Scripta Metallurgica, 18 (1984) 231-236.

[67] H.E. Hänninen, T.C. Lee, I.M. Robertson, H.K. Birnbaum, In situ observations on effects of hydrogen on deformation and fracture of A533B pressure vessel steel, Journal of Materials Engineering and Performance, 2 (1993) 807-817.

[68] S.P. Lynch, Environmentally assisted cracking: Overview of evidence for an adsorption-induced localised-slip process, Acta Metallurgica, 36 (1988) 2639-2661.

[69] S.P. Lynch, Metallographic contributions to understanding mechanisms of environmentally assisted cracking, Metallography, 23 (1989) 147-171.

[70] S.P. Lynch, Mechanisms of hydrogen assisted cracking–a review, Hydrogen effects on material behaviour and corrosion deformation interactions, the Minerals. Metals & Materials Society, Warrendale, 2003, 449-466.

[71] S.P. Lynch, Mechanisms and kinetics of environmentally assisted cracking: current status, issues, and suggestions for further work, Metallurgical and Materials Transactions A, 44 (2013) 1209-1229.

[72] M. Nagumo, Hydrogen related failure of steels–a new aspect, Materials Science and Technology, 20 (2004) 940-950.

[73] M. Nagumo, T. Kenichi, The predominant role of strain-induced vacancies in hydrogen embrittlement of steels: Overview, Acta Materialia, 165 (2019) 722-733.

[74] X.C. Ren, Q.J. Zhou, G.B. Shan, W.Y. Chu, J.X. Li, Y.J. Su, L.J. Qiao, A nucleation mechanism of hydrogen blister in metals and alloys, Metallurgical and materials transactions A, 39 (2008) 87-97.

[75] M.C. Tiegel, M.L. Martin, A.K. Lehmberg, M. Deutges, C. Borchers, R. Kirchheim, Crack and blister initiation and growth in purified iron due to hydrogen loading, Acta Materialia, 115 (2016) 24-34.

[76] R. Kirchheim. Reducing grain boundary, dislocation line and vacancy formation energies by solute segregation. I. Theoretical background, Acta Materialia, 55 (2007) 5129-5138.

[77] R. Kirchheim, On the solute-defect interaction in the framework of a defactant concept. International Journal of Materials Research, 100 (2009) 483-487.

[78] R. Kirchheim, Revisiting hydrogen embrittlement models and hydrogen-induced homogeneous nucleation of dislocations, Scripta Materialia, 62 (2010) 67-70.

[79] R. Kirchheim, S. Bria, S. Petros, Chemomechanical effects on the separation of interfaces occurring during fracture with emphasis on the hydrogen-iron and hydrogen-nickel system, Acta Materialia, 99 (2015) 87-98.

[80] A. Barnoush, V. Horst, In situ electrochemical nanoindentation: A technique for local examination of hydrogen embrittlement, Corrosion Science, 50 (2008) 259-267.

[81] M. Deutges, I. Knorr, C. Borchers, C.A. Volkert, R. Kirchheim, Influence of hydrogen on the deformation morphology of vanadium (100) micropillars in the α-phase of the vanadium–hydrogen system, Scripta Materialia, 68 (2013) 71-74.

[82] J. Čížek, O. Melikhova, I. Procházka, Hydrogen-induced defects and multiplication of dislocations in Palladium, Journal of Alloys and Compounds, 645 (2015) S312-S315.

[83] H. Yu, A. Díaz, X. Lu, B. Sun, Y. Ding, M. Koyama, J. He, X. Zhou, A. Oudriss, X. Feaugas, Z. Zhang, Hydrogen embrittlement as a conspicuous material challenge—comprehensive review and future directions, Chemical Reviews, 124 (2024) 6271-6392.

[84] S. Rahimi, K. Verbeken, T. Depover, E. Proverbio, Hydrogen embrittlement of pipeline steels under gaseous and electrochemical charging: A comparative review on tensile properties, Engineering Failure Analysis, 167 (2025) 108956.

[85] Y. Momotani, A. Shibata, D. Terada, N. Tsuji, Effect of strain rate on hydrogen embrittlement in low-carbon martensitic steel, International Journal of Hydrogen Energy, 42 (2017) 3371-3379.

[86] M. Kawamori, K. Shibata, R. Yoda, S. Morita, Y. Fujita, S. Kuroda, B. Sesen, M. Rohwerder, Dual effects of deformation on hydrogen embrittlement of austenitic stainless steels revealed by hydrogen visualization combined with microstructural analysis, International Journal of Hydrogen Energy, 145 (2025) 559-577.

[87] G. Álvarez, A. Zafra, F.J. Belzunce, C. Rodríguez, Hydrogen embrittlement testing procedure for the analysis of structural steels with Small Punch Tests using notched specimens, Engineering Fracture Mechanics, 253 (2021) 107906.

[88] A. Zafra, G. Álvarez, G. Benoit, G. Hénaff, E. Martínez-Paneda, C. Rodríguez, J. Belzunce, Hydrogen-assisted fatigue crack growth: Pre-charging vs in-situ testing in gaseous environments, Materials Science and Engineering: A, 871 (2023) 144885.

[89] A. Houben, J. Engels, M. Rasiński, C. Linsmeier, Comparison of the hydrogen permeation through fusion relevant steels and the influence of oxidized and rough surfaces. Nuclear Materials and Energy, 19 (2019) 55-58.

[90] Y. Mine, K. Tachibana, Z. Horita, Grain-boundary diffusion and precipitate trapping of hydrogen in ultrafine-grained austenitic stainless steels processed by high-pressure torsion. Materials Science and Engineering: A, 528 (2011) 8100-8105.

[91] M. Moallemi, H.J. Cho, S.J. Kim, The adverse effect of grain refinement on hydrogen embrittlement in a high Mn austenitic steel, Materials Science and Engineering: A, 916 (2024) 147367.

[92] P. Cavaliere, Hydrogen Embrittlement: Fundamentals. In: Hydrogen Embrittlement in Metals and Alloys. Springer, Cham. Springer Nature Switzerland, 2025.

[93] B. Miller, P. Swartzentruber, Fracture Mechanisms. In Fractography, ASM International, 2024.

[94] X. Qin, Y. Shi, L. Nyborg, H. Liu, Y. Cao, Hydrogen, similar to interstitial carbon, significantly strengthen 316 austenitic stainless steel. In press

[95] J.A. Lee, S. Woods, Hydrogen embrittlement, NASA/TM-2016-218602, 2016.

[96] T. Doshida, K. Takai, Dependence of hydrogen-induced lattice defects and hydrogen embrittlement of cold-drawn pearlitic steels on hydrogen trap state, temperature, strain rate and hydrogen content, Acta Materialia, 79 (2014) 93-107.

[97] J. Venezuela, Q. Liu, M. Zhang, Q. Zhou, A. Atrens, A review of hydrogen embrittlement of martensitic advanced high-strength steels, Corrosion Reviews, 34(2016) 153-186.

[98] P. Gümpel, Surface hardening of stainless steels by Kolsterising. Applied Science and Engineering Progress, 5 (2012) 11-18.

[99] L. Ceschini, M. Carla, Kolsterising®, Encyclopedia of tribology, Springer, 2013.

[100] D. Eaves, G. Williams, H.N. McMurray, Inhibition of self-corrosion in magnesium by poisoning hydrogen recombination on iron impurities, Electrochimica Acta, 79 (2012) 1-7.

[101] S. Ajito, T. Hojo, M. Koyama, E. Akiyama, Effects of ammonium thiocyanate and pH of aqueous solutions on hydrogen absorption into iron under cathodic polarization. ISIJ International, 61 (2021) 1209-1214.

[102] M.A.V. Devanathan, Z. Stachurski, The adsorption and diffusion of electrolytic hydrogen in palladium, Proceedings of the Royal Society of London. Series A. Mathematical and Physical Sciences, 270 (1962) 90-102.

[103] ASTM E384-22, Standard Test Method for Microindentation Hardness of Materials, ASTM international, 2022.

[104] ASTM E8M-22, Standard Test Methods for Tension Testing of Metallic Materials, ASTM international, 2022.

[105] P. Rozenak, A. Loew, Stress distributions due to hydrogen concentrations in electrochemically charged and aged austenitic stainless steel. Corrosion Science, 50 (2008) 3021-3030.

[106] R.F. Chuproski, B.C.E.S. Kurelo, W.R. de Oliveira, G. Ossovisck, F.C. Serbena, G.B. de Souza, In situ structural and mechanical analysis of the hydrogen-expanded austenite, International Journal of Hydrogen Energy, 48 (2023) 8685-8695.

[107] T. Komabayashi, C. McGuire, S. Thompson, G.D. Bromiley, A. Bravenec, A. Pakhomova, High-pressure melting experiments of Fe3C and a thermodynamic model of Fe-C liquids for the Earth's core, Journal of Geophysical Research: Solid Earth, 129 (2024) e2024JB029641.

[108] H. Shi, S. Nandy, H. Cheng, B. Sun, D. Ponge, In-situ investigation of the interaction between hydrogen and stacking faults in a bulk austenitic steel. Acta Materialia, 262 (2024) 119441.

[109] A.E. Pontini, J.D. Hermida, X-ray diffraction measurement of the stacking fault energy reduction induced by hydrogen in an AISI 304 steel, Scripta Materialia, 37 (1997) 1831-1837.

[110] Y. Ogawa, H. Hosoi, K. Tsuzaki, T. Redarce, O. Takakuwa, H. Matsunaga, Hydrogen, as an alloying element, enables a greater strength-ductility balance in an Fe-Cr-Ni-based, stable austenitic stainless steel. Acta Materialia, 199 (2020) 181-192.

[111] T. Ito, Y. Ogawa, W. Gong, W. Mao, T. Kawasaki, K. Okada, A. Shibata, S. Harjo, Role of solute hydrogen on mechanical property enhancement in Fe–24Cr–19Ni austenitic steel: An in situ neutron diffraction study, Acta Materialia, 287 (2025) 120767.